

LEABHARLANN CHOLÁISTE NA TRÍONÓIDE, BAILE ÁTHA CLIATH | TRINITY COLLEGE LIBRARY DUBLIN
Ollscoil Átha Cliath | The University of Dublin

Terms and Conditions of Use of Digitised Theses from Trinity College Library Dublin

Copyright statement

All material supplied by Trinity College Library is protected by copyright (under the Copyright and Related Rights Act, 2000 as amended) and other relevant Intellectual Property Rights. By accessing and using a Digitised Thesis from Trinity College Library you acknowledge that all Intellectual Property Rights in any Works supplied are the sole and exclusive property of the copyright and/or other IPR holder. Specific copyright holders may not be explicitly identified. Use of materials from other sources within a thesis should not be construed as a claim over them.

A non-exclusive, non-transferable licence is hereby granted to those using or reproducing, in whole or in part, the material for valid purposes, providing the copyright owners are acknowledged using the normal conventions. Where specific permission to use material is required, this is identified and such permission must be sought from the copyright holder or agency cited.

Liability statement

By using a Digitised Thesis, I accept that Trinity College Dublin bears no legal responsibility for the accuracy, legality or comprehensiveness of materials contained within the thesis, and that Trinity College Dublin accepts no liability for indirect, consequential, or incidental, damages or losses arising from use of the thesis for whatever reason. Information located in a thesis may be subject to specific use constraints, details of which may not be explicitly described. It is the responsibility of potential and actual users to be aware of such constraints and to abide by them. By making use of material from a digitised thesis, you accept these copyright and disclaimer provisions. Where it is brought to the attention of Trinity College Library that there may be a breach of copyright or other restraint, it is the policy to withdraw or take down access to a thesis while the issue is being resolved.

Access Agreement

By using a Digitised Thesis from Trinity College Library you are bound by the following Terms & Conditions. Please read them carefully.

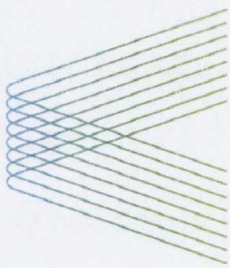
I have read and I understand the following statement: All material supplied via a Digitised Thesis from Trinity College Library is protected by copyright and other intellectual property rights, and duplication or sale of all or part of any of a thesis is not permitted, except that material may be duplicated by you for your research use or for educational purposes in electronic or print form providing the copyright owners are acknowledged using the normal conventions. You must obtain permission for any other use. Electronic or print copies may not be offered, whether for sale or otherwise to anyone. This copy has been supplied on the understanding that it is copyright material and that no quotation from the thesis may be published without proper acknowledgement.



embarkinitiative
Investing in People and Ideas

sfi
science foundation ireland
fondúireacht eolaíochta éireann

Mechanical Properties of One-Dimensional Nano-Systems



PhD Chemistry 2010

Dorothée Almecija (05172373)

Supervisor: Prof. John J. Boland

School of Chemistry & CRANN

Trinity College Dublin

Table of Content

Acknowledgement i

Declaration ii

Permission to Lend and/or Copy iii

Summary iv

Glossary vi

Introduction **1**

1. Methodologies and Techniques 3

1.1. General introduction to mechanical properties 3

1.1.1. Elastic materials 4

1.1.2. Non-linear materials – polymers 6

1.2. Techniques to measure mechanical properties at the nanoscale 7

1.2.1. Two-dimensional systems – thin films 7

1.2.2. Zero-dimensional systems – nanoparticles 10

1.2.3. One-dimensional systems – nanowires 13

Conclusion 27

References 27

2. Equipment **32**

2.1. Atomic Force Microscope (AFM) 32

2.1.1. Working principle 32

2.1.2. Mechanical measurements 35

2.2. Scanning Electron Microscope (SEM) and Focussed Ion Beam (FIB) 42

2.3. Transmission Electron Microscope (TEM) 46

Conclusion 49

References 49

3. Mechanical properties of germanium nanowires with diameter above 40 nm. **51**

3.1. Motivation 51

3.2. Germanium nanowires synthesis and structure 54

3.3. Mechanical measurements – Results 55

Conclusion 59

References 59

TRINITY COLLEGE
2 4 MAR 2011
LIBRARY DUBLIN
THESIS
8923

4. Mechanical properties of germanium nanowires with diameter below 40 nm. 62

4.1. Motivation 62

4.2. Mechanical measurements of small germanium nanowires 66

4.2.1. Nanowires synthesis 66

4.2.2. Standard AFM technique 68

4.2.3. Improved method for mechanical measurements 71

Conclusion 75

References 75

5. Mechanical properties of individual polymer carbon nanotubes composites fibers 77

5.1. Motivation 77

5.2. Experimental procedure 82

5.3. Results and analysis 84

5.3.1. Force-displacement measurements 84

5.3.2. Theoretical considerations 87

5.3.3. Data analysis 89

Conclusion 93

References 93

Conclusion 98

Publications 100

Appendices 101

Appendix A. TEM sample preparation procedure 101

Appendix B. Young's modulus determination from generalised model 104

Appendix C. Ongoing work. Investigation of the electromechanical properties of germanium nanowires 111

Acknowledgement

I would like to thank my supervisor Prof John J. Boland for his help and guidance throughout. A special thanks to Dr Justin D. Holmes, Dr Graham Cross and Dr Vojislav Krstic for insightful discussions. I would also like to thank SFI, CRANN and IRCSET for funding my research.

My deepest thanks to my partner Martin for his support and love; you made these last 4 years the best of my life and I am very much looking forward spending the rest of our lives together. Sincere thanks go to my family especially my brother Eric, his partner Laurence, my mother Marie-Thérèse and my uncle René. I also send a special thanks to my friends for the encouragement and numerous laughs and memories they provided over the years.

I would also like to thank all the members, past and present, of John Boland research group especially Ronan, Niall, Mary, Peter Nirmalraj, Eoin, Lien, Mick, Bin, Tetsuya, John, Peter Gleeson, Soon Jung and Baomei.

.

Declaration

I, the undersigned, declare that this work has not previously been submitted as an exercise for a degree at this, or any other University, and that unless otherwise stated, is my own work.

Permission to Lend and/or Copy

I, the undersigned, that Trinity College Library may lend or copy this dissertation upon request.



Dorothée Almecija

Monday, 07 June 2010

Summary

The measurement of mechanical properties of nano-scale materials is paramount for their safe and efficient incorporation into devices. Techniques to perform these measurements are reviewed here with a particular interest on one-dimensional systems. Following a technique developed in our lab we study the mechanical properties of germanium nanowires and polymer-carbon nanotubes composites. In this technique one-dimensional materials are spanned across a trench and pinned on both sides. Subsequently an AFM tip laterally loads the nanowire while the laser deflection on the photo-detector is closely monitored and recorded. This allows the plotting of force-displacement curves. In the instance of covalently bonded linear materials, such as germanium nanowires, we have developed a generalised model to extract both Young's modulus and ultimate strength of the material from these curves. These were established at 112 GPa and 15 GPa respectively. The latter was the highest strength ever recorded for a semiconductor nanowire. In the case of a polymer composite, poly-vinyl-alcohol and carbon nanotubes, we used a simple elastic model to account for the deformation and established lower bounds for modulus and strength of the fibers in relation with the concentration of carbon nanotubes in the polymer.

This technique was employed to study the mechanical properties of small germanium nanowires, of diameters from 10 to 40 nm. Unfortunately a large scatter in the data was present for the smallest nanowires, preventing us from drawing conclusions about their behaviour. However, it was found that these small nanowires exhibited great resilience as they could be deformed up to 30 times their radius. Subsequent measurements were performed on a TEM grid and the fracture and crystal structure of the nanowire was studied. High resolution TEM revealed that this issue stemmed from a large oxide layer on the nanowires and non-cylindrical nanowires. While it was possible to manipulate the nanowires on the carbon layer of a TEM grid, no quantitative data on the mechanical properties of the nanowires could be extracted due to the compliance of the carbon film. A similar experiment was attempted on Si_3N_4 TEM grids lithographically designed with micro-sized holes and was successful for larger nanowires. Single-crystal nanowires exhibited much higher modulus and strength than nanowires containing stacking faults.

Unfortunately the small germanium nanowires tended to adhere to holes in the substrate rather that lying over holes, thus precluding mechanical measurements. We are still dealing with this issue and are developing an approach using the adhesion of nanowires on the substrate and their resulting curvature as a means to estimate mechanical properties.

Preliminary work was also carried out in the determination of electro-mechanical properties of germanium nanowires. Substrates were fabricated using UV lithography and EBL. These were comprised of 20 interdigitated electrodes separated by 400 nm deep trenches. Nanowires were contacted to the electrodes with electron beam induced deposition of tungsten. A proposal for a nano-pulley electromechanical system is introduced.

Glossary

AFM	Atomic Force Microscope
SEM	Scanning Electron Microscope
FIB	Focussed Ion Beam
TEM	Transmission Electron Microscope
NW	Nanowire
CNT	Carbon nanotube
Ge	Germanium
PVA	Poly-Vinyl-Alcohol
EBL	Electron Beam Lithography

Introduction

Since Richard Feynman's talk at the 1959 meeting of the American Physical Society at Caltech titled 'There's plenty of room at the bottom', nanoscience has been a major topic of research. Silicon technology has played an important role in the miniaturisation of transistors and CMOS have been following Moore's Law with a decrease in feature sizes by a factor of 0.7 every 3 years[1]. The International Technology Roadmap for Semiconductors (ITRS) 2009 report highlights the difficulties of going beyond the 22 nm node[2]. It is expected that the metal oxide semiconductor field effect transistors (MOSFETs) node will be scaled down to 18 nm with a gate length down to 7 nm. Table 1 displays the long term technology requirements for the main transistors parameters[3].

Table 1. *ITRS 2007. Long term technology requirements. Double gate MOSFETs.*

		year						
		2016	2017	2018	2019	2020	2021	2022
node (nm)		22	20	18	16	14	13	11
Lg (nm)	HP	9	8	7	6	5.6	5.0	4.5
	LSTP	14	13	12	11	10	9	8
	LOP	11	10	9	8	7	6.5	6
V_{dd} (V)	HP	0.8	0.7	0.7	0.7	0.65	0.65	0.65
	LSTP	0.8	0.8	0.8	0.75	0.75	0.7	0.7
	LOP	0.6	0.5	0.5	0.5	0.5	0.45	0.45
$V_{t,sat}$ (mV)	HP	110	109	114	119	123	115	118
	LSTP	366	371	365	374	378	369	376
	LOP	202	188	194	190	195	190	201
I_{off} (DG) (μA/μm)	HP	0.44	0.48	0.45	0.47	0.43	0.62	0.60
	LSTP	2.97×10^{-5}	2.55×10^{-5}	3.38×10^{-5}	2.62×10^{-5}	2.39×10^{-5}	3.38×10^{-5}	2.89×10^{-5}
	LOP	1.31×10^{-2}	2.23×10^{-2}	1.94×10^{-2}	2.55×10^{-2}	2.41×10^{-2}	3.26×10^{-2}	2.40×10^{-2}
I_{on} (DG) (μA/μm)	HP	2627	2533	2804	2768	2677	2799	2786
	LSTP	738	839	889	895	935	934	946
	LOP	916	808	850	900	919	874	876
E_{OT} (DG) (Å)	HP	5.5	5.5	5.5	5	5	5	5
	LSTP	11	10	10	9	9	8	8
	LOP	8	7	7	7	7	6	6

[a] HP, high performance; LSTP, low standby power; LOP, low operation power.

However, top-down planar bulk Si MOSFETs are unlikely to meet the ITRS requirements in the long term. Bottom-up techniques seem to be more likely to achieve these goals and semiconductor nanowires (SC NWs) are prime candidates for these building blocks. Due to their high aspect ratio and surface area, SC NWs exhibit interesting electronic properties[4] making them an attractive option for transistors, actuators and nano-electro-mechanical systems. The integration of SC NWs into complex functional architectures is at the centre of many research projects. However it is important to understand the mechanical properties of these nanowires before their implementation

into devices. Deformation mechanisms, strength at fracture and amount of energy that can be stored are but a few critical properties that need to be studied.

In this thesis we focus on the mechanical properties of germanium nanowires that were investigated using a method developed in our lab in 2005[5]. This technique uses an atomic force microscope (AFM) tip to laterally load a suspended nanowire. From the deflection of the signal on the photodiode, force-displacement curves are generated. Since 2005 this method was used to study the properties of Au,[5] Ag[6], Si[7], Ge[8], ZnO[9] and polymer-carbon nanotubes composite fibres[10]. In addition a generalised model was developed to extract Young's modulus and strength from the force-displacement curves. Here we will detail the study of germanium nanowires and polymer fibres. We found this technique to reach its limit for very small nanowires, with diameters smaller than 20 nm due to surface effects and oxide layer. A similar technique involving high resolution transmission electron microscopy (HRTEM) was then developed to account for these effects.

The first two chapters of this thesis review the techniques used to study the mechanical properties of nano-systems and the equipment needed for this investigation. The following two chapters focus on germanium nanowires with Chapter 3 concerning nanowires of diameters above 20 nm and Chapter 4 that of less than 20 nm. The fifth chapter focuses on the mechanical properties of polymer-carbon nanotube composites. The last chapter detail preliminary work carried out on the electro-mechanical properties of germanium nanowires.

1. Methodologies and Techniques

1.1. General introduction to mechanical properties

In material science, mechanical properties play an important role. All engineered materials need to have their mechanical properties characterised before being incorporated into functional devices. Some properties are intrinsic while others depend on how the material is processed and ultimately used. The most common way to test mechanical properties is the tensile test. It provides important insights in both the material's elastic properties and plastic deformation. We will use tensile test concepts to provide an introduction into the main mechanical properties of materials and the terminology used. A review of the main characteristics of elastic materials and their fracture will be presented as well as a brief introduction on plastic deformation. After introducing the mechanical properties of materials in general, we will focus on the techniques used to investigate these properties from the macroscale to the nanoscale.

Materials have mechanical properties, let us define these[11]:

- Stress: ratio of the applied load divided by the initial cross sectional area
- Strain: ratio of change in length over the initial length
- Strength: property that enables a material to resist deformation under load.
    - Yield strength: stress level related to the onset of irreversible plastic deformation
    - Ultimate tensile strength: maximum load divided by initial cross sectional area
    - True fracture strength: load at fracture divided by final actual cross sectional area

Materials can be deformed or fractured in different ways:

- Deformation:
    - Elastic: material recovers its original shape after the load is removed
    - Plastic: permanent deformation of the material without breaking
- Failure:
    - Brittle: material that breaks before it deforms
    - Ductile: ability of the material to become significantly deformed prior to breaking

1.1.1. Elastic materials

When a material shows a complete elastic response to deformation, it follows Hooke's law. The latter predicts a linear relationship between the stress (σ) applied to the material and the strain (ε) undergone by this material, displayed on Equation 1.

$$\sigma = E\varepsilon \qquad \textbf{Equation 1}$$

E is a proportionality constant often referred to as Young's Modulus or the modulus of elasticity. The Young's modulus is a measure of the interatomic forces between adjacent atoms or ions within the material. We consider how the potential energy (*E*) between two adjacent particles changes with their distance of separation *x*, displayed on Figure 1.

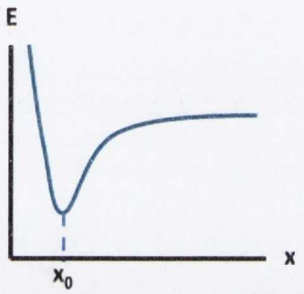


Figure 1. *Potential energy versus inter-atomic spacing*

The equilibrium distance of separation x_0 corresponds to a minimum in potential energy, which is a balance of attractive and repulsive energies between adjacent atoms. At x_0, the force acting on the particles, $F=dE/dx$, is zero. The first derivative of the force with respect to distance of particle separation, dF/dx, i.e. d^2E/dx^2, describes the stiffness or relative resistance to separation of the two particles. This quantity is the atomic level analogue of the Young's modulus described earlier on. As such, the modulus of elasticity is a measure of the bonding force between the atoms in the solid. It varies greatly between solids, ranging from a few MPa for polymers to almost 1 TPa for diamond[12]. This definition of the Young's modulus and Hooke's law is quite simplistic. There is a generalised version of Hooke's law which takes multi-axial loading conditions and material anisotropy into account. Stress in one direction can cause strain in the other two orthogonal directions, introducing *G* the shear modulus. G is defined as $\tau_{XZ} = G\,\gamma_{XZ}$ where τ_{XZ} is the stress applied on the X plane in the Z direction and γ_{XZ} is the corresponding shear strain. Material anisotropy occurs in crystalline solids where the elastic constants vary as a function of crystallographic orientation. From Figure 2 we can see that there are three normal and six shear stress components. Taken reversibility of

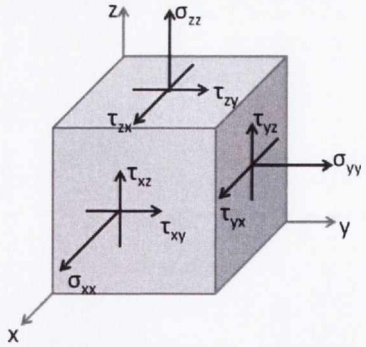


Figure 2. *Stress components acting on a volume element*

elastic strain and symmetry into account, the number of independent constants is reduced from 36 to nine constants for an orthorhombic crystal, five for hexagonal and only three for cubic crystal and the elastic modulus can be calculated for each crystallographic orientation. Another important elastic constant is the Poisson's ratio, v. It is defined as follows: $v = -\varepsilon_{xx}/\varepsilon_{yy}$. Poisson's ratio is a measure of how much the material is deformed in the direction orthogonal to the applied stress. For isotropic materials, there is a simple relationship between E, G and v: $G = E/2(v+1)$.

Materials follow Hooke's Law throughout their elastic range. The latter extends up to fracture for brittle materials. For plastic materials, this range varies greatly depending on the material, but it is always lesser than the full extent of deformation.

Brittle failure

Typical materials behaving this way are ceramics and heavily cross-linked polymers. The maximum stress the material can withstand before it breaks is its ultimate strength. Brittle materials usually exhibit low strain (a few percent at most) but can exhibit very high strengths (up to 95 GPa for diamond[13]). These types of materials are rarely used for engineering applications due to their incapacity to undergo large tensile load. Nevertheless it is not uncommon to find them used for their large compressive strength. Concrete is a prime example of such a material that has a much greater resistance to fracture under compression than under tension.

Plastic failure

When materials fail after they have deformed irreversibly, they have undergone plastic failure. They are many types of plastic responses with a combination of elastic and plastic deformations. Maybe the simplest type is the elastic-homogeneous plastic response which exhibits a stress-strain curve similar to Figure 3. The linear part of the plot is the elastic region that exists only for small strains. At larger strain, the material

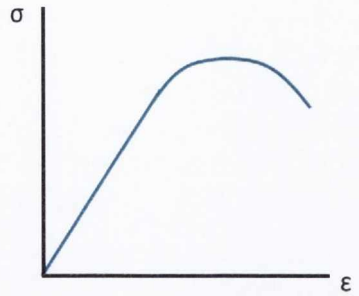


Figure 3. *Typical stress-strain curve for plastic deformation*

starts deforming and the stress-strain curve is parabolic, which is associated with irreversible movement of dislocations in the case of metals and ceramic[11]. The fact that the stress continues to increase after the onset of plastic deformation is a sign of strain hardening, resistance to further plastic deformation by the material. The second part of the curve can be empirically described by the following relationship: $\sigma = K \varepsilon^n$ where n is the strain hardening index or coefficient[14]. We can note that the case of n=1 is for a purely elastic behaviour and the case of n=0 is the case of a purely plastic material. The yield strength is the maximum stress before plastic deformation. The difference between true stress ($F/A_{initial}$) and engineering stress (F/A_{final}) becomes important for plastic deformation since the cross sectional area of the material after plastic deformation can have changed dramatically due to necking. This should be taken into consideration during calculations.

1.1.2. Non-linear materials – polymers

Stress-strain curves are usually highly non linear in the case of polymers, except for highly cross-linked ones. The main reason for this is that stress applied on polymer is not directly transferred into stress applied to covalent or ionic bonds. The main contribution to the strain is a reorganisation of polymer chains within the matrix, so that mechanical deformation initially probes the weak inter-chains forces instead of intra-chain forces. However, due to this reorganisation, the strain hardening coefficient is much higher in polymers, which means that by straining the polymer to a certain level, one can reorganise the structure into a new, more highly oriented and stronger one.

We have introduced and defined the main mechanical properties using the classical tensile test properties. We will now focus on the techniques available to investigate these properties at the nanoscale. Most macroscopic materials are tested using an universal tensile machine. A piece of material of known dimensions is securely placed

between two grips of the tensile machine. A constant force is then applied to the material while the distance between the grips is carefully monitored. However this technique is difficult to employ when the dimensions of the materials are below 100 nm. In addition, scale related phenomena are expected to occur at these small dimensions. For instance, mechanical contact is occurring over such small areas that large pressures can develop at the contact point. Also the large surface area to volume ratio may result in there being a significant contribution of surface atoms to the mechanical characteristics. Hence, new techniques appropriate to nanoscale dimensions and phenomena have been developed. The next section focuses on detailing the techniques and methods used to investigate the mechanical properties of thin films (2D) nanoparticles (0D), and nanowires (1D). We will detail the latter more extensively as it is the main interest of this thesis.

1.2. Techniques to measure mechanical properties at the nanoscale

1.2.1. Two-dimensional systems – thin films

Thin films are two-dimensional nanosystems as they are confined in one direction. They are a heavily studied nanosystem, probably due to their high importance in devices[15-16]. The characterisation of thin films provides a wide range of information on surfaces, interfacial chemistry and mechanical properties. Methods to investigate the mechanical properties of thin films include nanoindentation, bulge testing, substrate curvature and X-ray diffraction[17]. In 2009, Agrawal et al reviewed techniques available for measuring mechanical properties of thin films, nanowires and nanotubes[18]. They drew a schematic summarizing the main experimental techniques developed for testing thin films, reproduced here on Figure 4. Even though the most commonly used technique is

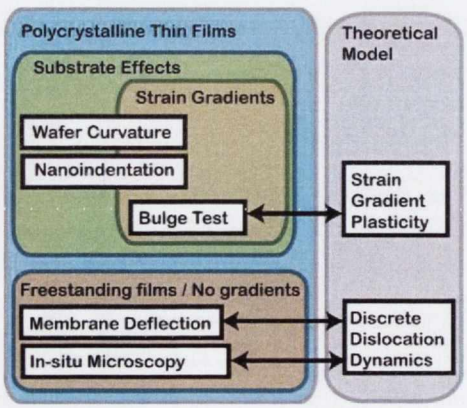


Figure 4. *Schematic summarizing the main experimental techniques developed for testing thin films*[18]

nanoindentation, we will briefly detail the other techniques and then focus on the advantages and recent advances in nanoindentation.

Before the invention of the nanoindenter by Pethica et al[19], the main technique used to study thin film was the substrate curvature method, developed by McInerney et al in 1982[20]. In this method, a laser beam is scanned across the feature of interest on the substrate and the surface curvature is determined by analysing the position of the reflected beam on a photo detector. To induce strain, thin films were deposited on a substrate with different thermal expansion coefficients and the whole system was heated. This method was successfully used by Venkatraman et al[21] in 1992 to separate the causes of film strengthening. Indeed when Doerner et al[22] experimented on aluminium and tungsten thin films there was doubt as to whether the strengthening was due to film thickness effects or to a change in grain sizes with thickness. By using the wafer curvature technique on films of different thicknesses but same grain sizes, Venkatraman et al found that strengthening was inversely proportional to film thickness. It is worth noting that since this technique is fast and non destructive it is applicable to patterned films.

Another interesting technique is the 'bulge test' method, developed on 1992 by Vlassak et al[23]. Free standing films were prepared by micro-machining processes and a uniform pressure was applied to one side of the film. The deflection of the film was then measured as a function of the applied pressure and the pressure-deflection data were converted into a stress-strain curve for the film. This technique was mostly used to determine the Young's modulus and the Poisson ratio of thin films.

X-ray diffraction is a precise and reliable technique to evaluate strain on thin films by measuring interplanar spacings in crystalline materials[17]. Stresses in amorphous materials can also be determined by measuring the strain induced in a crystalline substrate. The main drawback of this technique is the low spatial resolution due to the large diameter of X-ray beams. With a similar approach we can expect Raman spectroscopy to be used to measure the difference in bond strain for elements that exhibit a Raman signal.

While the previous methods mentioned were proven useful, the improvement in the calculation method of hardness, elastic modulus and contact area introduced by Oliver

and Pharr in 1992[24] using indentation made the latter a prime technique for the study of thin films. Indentation of thin films provides a wealth of information[25]: hardness, elastic modulus, stiffness, scratch resistance, film-substrate adhesion, residual stresses, time dependent creep, relaxation properties, fracture toughness and fatigue. Indentation measurements can also assess structural heterogeneities both on and underneath the surface such as diffusion gradients, precipitates, presence of buried layers, grain boundaries and modification of surface composition. Most of these properties are investigated using a nanoindenter. Nevertheless some research groups still use AFM to indent thin films, though mostly to study soft materials[26-28]. However, AFM does not provide enough control of the loading (speed and force measurement precision rather poor), the signal to noise ratio is too low (thermal vibration of cantilever induces noise in the measurement), the stiffness of the cantilever is limited (stiffer probes needed for hard materials) and the shape of the tip is not controllable.

Since Oliver and Pharr introduced a method to measure hardness and elastic modulus with a nanoindenter in 1992[24], a significant amount of improvements have been made, mostly to rule out uncertainties arising from the presence of strain gradients and substrates effects. Oliver and Pharr reviewed in 2004[29] most of these advances, how it deepened their knowledge of the elastic-plastic contact and discussed the limitations of these techniques. One of the main breakthrough in the field was reported by Stach et al in 2001 when they developed a nanoindenter able to perform measurements in situ during electron microscope obervation[30]. This set up enabled Minor et al to provide a new view on the onset of plasticity in aluminium films[31]. Figure 5 displays the change in dislocations before and after indentation. The authors reported that very small forces were sufficient to trigger plasticity in a dislocation-free Al grain. Interestingly, these small forces correspond to shear strengths on the order of the theoretical limit for aluminium (2.2 GPa). Interestingly the same grain of Al after indentation resulting in 10^{14} m^{-2} dislocation density can withstand shear stresses close to the theoretical shear strength, which is contrary to previous results stating that only a dislocation free material could support such high stresses[32].

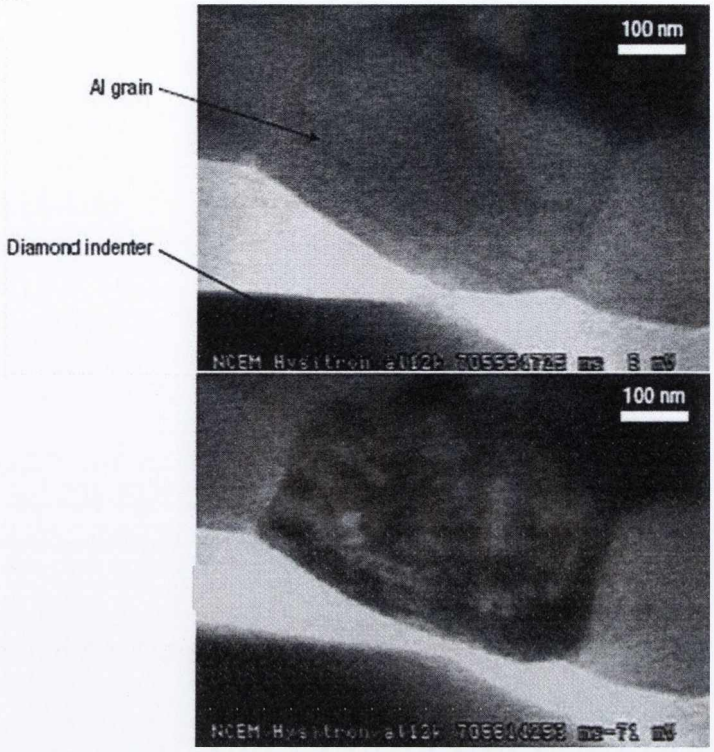


Figure 5. *TEM images of an Al grain before and after indentation in situ TEM[31] showing large amount of dislocations after indentation*

The ability to characterise the mechanical properties of thin films is paramount for their integration into devices and for a general understanding of plasticity, dislocation movements and contact effects. Indentation measurements represent the bulk of work carried out on this subject. It is a reliable, reproducible, highly controllable technique that provides a significant amount of information about the system under study and its mechanical deformation. The development of in situ TEM measurements opens the way to a better understanding of the mechanical properties of thin films. We will detail the principle of TEM and its operation in section 2.4.

1.2.2. Zero-dimensional systems – nanoparticles

Nanospheres and nanoparticles are of particular interest in domains such as catalysis[33], fluidics[34], sensors[35], polymer composites[36] and synthesis[37]. The three-dimensional confinement of nanoparticles makes them an attractive system where strain and deformation are concentrated in a small volume. In addition, these small volumes containing few atoms allow the construction of models that are very close to reality. Comparison of simulations and experiments can then lead to improvements in both. However, experimental techniques to study the mechanical properties of nanoparticles

are scarce. Only one method has been used repeatedly: nanoindentation but has lead to discovering interesting properties.

In 1995, Schaefer et al[38] reported on the use of a home-built AFM to indent gold clusters deposited on an atomically flat surface. In this paper they provide a detailed experimental procedure to image and indent the nanoclusters and calibrate the cantilever. They compare the load-displacement plot for indentation on the clusters and on sapphire. The authors found that annealed clusters with sizes between 3 and 18 nm showed an elastic modulus about two third of bulk Au. The modulus of unannealed clusters was half of annealed ones. The authors also showed that the AFM can fracture the gold clusters.

In 2003, Gerberich et al[39] reported on superhard silicon nanospheres. Using a combination of experiments and computational simulations the authors showed that these nanospheres had a hardness about four times that of bulk Si. Dislocation injection and reverse plastic deformation were observed and accounted for in the determination of the hardness. While some groups use nanoindentation on its own to characterise nanoparticles, the bulk of the work is carried out in situ TEM which provides atomic resolution changes during plastic deformation while controllably indenting the particle. In addition, the analysis of metal indentation is quite difficult because of the native oxide layer. When indenting the surface, the tip first encounters the oxide layer and needs to fracture it before it can indent the metal surface. This interfacial layer makes analysis complicated. By indenting the sample directly using in situ TEM one can clearly visualise when the tip starts having an effect on the metal.

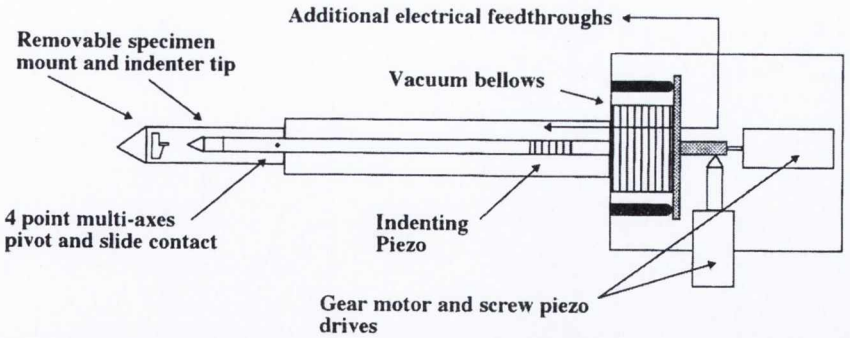


Figure 6. *Schematics of indentation specimen holder showing the general design and construction*[40]

Kizuka et al[40] published the design of an in situ piezo driven specimen holder in 1997 to study the contact of Au surfaces between two Au tips. However Wall and Dahmen were the first ones to report the design and fabrication of an in situ nanoindenter[41], pictured on Figure 6, which they used to indent Si wedges. They subsequently improved their design to study the onset of deformation on aluminium films[30,42]. This new nanoindentation holder allows coarse and fine movements in three directions. Using this tool, Deneen et al reported on the deformation of silicon nanospheres in situ TEM[43]. Elastic contacts (tip/particle and particle/particle), strain fields and plastic deformation were investigated and the onset of fracture was identified. This first report illustrates the use of in situ TEM nanoindentation and provides results that are not available using another technique. Using the holder described previously, Shan et al reported on ultra high stress and strain of hollow nanospheres[44]. The authors found that spherical nanocrystalline CdS particles are able to withstand stresses close to the theoretical shear strength and exhibit strains up to 20 % making these hollow particles extremely interesting.

Another interesting systems measured by nanoindentation were Si clusters investigated using in situ TEM by Lockwood et al[45] in 2008. This work not only focused on the hardness of 50 nm diameter Si nanospheres but also studied the nanospheres interaction within the cluster, to access dynamical mechanical properties. It was established that at small loads, the main deformation mode to relieve the applied stress was a rotation of the spheres. For larger applied loads, the particles fractured at the amorphous silicon interface. Figure 7 shows a series of TEM images during loading. Figure 7a was taken before loading, then Figure 7b to d are images after respectively the first, second, third and fourth loadings. The rotation of the nanoparticles can be seen

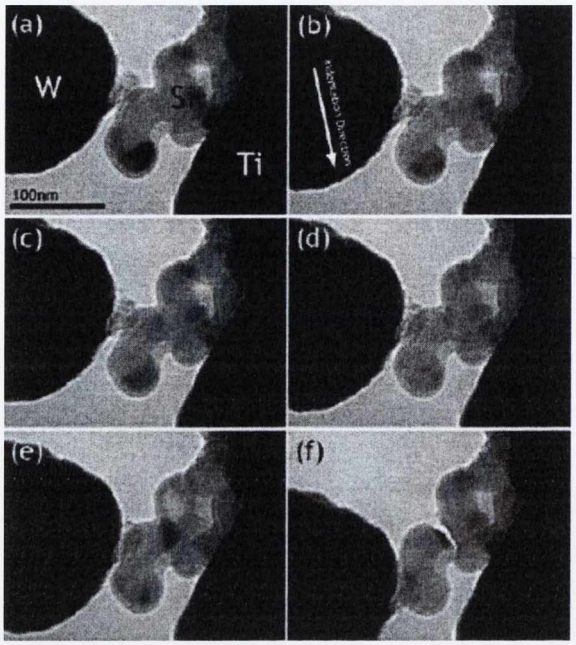


Figure 7. *Series of TEM images during compressive loading of Si nanospheres by a tungsten tip[45]. (a) image taken before loading, (b) to (e) respectively first to fourth loadings showing change in Bragg, (f) fracture of clusters.*

due to the change in Bragg contrast throughout the clusters. Figure 7f shows the fracture of the clusters. The formation of the crack resulted in a sharp decrease in elastic strain within the cluster and almost the separation of 2 nanoparticles from the cluster body. The contact pressure at the time of fracture was 17.6 GPa, which is 30 % greater than the hardness of bulk Si.

Mechanical measurements on nanoparticles are interesting because of their small volume where the strain has to be concentrated. The main technique used for this investigation is indentation, either ex situ on an AFM or nanoindenter or in situ TEM. Interesting properties were reported such as super hard silicon, onset of fracture on Si wedge, ultra strong CdS hollow spheres and mechanism for stress relief in nanoclusters. The most efficient way to study these behaviours is by directly following the changes in strain, plasticity and size inside a TEM while applying load. The obvious difficulty of this technique is the design and fabrication of an appropriate nanoindenter sample holder which has only been reported by a couple of groups.

1.2.3. One-dimensional systems – nanowires

At the nanoscale, one-dimensional (1D) systems are of particular interest as the reduction in lateral dimensions should result in the decrease of defects per unit length,

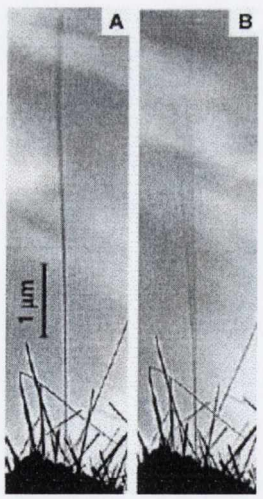
hence increasing the strength of materials[46].It is expected that during nanowire growth the defects would be expelled at the surface as it requires more energy to create them. This assumption is open to debate amongst scientists but is the groundwork of nanomechanics. Not only could the strength of nanoscale materials increase compared to bulk but they could demonstrate new properties as a result of this enhanced strength. For instance, nanowires able to resist high fracture stress would be able to overcome shear stresses and nucleate ductile dislocations or make them mobile. This would make materials that are brittle in bulk form show ductile behaviour at the nanoscale[47]. However due to their dimensions (usually below 100 nm in width), measuring the mechanical properties of 1D nano-systems is very challenging. The most studied systems probably are carbon nanotubes, silicon and ZnO nanowires due to their extensive range of applications. For the past decade groups all over the world have developed ingenious ways to study the mechanical properties of nanowires, nanotubes, nanorods and nanobelts[48]. Techniques used can be split into two categories: in situ electron microscope (EM) and AFM based. We will now detail these techniques and discuss their applications.

In situ TEM/SEM – oscillations (thermal and voltage driven)

The discovery of carbon nanotubes (CNTs) by Ijima in 1991[49] and calculations[50] of their properties raised great expectations for their modulus and strength[51-53] , which were estimated to be of the order of 1 TPa and at least 20 GPa respectively[54]. However their mechanical properties eluded direct measurements until Treacy et al reported for the first time in 1996 the measurement of the Young's modulus of thermally oscillating carbon nanotubes[55] inside a TEM. They attached a bundle of CNTs to the edge of a TEM grid, brushed the tip of the bundle with tweezers, producing horizontally aligned tubes clamped at one end. The TEM was equipped with a heater holder that could reach 1100 K. The CNTs were thermally vibrated from 300 K to 1100 K and the amplitude of their oscillations was recorded. It was found that the Young's modulus was in the terapascal range, much higher than previously reported graphite fibers[56] but in good agreement with simulations[50]. Thermal oscillations provide a good estimate of the modulus but fail to provide additional information on the mechanical properties such as strength or failure mechanism. Also the error in determining the amplitude of the oscillations is

quite large. Nevertheless the technique demonstrated in this paper opened up developments for mechanical testing inside a TEM.

In 1999, Poncharal et al described their innovative method of electric field induced resonant excitations of CNTs in situ TEM[57]. This technique is quite powerful because a significant amount of information can be extracted from the same set-up used in different ways. Carbon nanotubes were attached to a thin gold wire and inserted inside the TEM chamber at a close distance from a counter electrode. First, a static potential was applied to the wire which caused the CNT to charge and become attracted to the counter electrode. In this case, the CNTs of interest were the ones that were not perpendicular to the electrode, as only these could bend towards it and their elastic deformation could be investigated. It was then found that a MWCNT of 20 nm in diameter could bend to a radius of curvature at least as small at 80 nm and recover its straight configuration. This first result gave great insight into the elastic properties of carbon nanotubes. A second experiment using the same set-up was to apply an oscillating voltage to the wire, resulting in dynamic deflection of the CNT and tune this



potential to obtain resonant excitations as shown on Figure 8. On Figure 8A the end of the CNT is blurry due to thermal oscillations. Figure 8B shows the wire oscillating at its

Figure 8. *TEM micrographs of (A) CNT standing and (B) oscillating at its resonance frequency*[57]

resonance frequency from which the modulus was extracted, knowing the length and diameter of the tube. The modulus was plotted against diameter and was found to show a sharp decrease at diameter of 12 nm and above from around 1 TPa to 0.4 TPa. This

drop at larger diameters is attributed to a wavelike distortion which is the energy favourable bending mechanism for larger diameter nanotubes.

This same technique was also used as a nanobalance with a range in the pico-to-femto-gram when a nanoparticle was placed at the end of the CNT. A very similar method was developed in 2006 by Chen et al inside an SEM[58] to investigate the modulus of ZnO nanowires. The much larger size of the SEM chamber compared to TEM, makes this technique easier to carry out, and thus making possible the study of different 1D systems.

Although, in situ oscillations studies in SEM or TEM constitute a valid approach to determining the elastic modulus of nanowires and nanotubes but there is a significant error due the estimation of the oscillation amplitude. In addition this technique does not make use of the full potential of TEM and its atomic resolution capabilities. These methods also fail to provide values for the strength as the material is only oscillated not plastically deformed or broken. In situ oscillations measurements provide a simple, fast and non-destructive approach to determine the modulus of one-dimensional nanosystems. If more information on the material is needed another technique must be used: tensile measurements in situ TEM/SEM.

In situ TEM/SEM – tensile

Many groups have described different approaches to tensile testing on a TEM stage in an attempt to reproduce this well tested mechanical characterisation method. The large amount of insight provided by tensile testing makes it a particularly compelling approach on the nanoscale. In 2000, Yu et al[59] used a nano-stressing stage inside a Scanning Electron Microscope (SEM) and recorded the entire experiment on video, enabling real-time characterization of the deformation. In these experiments, individual MWCNTs were picked up and attached onto the opposing tips of AFM cantilever probes, as seen in Figure 9. Mechanical failure was observed to occur in the outermost layer, following the 'sword-in-sheath' model. However, since only the outermost layer was bonded to the AFM tip, once this one broke, the other layers tended to slide, which the authors reported as pullout length. This experiment mimics quite accurately a classical macro scale tensile load experiment and hence allows the calculation of a wide range of mechanical properties, such as the force at fracture, the Young's modulus and the

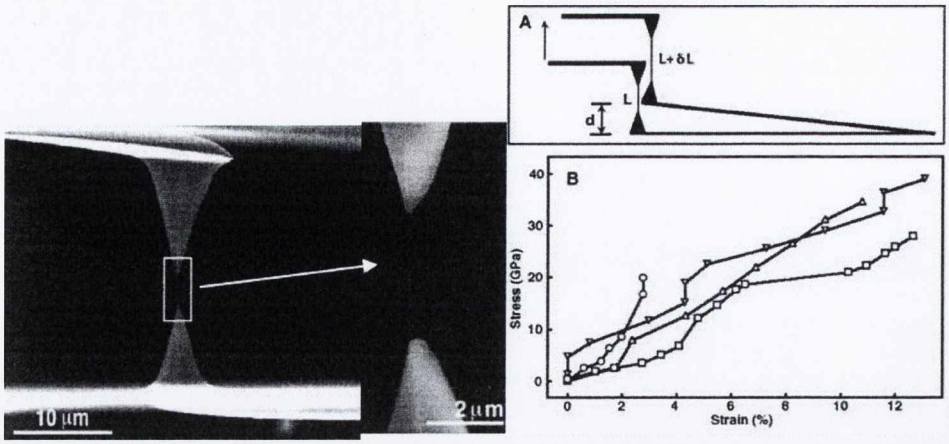
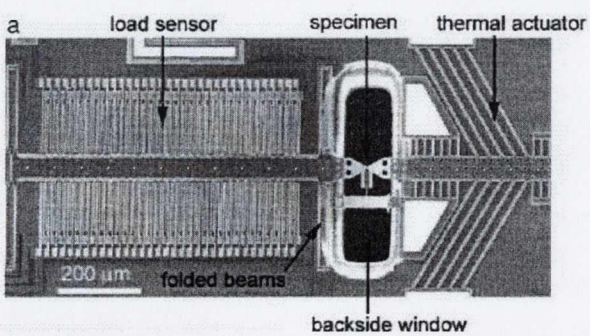


Figure 9. *Left hand side: SEM images of the two AFM cantilevers holding a MWCNT. Right hand side: A. Schematic showing the principle of the tensile loading experiment. When the top cantilever is driven upwards, the MWCNT stretches and brings the lower cantilever with it. B. Plots of stress versus strain for individual MWCNT*[59]

tensile strength. These were found to range from 270 to 950 GPa and from 11 to 63 GPa, respectively. TEM imaging also revealed different fracture patterns such as wavelike structures, ribbon-like distortions and radial collapses[60]. The values obtained by this technique are in good agreement with previous calculations[54]. However, the stress-strain curves obtained (see Figure 9B) are quite noisy and the authors reported that at least half of the MWCNTs would become detached at one of the end during the tensile test. While providing convincing data on the mechanical measurements of carbon nanotubes, this technique lacks repeatability and controllability. Tensile testing should be performed by a specifically designed device allowing great control over the displacement and force applied.

Such a device was reported in 2005 by Zhu et al who designed and fabricated a



microelectromechanical system (MEMS) that allowed controlled tensile measurements and atomic resolution imaging, simultaneously[61]. They built the device portrayed in Figure 10 that consists of an actuator and a load sensor (with nN resolution capability)

Figure 10. *In situ EM tensile testing device including actuator, load sensor, and specimen. Four folded beams support the load sensor*[61]

based on capacitance measurements. Thanks to its small size the device can be used in situ in SEM and TEM and its versatility makes it possible to study thin films, nanowires, nanotubes and biological samples. This technique is very well thought through and provides great insight in the deformation and fracture mechanism of a wide range of materials. In the particular case of 1D nanostructures, strain-stress curves were generated both by in situ SEM and TEM for a Pd nanowire and a MWCNT, respectively. A micromanipulator was used to position the nanowire across the MEMS and the latter was secured by electron beam induced deposition (EBID) of platinum on each side of the structure. The MEMS was then activated and tensile load was applied to the nanowire while continuously monitoring the wire deformation. The results from the TEM provide information on the fracture mechanism as shown on Figure 11 and the authors recorded

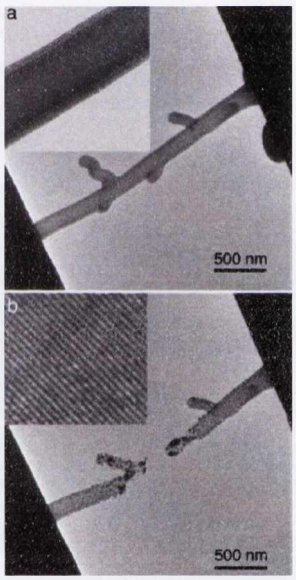


Figure 11. *TEM micrographs of a MWCNT across the MEMS (a) before the test and inset is HRTEM of MWCNT, (b) after the test and inset shows crystalline particle embedded in amorphous matrix surrounding MWCNT*[61]

a real-time video of the nanotube deformation. This technique, in contrast with the others described so far provides a value for CNT strength, which in the case of MWCNT was estimated at 15.84 GPa. In addition, the inset of Figure 11B shows a crystalline particle embedded in an amorphous matrix surrounding the MWCNT. HRTEM and diffraction confirmed this particle to be Pt from the EBID process which impairs high resolution imaging of the tube. In 2009, Agrawal et al[62] reported on the tensile deformation of ZnO nanowires using this MEMS. They compared their experimental results to computational modelling and found that the NWs showed fracture stresses up

to 9.53 GPa and strain up to 6.2 %. However the simulations predicted a phase transformation which was not seen experimentally.

The design and fabrication of the MEMS is by itself a breakthrough, allowing different materials to be tested and mechanical properties to be investigated. MEMS are an excellent tool that can provide reliable values for strength and modulus of nanowires. So far it has only been used at room temperature and temperature dependent studies should provide interesting results, comparable to those reported in the following study.

In 2005, Huang et al jointly studied electronic transport and atomic scale deformation of MWCNTs[63] in situ TEM. This first study was mainly focussed on the contact and transport of MWCNTs. By passing a current of 240 μA through the MWCNT, electric breakdown occurred in a wall-by-wall fashion. Our interest in this paper lies in the piezo manipulator set-up displayed on Figure 12 that was used in another study in 2006 by the same

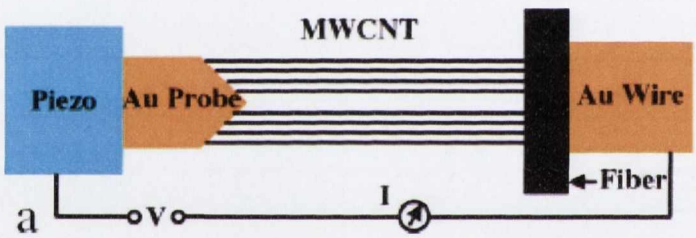


***Figure 12**. Schematics of piezo- manipulator. MWCNT grown on carbon fiber attached to STM probe*[64]

authors[64]. In this work, the authors studied plasticity in SWCNTs at high temperature. The piezo manipulator was used to pull a 24 nm long SWCNT to increase the strain at a constant bias of 2.3 V; the temperature in the centre was estimated to be around 2000 C. At this temperature, the SWCNT showed superplastic deformation with an elongation of 280 % and its diameter was reduced 15 times before breaking, as shown on Figure 13a-d. Figure 13e-f displayed TEM micrographs of the experiments carried out at room temperature which showed a maximum strain of only 15 %. Arrowheads identify kinks which the authors claim are responsible for the superplasticity through their nucleation and motion; arrows indicate features at the ends of the nanotube that are almost unchanged during elongation. This technique gives very interesting qualitative results but fails to provide quantitative values for the modulus or strength.

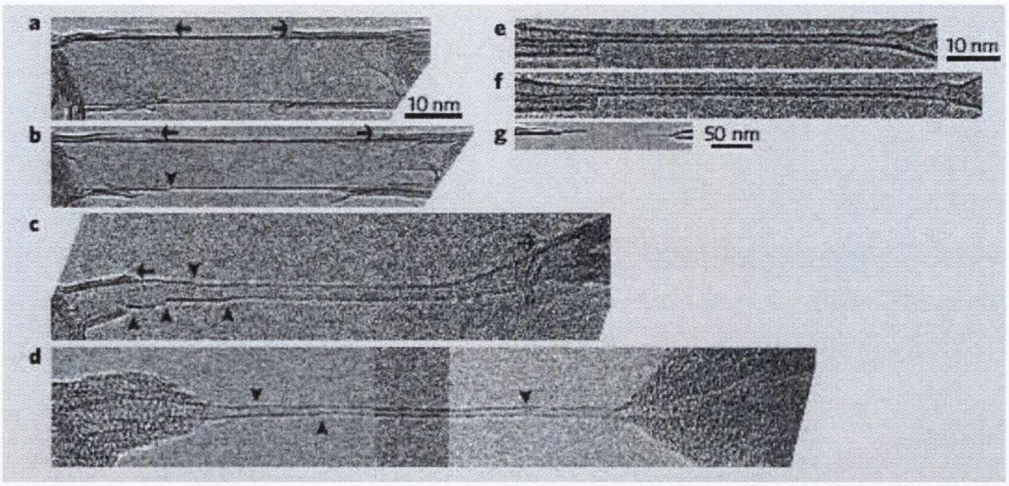


Figure 13. *TEM micrographs of SWCNT under tensile load[64] at (a-d) high temperature (around 2000 C) with arrowheads identifying kinks responsible for the superplasticity observed and (e-g) room temperature which showed a maximum strain of only 15 %*

The techniques described so far required the fabrication of an in situ holder for mechanical measurements. To avoid this time consuming and expensive design, Han et al developed in 2007 a technique allowing mechanical deformation of SiC nanowires and HRTEM imaging simultaneously[47,65]. Nanowires were deposited on a TEM grid covered with specially designed colloidal film. Under electron beam radiation the celloidin/carbon thin film linearly contracts (usually 4-5 %) due to polymerisation shrinkage. When the film was heated up, it curved hence bending nanowires lying on top of it. Figure shows TEM micrographs taken at several time intervals and displaying the

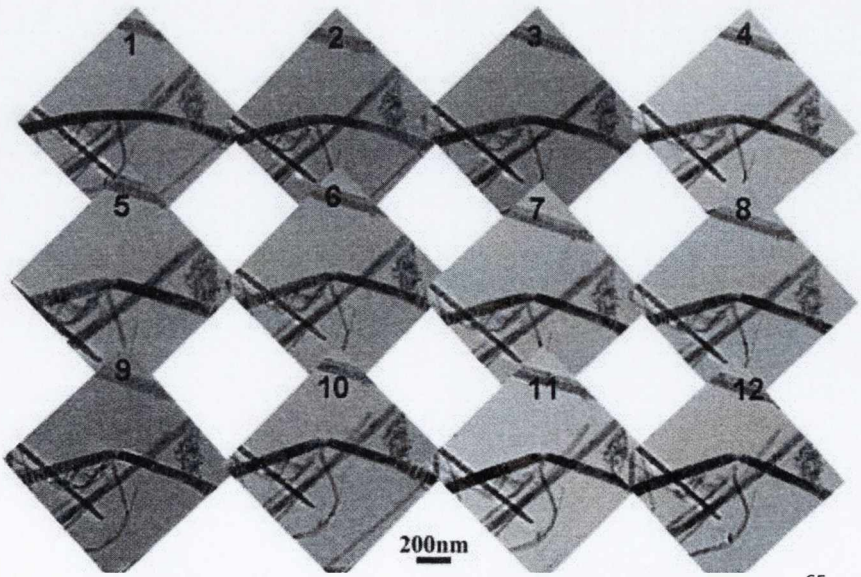


Figure 14. *TEM micrographs of a SiC during mechanical deformation[65]. The plastic deformation was triggered from the second image*

plastic deformation of a SiC nanowire. Of the 20 nanowires investigated, all showed elastic strain (up to 2 %) but 4 of them revealed plastic deformation accompanied with much larger strains. Interestingly, the fracture was not crystalline but the nanowire had transformed from crystalline to amorphous at the most strained region. High resolution TEM images of this area show classic bending induced tensile-compressive features except for the presence of an asymmetric feature in the strained field (X-shaped amorphous region). The images revealed that the plastic deformed area is a combination of disordered atomic planes, bent lattices and amorphous regions. The elastic-plastic transition was also investigated and was characterized by homogeneous lattice distortion, dislocation nucleation and lattice relaxation in the compressed side of the bent SiC nanowire. This was the first time SiC was seen to deform in a plastic fashion in contrast with its bulk counterpart. The occurrence of this phenomenon close to room temperature is quite surprising and opens new potential applications for nanoscale SiC. Zhang et al, part of the same group, reported on β-SiC nanowires using, HRTEM imaging and tensile measurements in situ SEM[66]. Moreover, later during that year the same authors reported on the plasticity of Si nws[47] using the same technique. Single crystal Si nanowires of diameters between 15 and 70 nm were studied and they demonstrated a reduction in diameter of up to 426 % and an elongation ratio up to 125 % upon tensile deformation. From Young's modulus calculations, the authors suggested a brittle to ductile transition diameter of around 60 nm at room temperature. In addition to commenting on the stiffness of these nanowires, the authors discussed the occurrence of plasticity in terms of surface-effect driven phenomena. The emergence of a high density of dislocations during deformation is the prime cause of this large strain plasticity which is then followed by the formation of disordered crystalline structures and finally amorphization and plastic necking leading to failure. Further work was carried out by the authors and in 2009 they reported on the atomic mechanisms governing the elastic limit and plasticity of bending Si nanowires[67]. Positional-resolved atomic level strain distribution (PRALSD) was calculated and mapped onto the HRTEM images of the nanowire as seen on Figure . A shift of the neutral strain axis from the compressive zone to the tensile zone was demonstrated. The authors suggested that this phenomenon was due to the tensile surface atomic steps and the compressive buckling which in turn facilitated plasticity by initiating ductile plastic dislocation events. This technique is

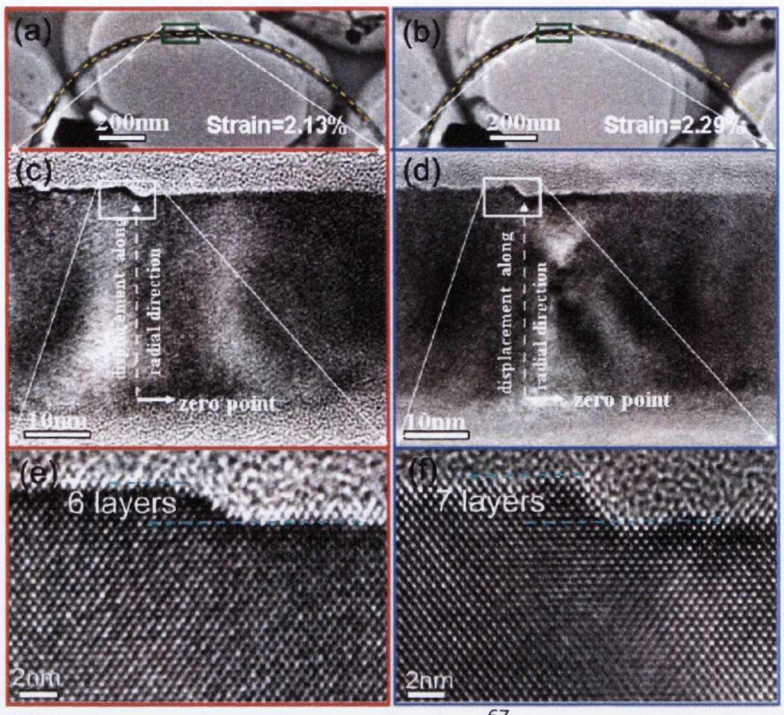


Figure 15. *TEM micrographs of Si nanowire bent[67]. Low resolution (a, b); (c, d) enlarged images from the green framed regions on (a, b); (e, f) enlarged images from the white framed regions on (c, d).*

particularly interesting because of its simplicity and the high quality of atomic resolution imaging provided. Plastic deformation of SiC and Si nanowires and their atomic mechanisms were analysed. However the only data accessible is the strain. The authors have not yet found a way to measure the force applied by the film on the nanowires and hence stress-strain curves could not be measured.

While the techniques presented in this section provide great insight in the deformation of materials, TEM is an expensive and time-consuming tool that is not available in every lab. In addition in situ mechanical measurements tools (MEMS) either take years to build or are very expensive to purchase from the TEM suppliers. Groups who do not have access to these tools have found other ways to study the mechanical properties of one-dimensional systems, mainly using AFM.

AFM based techniques – Indentation

Indentation is commonly used to study the mechanical properties of films. It involves the controlled vertical loading of a well defined-shape tip (indenter) on a surface and its withdrawal. Indentation is particularly interesting for the study of plasticity, hardness and ductile deformations and is quite powerful due to the wide range of tip shapes that can be studied. However, for one-dimensional systems nano-indentation is problematic because of the need to visualise the NW before performing the test. This could be overcome by the use of an AFM as both the visualisation tool and the nano-indenter. This in turn creates a new problem due to the shape of the AFM tip and the stiffness of the cantilever. AFM tips are usually pyramidal shaped, making it close to impossible to indent perpendicularly to the surface of the NW and causing slippage and friction issues. An alternative to this problem was reported by Li et al[68] in 2003 where they used a combination of AFM and nano-indenter to study the mechanical properties of silver nanowires. A Berkovich diamond tip was used to image, locate nanowires on the surface and indent with different loads at specific points on the NW. AFM was then used to get a better picture of the NW and the indentation shape. Figure shows a representative

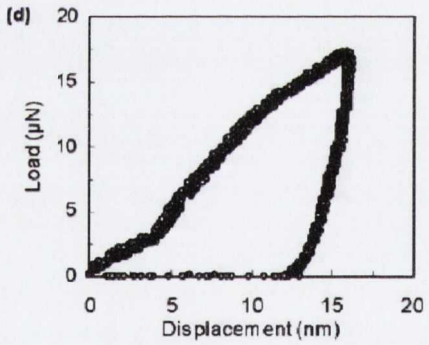


Figure 16. *Typical load-displacement curve for an Ag NW*[68]

load-displacement curve for an Ag NW. Penetration depth of the tip into the NW was around 15 nm, which represents about 30 % of the wire diameter, enabling the authors not to take into account the surface hardness. In addition there is a distinct change of slope at a load of 2.5 μN, indicative of plastic deformation associated with dislocation nucleation and motion. They found the hardness and Young's modulus of the silver NW to be 0.87 and 88 GPa respectively, both values are in good agreement with bulk silver. The authors used the standard Oliver Pharr method[24] to calculate hardness and elastic modulus which is based on the indentation of a half space. This assumption works well

for thin films but is debatable for one-dimensional systems. A similar technique was used by Mao et al[69] to study the hardness of ZnO nanobelts.

In 2006, Feng et al[70] reported on the mechanical properties of GaN and ZnO NWs using a nano-indenter with scanning capabilities. In comparison with the previous technique, the authors developed a model that takes into account the tip/NW and the NW/surface interfaces. As first order estimations for the hardness of the materials it was established that the Oliver Pharr method provides a lower bound while the Joslin Oliver[71] hardness provides an upper bound.

Indentation of nanowires is quite seldom performed and mostly provides a measure of the hardness of the material. The effect of the substrate is the main problem, especially for small nanowires. Indentation measurements on one-dimensional nano-systems provide a lesser amount of information on the deformation mechanism than other techniques. It also fails to measure the strength of nanowires and nanobelts, a parameter of paramount importance for the implementation of nanowires into devices. While indentation is extremely commonly used for the study of mechanical measurements of thin films, it is a less attractive method for one-dimensional nano-systems. The bulk of mechanical measurements studies on nanowires using AFM was carried out using bending and tensile techniques.

AFM based techniques – Bending and tensile

AFM is a particularly suitable tool for studying bending of nanowires, providing a wide range of information. The AFM tip can be used as a probe to bend and relax the nanowires, therefore studying both elastic and plastic deformation. The tip can also break the wire giving a measure of the strength, which is difficult to access by other means. Manipulation with the AFM can also provide qualitative information on the elasticity of nanowires. The latter was performed by Falvo et al in 1997 who used the tip of an AFM to bend and buckle MWCNTs through large angles without breaking them[72]. This first report on the subject was more qualitative than quantitative as the force applied to the nanotube could not be calculated because of the friction component on the surface. This article however shed light on how flexible and elastic CNTs can be and opened the way to AFM-based mechanical testing of nanowires.

Later that year, Wong et al[73] studied the elastic strength and toughness of silicon carbide nanorods and multi-walled carbon nanotubes (MWCNT) using an AFM based techrique. The nano-materials were first dispersed on a flat surface, and pinned to it by a lithographically patterned array of SiO squares. An AFM tip was then used to directly measure Force-displacement (F-d) characteristics at different distances from the pinning points and hence Young's modulus and bending strength were determined. In addition, a lower bound for stored strain energy was calculated and showed to be about 10 times higher in MWCNT than in SiC nanorods. This experiment highlighted the potential applications of MWCNT and carbide rods as reinforcement in ceramics or polymer composites.

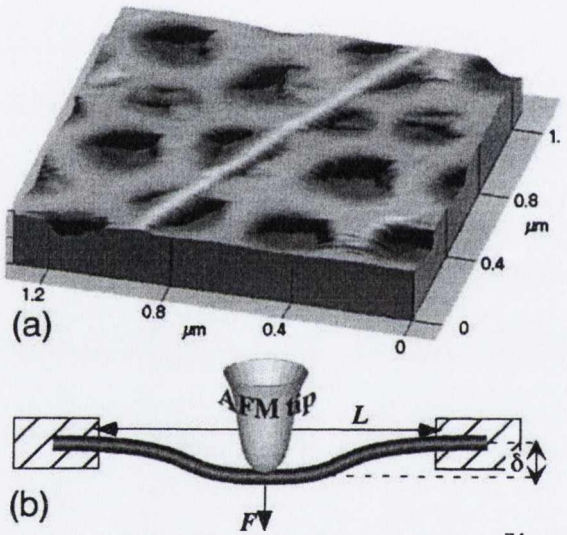


Figure 17. *a) AFM image of SWCNT rope lying over a pore[74]. b) Schematics of AFM bending test*

In yet another study of carbon nanotube Salvetat et al[74] reported on the first elastic properties measurements of crystalline SWCNTs ropes using a three-point bending AFM technique. SWCNTs ropes were dropped on a porous alumina filtration membrane with ropes spanning over holes, as shown on Figure a. An AFM tip loaded the ropes normal to the plane of the substrate and the resulting deflection was a measure of the force applied as shown on Figure b. The adhesion of the CNTs to the alumina surface was enough to provide a strong clamped configuration and prevent slippage. CNTs ropes showed linear elastic response up to 3nN of applied force. A significant increase of the elastic modulus with decreasing diameter was reported with the elastic modulus in the region of 1 TPa for the smallest ropes and the shear modulus around 1 GPa. This

technique, while providing a valid estimation of the modulus, fails to provide values for strength or strain. More recently, Zhou et al[75] performed finite element analysis to show how the Young's modulus can be underestimated using this method due to boundary conditions and aspect ratio of the nanowire. In addition a similar three-point bending technique, resonance contact AFM where an oscillating voltage excited the tip while in contact with the spanning beam was used to study the elastic properties of polypyrrole[76], silver and lead[77] nanowires.

Another AFM based technique was developed by Song et al[78] in 2005 and has the key advantage of being non destructive towards the nanowire. An AFM in contact mode scanned the surface covered with vertically aligned nanowires. The elastic modulus was determined by simultaneously recording the topography and lateral force when the tip

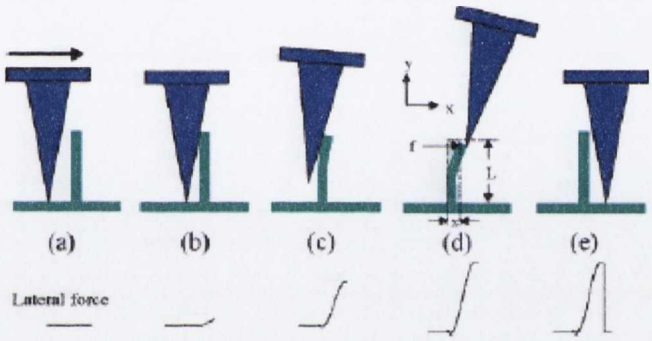


Figure 18. *Procedure to measure the elastic properties of an individual nanowire*[78]

scanned across the aligned arrays, as shown in Figure . Prior to touching a nanowire, a small lateral force is observed (Figure b). When the tip comes in contact with the wire, the force increases almost linearly as the nanowire is elastically bent from its equilibrium position (Figure c). At the largest deflection (Figure d), the tip crosses the top of the wire and the nanowire is then released (Figure e). This technique was recently improved by Hoffmann and coworkers[79] by setting up an AFM inside an SEM. The AFM tip was used to bend vertical silicon nanowires until fracture. The maximum stress before fracture was then calculated and found to be 12 GPa. In addition, a simulation of the stress showed that the maximum stress was generated at the pinning point of the wire. A correlation between strength and length was also reported, such that shorter nanowires tend to have a greater fracture strength than longer ones.

In 2005, Wu, Heidelberg et al[5] reported on a technique where an AFM tip laterally loads a nanowire spanning over a trench. This technique will be more explicitly explained in section 2.2.1.

Conclusion

Mechanical measurements of one-dimensional nanosystems are mostly studied by in situ EM and AFM. The former is mostly used for vibration and tensile experiments while the latter is used for bending and indentation experiments. The main advantage of in situ EM testing is the accuracy in determining the dimensions and the possibility of following in real time with atomic resolution the deformation of the material, though these are usually very challenging experiments which require home-built systems. The advantage of the AFM-based techniques is that they are much easier to carry out and a wide range of properties can be easily extracted from the experiment (modulus, strength, toughness, brittle/elastic fracture mechanism).

AFM based measurements are technically easier to perform than in situ TEM ones but the bending component in the deformation of the nanowire is difficult to analyse. Purely tensile measurements are much easier to study and model but they are extremely difficult to set up experimentally. While AFM measurements can provide statistics on a NW system it does not provide information on the atomic structure changes during deformation and failure. In situ TEM measurements provide the latter information but need a special home-built nano-manipulator to carry out the experiments, which are usually made on a small amount of nanowires. In Chapter 4 of this thesis we will discuss an approach we have taken that does not involve manipulating the nanowires in any way but provides interesting insights into the deformation and atomic strain of nanowire.

References

(1) Moore, G. E. *Electronics* **1965**, *38*.

(2) http://www.itrs.net/Links/2009ITRS/Home2009.htm 2009.

(3) Wu, X.; Kulkarni, J. S.; Collins, G.; Petkov, N.; Almecija, D.; Boland, J. J.; Erts, D.; Holmes, J. D. *Chemistry of Materials* **2008**, *20*, 5954.

(4) Law, M.; Goldberger, J.; Yang, P. *Annual Review of Materials Research* **2004**, *34*, 83.

(5) Wu, B.; Heidelberg, A.; Boland, J. J. *Nature Materials* **2005**, *4*, 525.

(6) Wu, B.; Heidelberg, A.; Boland, J. J.; Sader, J. E.; Sun, X.; Li, Y. *NanoLetters* **2006**, *6*, 468.

(7) Heidelberg, A.; Ngo, L. T.; Wu, B.; Phillips, M. A.; Sharma, S.; Kamins, T. I.; Sader, J. E.; Boland, J. J. *NanoLetters* **2006**, *6*, 1101.

(8) Ngo, L. T.; Almecija, D.; Sader, J. E.; Daly, B.; Petkov, N.; Holmes, J. D.; Erts, D.; Boland, J. J. *Nano Letters* **2006**, *6*, 2964.

(9) Wen, B.; Boland, J. J. *Physical Review Letters* **2008**, *101*, 175502.

(10) Almecija, D.; Blond, D.; Sader, J. E.; Coleman, J. N.; Boland, J. J. *Carbon* **2009**, *47*, 2253.

(11) Hertzberg, R. W. *Deformation and Fracture Mechanics of Engineering Materials*; John Wiley & Sons, Inc, 1996.

(12) Kaye, G. W. C.; Laby, T. H. *Tables of Physical and Chemical Constants*; Longman: London, 1973.

(13) Roundy, D.; Cohen, M. L. *Physical Review B* **2001**, *64*, 212103.

(14) Hollomon, J. H. In *Transactions of the American Institute of Mining, Metallurgical and Petroleum Engineers* 1945; Vol. 162, p 268.

(15) Wilk, G. D.; Wallace, R. M.; Anthony, J. M. *Journal of Applied Physics* **2001**, *89*, 5243.

(16) Dimitrakopoulos, C. D.; Malenfant, P. R. L. *Advanced Materials* **2002**, *14*, 99.

(17) Vinci, R. P.; Vlassak, J. J. *Annual Review of Materials Science* **1996**, *26*, 431.

(18) Agrawal, R.; Espinosa, H. D. *Journal of Engineering Materials and Technology-Transactions of the Asme* **2009**, *131*.

(19) Pethica, J. B.; Hutchings, R.; Oliver, W. C. *Philosophical Magazine a-Physics of Condensed Matter Structure Defects and Mechanical Properties* **1983**, *48*, 593.

(20) McInerney, E. J.; Flinn, P. A. *Proceedings of the 20th IEEE IRPS Symposium New York* **1982**.

(21) Venkatraman, R.; Bravman, J. C. *Journal of Materials Research* **1992**, *7*, 2040.

(22) Doerner, M. F.; Gardner, W. D. N. *Journal of Material Research* **1986**, *1*, 845.

(23) Vlassak, J. J.; Nix, W. D. *Materials Research Society Symposium Proceedings* **1992**, *7*, 3242.

(24) Oliver, W. C.; Pharr, G. M. *Journal of Materials Research* **1992**, *7*, 1564.

(25) Bhushan, B.; Li, X. D. *International Materials Reviews* **2003**, *48*, 125.

(26) Domke, J.; Radmacher, M. *Langmuir* **1998**, *14*, 3320.

(27) Dimitriadis, E. K.; Horkay, F.; Maresca, J.; Kachar, B.; Chadwick, R. S. *Biophysical Journal* **2002**, *82*, 2798.

(28) Vanlandingham, M. R.; McKnight, S. H.; Palmese, G. R.; Elings, J. R.; Huang, X.; Bogetti, T. A.; Eduljee, R. F.; Gillespie, J. W. *Journal of Adhesion* **1997**, *64*, 31.

(29) Oliver, W. C.; Pharr, G. M. *Journal of Materials Research* **2004**, *19*, 3.

(30) Stach, E. A.; Freeman, T.; Minor, A. M.; Owen, D. K.; Cumings, J.; Wall, M. A.; Chraska, T.; Hull, R.; Morris, J. W.; Jr., A.; Zettl, U. *Microscopy and Microanalysis* **2001**, *7*, 507.

(31) Minor, A. M.; Syed Asif, S. A.; Shan, Z.; Stach, E. A.; Cyrankowski, E.; Wyrobek, T. J.; Warren, O. L. *Nat Mater* **2006**, *5*, 697.

(32) Gouldstone, A.; Van Vliet, K. J.; Suresh, S. *Nature* **2001**, *411*, 656.

(33) Zaluska, A.; Zaluski, L.; Strom-Olsen, J. O. *Journal of Alloys and Compounds* **1999**, *288*, 217.

(34) Keblinski, P.; Phillpot, S. R.; Choi, S. U. S.; Eastman, J. A. *International Journal of Heat and Mass Transfer* **2002**, *45*, 855.

(35) Shipway, A. N.; Katz, E.; Willner, I. *Chemphyschem* **2000**, *1*, 18.

(36) Ke, Y. C.; Long, C. F.; Qi, Z. N. *Journal of Applied Polymer Science* **1999**, *71*, 1139.

(37) Brust, M.; Kiely, C. J. *Colloids and Surfaces a-Physicochemical and Engineering Aspects* **2002**, *202*, 175.

(38) Schaefer, D. M.; Patil, A.; Andres, R. P.; Reifenberger, R. *Physical Review B* **1995**, *51*, 5322.

(39) Gerberich, W. W.; Mook, W. M.; Perrey, C. R.; Carter, C. B.; Baskes, M. I.; Mukherjee, R.; Gidwani, A.; Heberlein, J.; McMurry, P. H.; Girshick, S. L. *Journal of the Mechanics and Physics of Solids* **2003**, *51*, 979.

(40) Kizuka, T.; Yamada, K.; Deguchi, S.; Naruse, M.; Tanaka, N. *Physical Review B* **1997**, *55*, R7398.

(41) Wall, M. A.; Dahmen, U. *Microscopy Research and Technique* **1998**, *42*, 248.

(42) Minor, A. M.; Morris, J. W.; Stach, E. A. *Applied Physics Letters* **2001**, *79*.

(43) Deneen, J.; Mook, W.; Minor, A.; Gerberich, W.; Barry Carter, C. *Journal of Materials Science* **2006**, *41*, 4477.

(44) Shan, Z. W.; Adesso, G.; Cabot, A.; Sherburne, M. P.; Syed Asif, S. A.; Warren, O. L.; Chrzan, D. C.; Minor, A. M.; Alivisatos, A. P. *Nat Mater* **2008**, *7*, 947.

(45) Lockwood, A. J.; Inkson, B. J. *Journal of Physics D: Applied Physics* **2009**, *42*, 035410.

(46) Levitt, A. P. *Whisker Technology*; Wiley-Interscience: New York, 1970.

(47) Han, X.; Zheng, K.; Zhang, Y.; Zhang, X.; Zhang, Z.; Wang, Z. L. *Advanced Materials* **2007**, *19*, 2112.

(48) Han, X. D.; Zhang, Z.; Wang, Z. L. *Nano* **2007**, *2*, 249.

(49) Iijima, S. *Nature* **1991**, *354*, 56.

(50) Overney, G.; Zhong, W.; Tomanek, D. *Zeitschrift Fur Physik D-Atoms Molecules and Clusters* **1993**, *27*, 93.

(51) Bacon, R. *Journal of Applied Physics* **1960**, *31*, 283.

(52) Calvert, P. *Nature* **1992**, *357*, 365.

(53) Iijima, S.; Ichihashi, T.; Ando, Y. *Nature* **1992**, *356*, 776.

(54) Ruoff, R. S.; Lorents, D. C. *Carbon* **1995**, *33*, 925.

(55) Treacy, M. M. J.; Ebbesen, T. W.; Gibson, J. M. *Nature* **1996**, *381*, 678.

(56) Dresselhaus, M. S.; Dresselhaus, G.; Sugihara, K.; Spain, I. L.; Goldberg, H. A. *Graphite Fibers and Filaments*; Springer: New York, 1988.

(57) Poncharal, P.; Wang, Z. L.; Ugarte, D.; Heer, W. A. d. *Science* **1999**, *283*, 1513.

(58) Chen, C. Q.; Shi, Y.; Zhang, Y. S.; Zhu, J.; Yan, Y. J. *Physical Review Letters* **2006**, *96*, 075505.

(59) Yu, M.-F.; Lourie, O.; Dyer, M. J.; Moloni, K.; Kelly, T. F.; Ruoff, R. S. *Science* **2000**, *287*, 637.

(60) Ruoff, R. S.; Tersoff, J.; Lorents, D. C.; Subramoney, S.; Chan, B. *Nature* **1993**, *364*, 514.

(61) Zhu, Y.; Espinosa, H. D. *Proceedings of the National Academy of Sciences of the United States of America* **2005**, *102*, 14503.

(62) Agrawal, R.; Peng, B.; Espinosa, H. D. *Nano Letters* **2009**, *9*, 4177.

(63) Huang, J. Y.; Chen, S.; Jo, S. H.; Wang, Z.; Han, D. X.; Chen, G.; Dresselhaus, M. S.; Ren, Z. F. *Physical Review Letters* **2005**, *94*, 236802.

(64) Huang, J. Y.; Chen, S.; Wang, Z. Q.; Kempa, K.; Wang, Y. M.; Jo, S. H.; Chen, G.; Dresselhaus, M. S.; Ren, Z. F. *Nature* **2006**, *439*, 281.

(65) Han, X. D.; Zhang, Y. F.; Zheng, K.; Zhang, X. N.; Zhang, Z.; Hao, Y. J.; Guo, X. Y.; Yuan, J.; Wang, Z. L. *Nano Letters* **2007**, *7*, 452.

(66) Zhang, Y.; Han, X.; Zheng, K.; Zhang, Z.; Zhang, X.; Fu, J.; Ji, Y.; Hao, Y.; Guo, X.; Wang, Z. L. *Advanced Functional Materials* **2007**, *17*, 3435.

(67) Zheng, K.; Han, X.; Wang, L.; Zhang, Y.; Yue, Y.; Qin, Y.; Zhang, X.; Zhang, Z. *Nano Letters* **2009**, *9*, 2471.

(68) Li, X. D.; Hao, H. S.; Murphy, C. J.; Caswell, K. K. *Nano Letters* **2003**, *3*, 1495.

(69) Mao, S. X.; Zhao, M.; Wang, Z. L. *Applied Physics Letters* **2003**, *83*, 993.

(70) Feng, G.; Nix, W. D.; Yoon, Y.; Lee, C. J. *Journal of Applied Physics* **2006**, *99*.

(71) Joslin, D. L.; Oliver, W. C. *Journal of Materials Research* **1990**, *5*, 123.

(72) Falvo, M. R.; Clary, G. J.; Taylor, R. M.; Chi, V.; Brooks, F. P.; Washburn, S.; Superfine, R. *Nature* **1997**, *389*, 582.

(73) Wong, E. W.; Sheehan, P. E.; Lieber, C. M. *Science* **1997**, *277*, 1971.

(74) Salvetat, J.-P.; Andrew, G.; Briggs, D.; Bonard, J.-M.; Bacsa, R. R.; Kulik, A. J.; Stockli, T.; Burnham, N. A.; Forro, L. *Physical Review Letters* **1999**, *82*, 944.

(75) Zhou, P.; Wu, C.; Li, X. *Measurement Science and Technology* **2008**, *19*, 115703.

(76) Cuenot, S.; Demoustier-Champagne, S.; Nysten, B. *Physical Review Letters* **2000**, *85*, 1690.

(77) Cuenot, S.; Frétigny, C.; Demoustier-Champagne, S.; Nysten, B. *Physical Review B* **2004**, *69*, 165410.

(78) Song, J.; Wang, X.; Riedo, E.; Wang, Z. L. *NanoLetters* **2005**, *5*, 1954.

(79) Hoffmann, S.; Utke, I.; Moser, B.; Michler, J.; Christiansen, S. H.; Schmidt, V.; Senz, S.; Werner, P.; Gosele, U.; Ballif, C. *NanoLetters* **2006**, *6*, 622.

2. Equipment

2.1. Atomic Force Microscope (AFM)

The Atomic Force Microscope (AFM) and the Scanning Tunneling Microscope (STM) are types of scanning probe microscope. The latter was invented by Binnig and Roher in 1981[1] and earned them a Nobel Prize in 1986. That same year Binnig, Quate and Gerber invented the AFM[2]. Its principle of operation involves scanning of a sharp tip over a surface where the interaction between the probe and the sample is closely monitored by a feedback loop. The raster scanning of the tip allows the construction of an image representing the topography of the surface. Most tip-surface interaction forces are related to Van der Wall's forces or dipole-dipole interactions but by carefully designing the tip it is possible to study a wide range of interactions e.g. magnetic and electrostatic forces and even thermal gradients. The following paragraphs provide a generalised overview of scanners and probes as well as the overall principle and operating modes of AFM.

2.1.1 Working principle

The motion of the AFM tip during raster scanning of the surface is detected by a laser beam, of usually 1 mW, which strikes the cantilever and is reflected onto the photodetector, as seen on Figure 19. The latter is made up of 4 quadrants which combine to form the total signal and to provide different information depending on the type of operating mode. From the position of the laser reflection on the photodetector, the lateral and normal deflections of the cantilever are measured. For instance, the differential signal between the top 2 and the bottom 2 elements is a measure of the normal deflection of the cantilever.

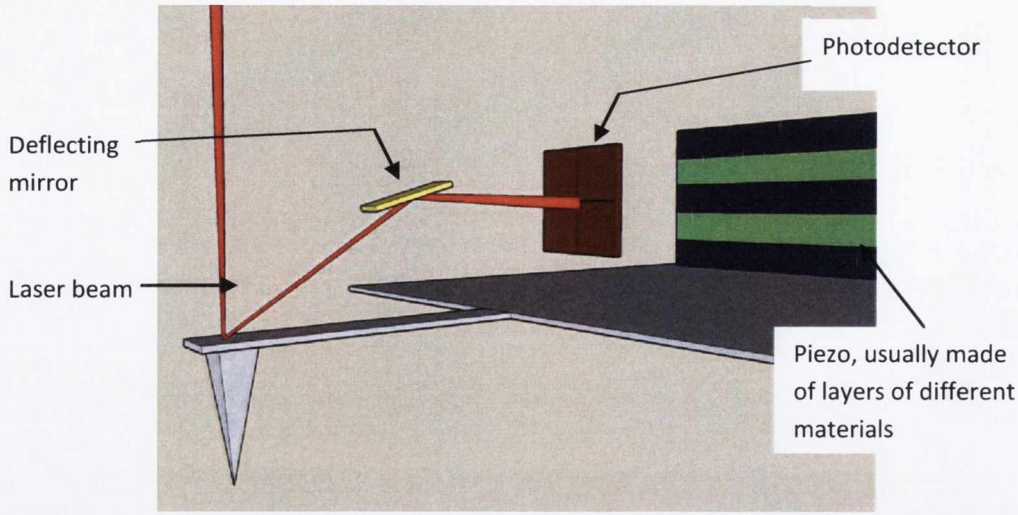


Figure 19. *Principle of AFM*

AFM operates in two different modes: Contact and Tapping (or dynamic) mode. The former utilises a feedback on the cantilever deflection whereas the latter monitors the cantilever amplitude or frequency. These changes are observed through a four quadrant split photodiode detector that can detect changes in cantilever deflection of less than 1 Å. The feedback loop maintains deflection and amplitude according to a predefined set-point. The feedback is monitored by a PID controller (proportional-integral-derivative) which minimises the error between the measured signal and the desired setpoint. By using the so called Contact Mode, the operator maintains a constant force between the surface and the tip. This force, F, is calculated from Hooke's Law, $F = -kx$, where k is the spring constant of the cantilever and x the cantilever deflection. The height is then recorded at each point and forms a topographic image of the surface. In Tapping Mode, the tip is oscillated at constant amplitude (usually in the range of 20 to 100 nm) and hence gently taps over the surface, building up a point by point topographic image of the surface. The feedback loop maintains constant oscillation amplitude by monitoring the root mean square of the signal acquired by the photodiode. The oscillation amplitude is constant and predefined as the 'set-point amplitude'; hence a constant tip-sample interaction is maintained during imaging.

The following table lists the main advantages and disadvantages for both imaging modes.

Table 2. *Advantages and disadvantages of Contact Mode and Tapping Mode AFM*

	Contact Mode	**Tapping Mode**
Advantages	• High scan speeds • Atomic resolution	• Higher lateral resolution • Lower forces and less damage to soft samples
Disadvantages	• Distortion of the image by shear forces • Damages on the surface due to scraping	• Slower scan speed

Scanners

To position and move the AFM probe across the surface it is necessary to have some mean to scan the probe. AFM scanners are made from piezoelectric materials that allow extreme precision in scanning. However, the relationship of movement vs. applied voltage is nonlinear and hence creates hysteresis between the trace and re-trace scans. It is necessary to calibrate the scanner to account for this effect and eliminate it. Scanners are either driving the tip or driving the stage. The latter allows decoupling of the XY-Z piezo, hence reducing noise in the system. Closed loop scanners are even more precise than open loop ones as they allow extreme positioning of the tip (within a few nanometres), which is extremely important for patterning and manipulation experiments. However, close-loop operation induces quite some noise in the imaging, which makes it inconvenient for all other experiments.

Probes

Two main types of probes are available commercially: silicon nitride and silicon. The former are triangle-shaped, exhibiting low spring constant (down to 0.01 N/m) and are used for Contact Mode or Tapping Mode in liquid. Silicon probes are rectangle-shaped, exhibit spring constant up to 50N/m and are mostly for Tapping Mode in air. Both are available with numerous coatings allowing measurements of a wide range of forces (magnetic, electric, chemical, etc...). Figure 20 shows a micrograph of a Si AFM probe and the inset is a zoom-in of the tip itself. The resonance frequency of the cantilever depends of its dimensions, with longer tips exhibiting smaller resonance frequencies. The apex of the tip is usually around 20 nm but deteriorates quickly as the tip scans the

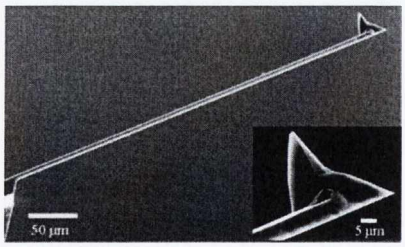


Figure 20. *SEM micrograph of a Si AFM probe*

surface. The lateral resolution of the AFM is not nearly as high as its vertical resolution which can be up to 0.1 nm. This is due to lateral interaction of the tip with the surface. To eliminate this effect extremely high aspect ratio tips can be purchased. An important characteristic of both is the spring constant k. For triangular cantilevers, the spring constant is usually calculated by a thermal noise method[3-4]. For rectangle-shaped cantilever k is calculated using the following equation, with E being the Young's modulus: $k = \frac{Et^3 w}{4L^3}$. Nevertheless, numerous other methods have been reported[5-10]. For our study, we use a different method which is detailed in section 2.2.1.

AFM is a very versatile tool allowing high resolution imaging on a wide range of surfaces and media. By carefully choosing the tip and its coating, one can probe specific physical properties. In Tapping Mode, the resonance frequency is modified by tip-surface interaction forces and shifts in this frequency provide information about the sample. This operating mode is called frequency modulation AFM (FM-AFM). A similar technique, amplitude modulation AFM (AM-AFM) provides information on the phase of the oscillation which in turn can distinguish materials on the surface. Other main advantages of AFM are its patterning and manipulation abilities. The latter was used extensively for our work on the study of mechanical properties of nanowires, which we will detail in the next section.

2.1.2. Mechanical measurements

As mentioned in the first part of this report, several techniques have been reported to measure the mechanical properties of nanowires. The method we present here overcomes the main disadvantages of the previous techniques by removing the wire-substrate friction while accurately measuring the nanowire diameter and the elastic properties. In order to measure a wide range of mechanical properties such as Young's Modulus, yield strength, plastic deformation and failure, a novel method using Focussed Ion Beam (FIB), Electron Beam Induced Deposition (EBID), Scanning Electron Microscope (SEM) and Atomic Force Microscope (AFM) has been developed[11-12]in our lab. It involves

pushing a double-clamped nanowire suspended across a trench with an AFM tip, while recording the force needed to push and/or break the wire using a Lab View program.

Trenches have to be fabricated. Gold is evaporated onto a silicon substrate to a thickness of 50 nm. The sample was then placed into the Dual Beam chamber and the latter was pumped down. Electron and ion beams were aligned and focused on a clean, smooth area of the substrate. The trench width needed depends on the diameter of the nanowires, as the theory we use requires a ratio of at least 10 between the spanning length of the wire and its diameter. A range of widths was fabricated on different substrates, from 500 nm to 5 μm. The length of the trenches is only limited by the time needed to mill them knowing we want the trenches to be as long as possible to make their detection on the surface easier. A length of 200 μm was chosen. For better manipulation, depth of at least 500 nm is required. However, we only need to mill through the Au layer, hence creating a pattern of trenches, later to be etched into the

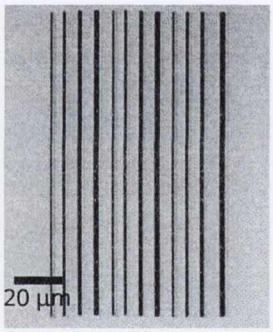


Figure 21. *SEM image of a set of milled trenches of different widths*

silicon. Figure 21 shows a set of trenches milled following this procedure. It is to be noted that a clear difference in contrast is observed between the trenches and the surface. This is evidence that the milling went through the gold and reached SiO_2, which is insulating hence comes up darker than the gold surface. Each trench was separated from the next one by at least 2 μm. Once the milling is complete, the sample was taken from the chamber and put into a few millilitres of hydrofluoric acid (HF) buffer (25%, supplied by Trancene) for 4 to 5 minutes, as the etching rate of the buffer solution is 100 nm/min. As etching is isotropic, leaving the substrate in HF for too long would lead to large undercut, jeopardising the strength of the trenches. Afterwards, the substrate was thoroughly cleaned in de-ionised water and dried with nitrogen. Because HF etches deep into the trench but also wide on the edge of the trench (isotropic etching), the gold layer at the edge of the trench peels off and rolls up, as shown in Figure 22.

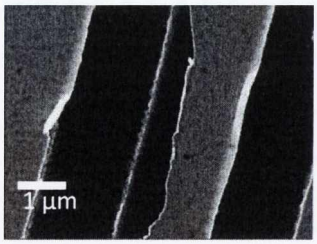


Figure 22. *SEM micrograph of Au peeling out after HF treatment*

The one-dimensional nano-material to be studied was then dispersed on the substrate. In the case of germanium nanowires, a dispersion was made up prior to deposition. It usually consists of a few mg of nanowires powder dispersed in about 2 mL of isopropanol and sonicated for 5 minutes, until the solution becomes darker, a sign of a quite homogenous dispersion. Between 3 and 5 µL were taken from this solution and dropped on the substrate. In order to get a better alignment of the wires, i.e. perpendicular to the trenches, N_2 was gently blown on the substrate to dry out the solvent. A large proportion of nanowires followed the direction of the N_2 flow and were somewhat aligned. After each drop casting of the nanowire solution, the substrate was inspected under the optical microscope to check that a sufficient amount of nanowires were spanning across trenches.

The sample was placed into the Dual Beam chamber, securely attached to the chuck with conductive copper tape. As platinum (Pt) is going to be deposited at this point via electron beam induced deposition (EBID), a good vacuum is needed to ensure the best quality. Imaging was usually commenced once the chamber pressure reached at least $5x10^{-6}$ mbar, which took 10 minutes. The sample was then positioned to have the trenches in a north – south direction. It has been empirically observed that the Pt deposition is more reproducible and of better quality when deposited in this direction. Pt lines of 2 µm long, 200 nm wide and 200 nm high were deposited. These have to be positioned on the edge of the trench, so as to eliminate the wire-substrate friction. To ensure mechanical stability between the wire and the Pt line, a Pt thickness at least twice the height of the nanowire has to be deposited. Figure 23 shows a germanium nanowire spanning over a trench and pinned down on both sides by Pt lines. On a same set of nanowires, an average amount of 20 to 25 wires were pinned down.

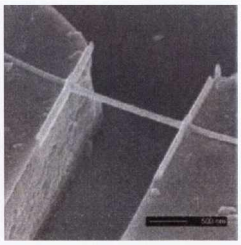


Figure 23. *SEM micrograph of a Ge nanowire pinned of both sides by EBID Pt*

The sample is then positioned on the Veeco Dimension 3100 AFM stage, secured by a vacuum chuck, in such a way that the wire of interest is parallel to the cantilever. Because the height of the tip relative to the surface is of paramount importance for our purposes, a ramp plot in Tapping Mode was performed to map out the distance of the tip from the surface. Figure 24 is a typical plot of amplitude against height for a 300 kHz

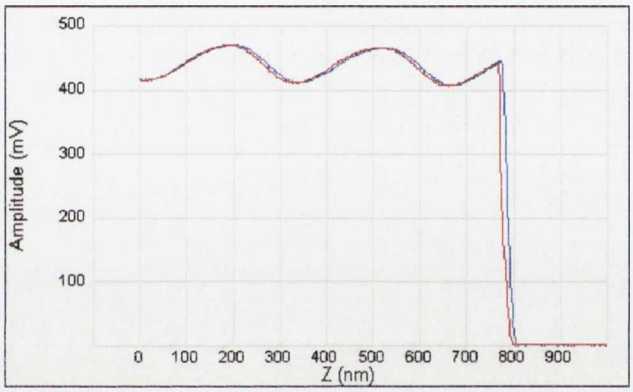


Figure 24. *Plot of Amplitude vs Height for a 300kHz tip*

tip. The sinusoidal part of the graph represents the free amplitude oscillation of the tip above the surface. The sharp slope between 0 and 430 mV is the range of setpoints available, 0 mV being when the tip is in constant contact with the surface. The absolute height on the graph is irrelevant, only the relative distance from the height corresponding to 0 mV matters (here 800 nm). The setpoint chosen for imaging allows us to know the distance of the tip from the surface. For example, for a setpoint of 300 mV, the corresponding height is around 780 nm, which means the average position of the tip is at 20 nm (800 -780 nm) from the surface.

An image of the nanowire was acquired. Accuracy of the manipulation was ensured by taking a close-up image of the wire, where the suspended part represented 80% of the image. It is preferable to image the nanowire at 90° angle to get the best resolution for the diameter of the wire. We used the Nanoman software package built into the Veeco software to manipulate the wires. In this application, after taking a single scan of the area the tip is positioned at the centre of the image, hovering over the surface. The

Nanoman path program is made up of 2 parts: *connect* and *segment*. The former displays the parameters for the tip to go from its hovering position to the beginning of the path, or between paths. It was set as Tapping Mode in our case. The latter sets parameters of the path itself, such as Tapping or Contact mode, feedback, xy velocity, z position, etc... We set the segment parameters as Contact mode, feedback off and xy velocity of 0.02 μm/s. Before mechanically loading the wire, a line was drawn in the trench, first at z=0, to acquire the baseline and checking if the tip was touching the bottom of the trench. The same procedure was repeated, lowering z each time until the tip touched the bottom of the trench. The height was then set to 20 nm higher than this point. The path was drawn to either carry out a sequence of loading-unloading cycles of the wire or pass through and break the wires in a single shot experiment. Figure 25

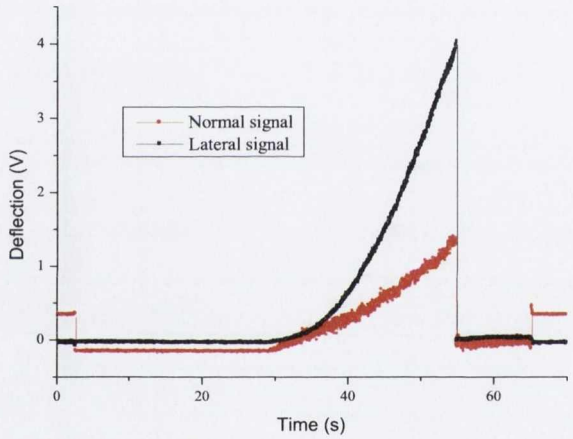


Figure 25. *Typical plot of deflections against time for a Ge NW*

shows a typical plot recorded by the Lab VIEW program. The black line represents the lateral signal and the red one the normal signal. The first part of the plot, from 0 to 30 s represents the baseline, where the tip moves along but above the trench floor. The absence of a slope on the normal signal proves that the tip is not touching the bottom of the trench. At 30 s, the tip makes contact with the wire and loads it laterally. The normal signal is about half of the lateral one, which is quite high but is due to the higher sensitivity of the tip in the normal deflection (around 1000 times) which will be taken into account during calibration. If the normal signal is higher than the lateral one, slippage of the wire on the tip might have occurred. The sharp drop at around 55 s is the sign of the wire breaking with the tip snapping back to its equilibrium position. Once the manipulation is over, a scan in Tapping Mode is taken, as shown in Figure 26. A clear

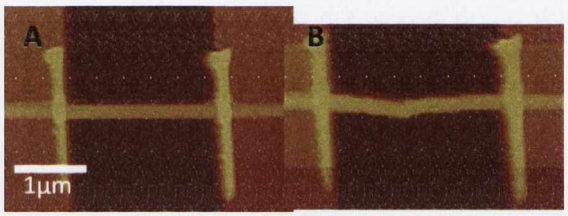


***Figure 26**. AFM images of germanium nanowire before (A) and after (B) break*

break is visible at the centre of the wire and no disruption on the Pt lines can be seen. For each set of wires, around 10 were manipulated with the same tip. The quality of the tip deteriorated after several manipulations and scans. Once all the pinned wires have been loaded, the tip was calibrated to determine its vertical and lateral sensitivities.

Calibration followed the procedure and calculations described by Schwarz et al[13]. The tip was laterally loaded and unloaded against the edge of a calibration grid, at least 3 times

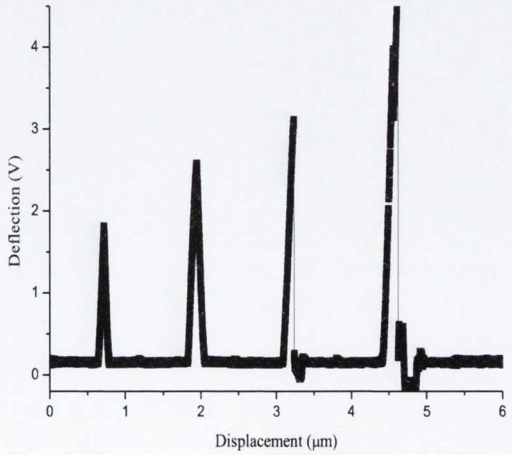


***Figure 27.** Typical plot of deflection against displacement for several consecutive lateral loadings of the tip against the edge of a pit*

as shown on Figure 27. It is important that the calibration was carried out at the same height and setpoint as the manipulation. The slope resulting from this loading, named S_{lat}, represents the tip's maximal lateral deflection per length, expressed in V/m. The AFM is then set in contact mode, with a setpoint of -2 V and a ramp is carried out on the surface. In this process, once the tip is in contact with the surface, it is set to scan a very small area (0.1 nm^2), which means it is basically motionless on the xy plane. Then the tip is set to move vertically (in z direction) following a ramp of 1 µm and when in contact

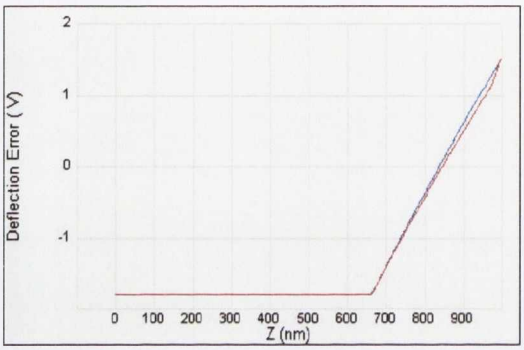


Figure 28. *Typical plot of vertical deflection against z displacement for a 300 kHz tip*

with the surface will apply force. Figure 28 shows a typical plot of vertical deflection against z displacement. The line between 0 and 680 nm represents the free deflection of the tip when it is not touching the surface. Contact with the surface occurred from 680 nm onwards. This slope is named S_{ver} and is expressed in our calculations in m/V, inverse of the graph's slope. The tip was then taken from the tip holder and brought to the SEM for dimensions measurements. Width (*w*), thickness (*t*) and length (*L*) of the cantilever, from the tip to the edge of the cantilever as well as length of the tip itself (l_{tip}) have to be recorded. Figure 29 shows an example of the dimensions of a 300 kHz tip. The red lines represent the dimensions used for the calibration (clockwise from top left hand side: L, l_{tip}, w, t). Typical values of S_{lat}, S_{ver}, w, t, L and l_{tip} for 300 and 75 kHz tips are detailed in Table 3.

Table 3. *Typical calibration values for 300 and 75 kHz tips*

	w (µm)	*t(µm)*	*L(µm)*	*ltip (µm)*	S_{lat} *(V/m)*	S_{ver}(m/V)
300 kHz	41	4.2	120	13.5	20	$5\ 10^{-8}$
75 kHz	32	3.5	240	13	50	$2\ 10^{-7}$

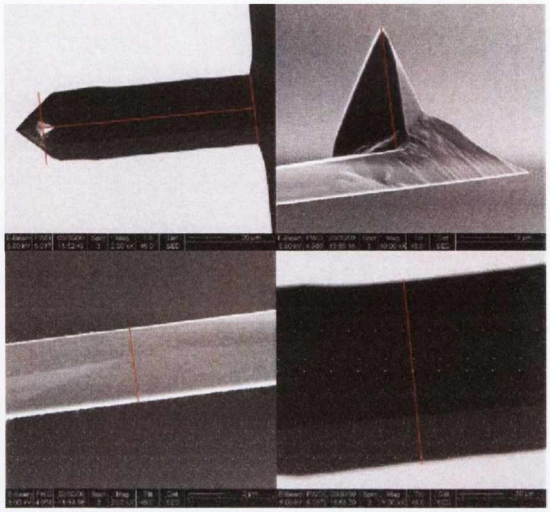


Figure 29. *SEM micrographs of a 300 kHz tip to evaluate its dimensions A) length, B) tip length, C) width, D) thickness.*

The following equation between the force *F* exerted by the tip and the relative change in signal on the photodiode ΔU_{lat} (in volt) is well known[13], where G is the shear modulus of the cantilever (150 GPa in our case):

$$F = \frac{Gwt^3}{4L^2 l_{tip}} . S_{ver} . \Delta U_{lat}$$

The cantilever spring constant, k_c, is also calculated using the calibration parameters: $k_c = S_{lat} \frac{F}{\Delta U_{lat}}$. We have used this technique extensively throughout the work described in this thesis and will present the results obtained for germanium nanowires and polymer composite nanofibres.

2.2. Scanning Electron Microscope (SEM) and Focussed Ion Beam (FIB)

Our work was mostly conducted on a FEI Strata Dual Beam SEM FIB. It is composed of two columns: a vertical electron column and an ion column situated at 52° from the former. The chamber also contains several detectors (secondary electron detector (SED), triple lens detector (TLD) for back-scattered electrons) and three gas injections systems (GIS) that allow the deposition of Pt and SiO_2 as well as enhanced etching with XeF_2. We will explain the main components of the system and detail their working principles. A minor part of the work was conducted on the Carl Zeiss Auriga Cross Beam tool whose concept is very similar to the FEI tool.

SEM

In 1925 Louie de Broglie theorised that the electron had wave-like characteristics[14] and 1927 it was demonstrated by electron diffraction experiments[15]. Only a few years later (1932) the first electron microscope was reported[16]. A SEM generates a beam of electrons that are scanned in a raster scan pattern in a vacuum. The beam is collimated through electromagnetic condenser lenses, focuses via objective lenses and scanned across the surface using electromagnetic deflection coils. A schematic of the main features of the column is pictured on Figure 30.

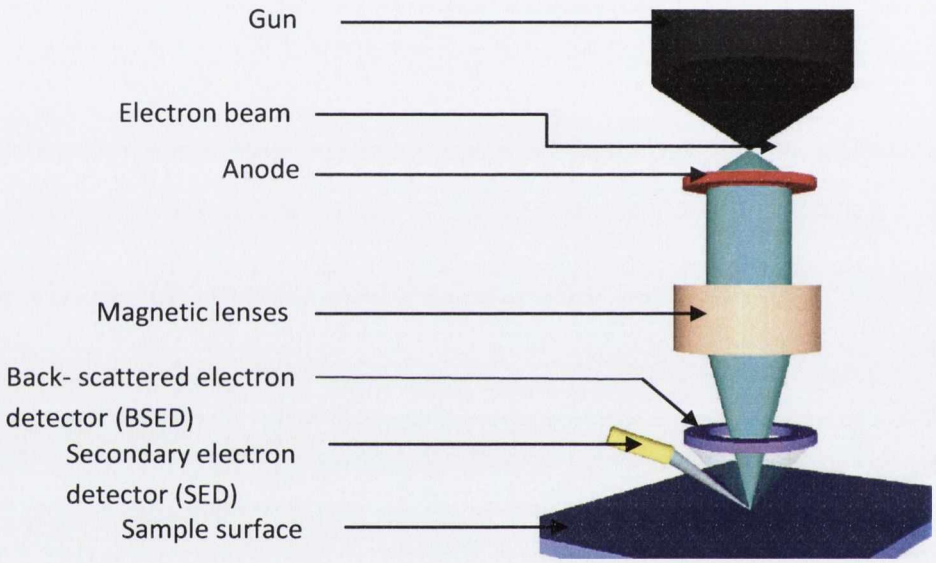


Figure 30. *Schematics of SEM column*

There are 3 types of gun available: tungsten filament cathode, lanthanum hexaboride cathode (LaB_6) and field emission gun (FEG), each of them requiring increasing vacuum levels and providing increasing resolution. The first two types function in a very similar way. A current is passed through the cathode to generate thermionic emission of electrons. These electrons are then attracted by the anode situated below the filament to generate the beam. The vacuum level needed for a tungsten filament and LaB_6 are respectively around 10^{-5} mbar and 10^{-6} mbar. A LaB_6 cathode is generally an order of magnitude brighter than a tungsten filament and also provides longer cathode life. A FEG functions in a complete different way but provides by far the highest resolution. The principle of the FEG is based on tunneling. The gun is made up of a very sharp tungsten

tip onto which a high negative voltage is applied in relation to a nearby electrode. The high field collapses the normal workfunction barrier to emission and tunnelling becomes possible. As a result electrons are emitted from the metal, hence creating a beam down the column. The vacuum needed in a FEG column is around 10^{-7} mbar and the resolution obtained is of the order of a nanometre.

If we apply the classic Rayleigh criterion for the resolution of a light microscope, we find that the smallest distance that can be resolved is approximately half of the wavelength of the radiation. In addition, by referring to Louie de Broglie's equation linking wavelength of electrons, λ, and their energy, E, we expect the following relationship: $\lambda = 1.22/E^{1/2}$ with λ in nm and E in eV. Most SEMs function between 0.5 and 30 kV. The higher voltages theoretically provide sub-nanometric resolution (0.2 nm). However imperfections in electron lenses make this limit almost unachievable. Nevertheless state-of-the-art microscopes can routinely achieve nanometric resolution.

When the incident electron beam reaches the surface, several electron-solid interactions take place below the surface forming a pear-shaped excitation volume, as shown on Figure 31. From within this excitation volume electrons and x-rays emerge and can be used to gain valuable information. The penetration depth (D) depends on the electron energy (V) and on the material (D ~ V and D ~ 1/atomic mass). At low energy (around 50 eV and less) secondary electrons stemming from inelastic scattering are generated just a few nanometres below the surface. These electrons are commonly used for topographic imaging.

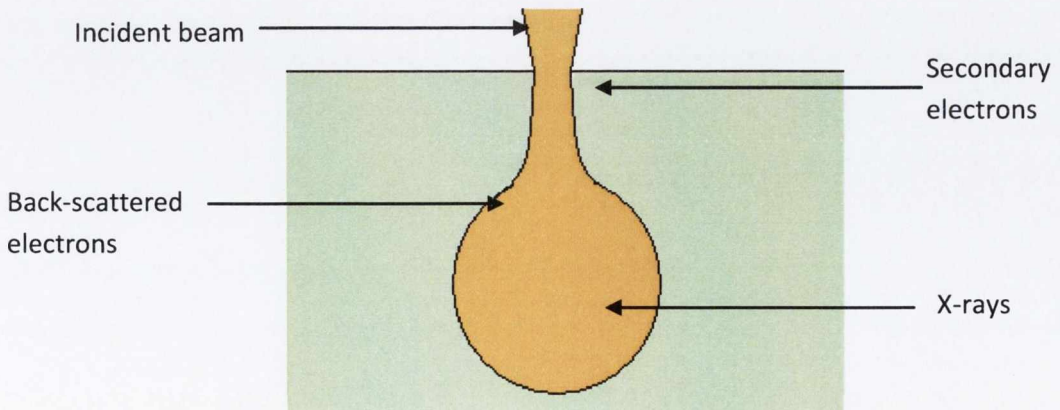


Figure 31. *Schematics of interaction volume upon incident electron beam*

At higher energy elastically back-scattered electrons emerge from the sample. Because of the way the electrons interact with the solid, these electrons are highly dependent on the atomic number with heavy atoms giving higher signal that lighter ones. Hence backscattered electrons provide compositional information. At the higher end of the energy spectrum are X-rays (with energies of the order of keV). These are found at the deeper portion of the interaction volume and an X-ray detector can be added inside the column, providing qualitative elemental analysis.

The most used detector is the SED, giving high quality topographical information. Since incident beam voltages range from 0.5 kV to 30 kV, the lower energy electrons are not energetic enough to reach atoms below the surface; they will provide surface information only. However due to their loss of energy from scattering, some electrons might not reach the detector and the signal would be quite low. A good comprise (for most common samples) for high resolution and low signal to noise ratio is 5 kV.

Before reaching the sample the beam goes through an aperture strip, basically a series of holes of different diameters. Most common apertures range from 30 μm to 100 μm. The smaller ones leaving a lower number of electrons go through provides the highest resolution. The largest one is commonly used for faster material deposition. In SEM there is always a compromise between signal (number of electrons) and noise.

FIB

The FIB works in a very similar way as the SEM although Gallium (Ga) atoms are accelerated instead of electrons. Gallium ions are chosen as the liquid metal ion source because of its low melting point (29.8˚C), its low volatility which conserves the supply of metal, its low surface free energy which ensures viscous behaviour on the substrate and its excellent mechanical, electrical and vacuum properties. Because of their much higher mass, gallium ions mill the surface during scanning. Imaging and milling currents can be chosen from 1 pA to 20 nA by rotating the ion column aperture strip. At low current (less than 50 pA) the FIB can be used to image samples. Currents higher than 300 pA should only be used for milling. A common problem in FIB resides in material re-deposition during milling. This can be tackled by using lower currents. In FIB the compromise lies between current and time. We used the FIB in our experiments to mill trenches into silicon as described in section 2.1.2.

GIS

Inside the chamber, a Gas Insertion System is present. Several needles are located around the stage holder and can supply different gases for deposition purposes. Our main interest lies in platinum, which we will use as an example to explain the working mechanism of electron or ion beam induced deposition (EBID or IBID). The principle lies in the breaking up of a precursor gas by electron or ion beam. A source of methylcyclopentadienyl-trimethyl-platinum is heated to its boiling point and the needle is inserted into the chamber at a very close distance from the substrate (100 μm). The focussed beam scans the pre-patterned feature causing the covalent bonds to break up, resulting in a deposition of Pt metal on the surface. It has to be noted that this deposition is quite dirty as a lot of carbon is deposited simultaneously with Pt.

2.3. Transmission Electron Microscopy (TEM)

Once the first electron microscope was invented by Ruska in the early 1930's a large amount of research was carried out to improve its resolution and design. As was mentioned earlier, on a SEM an image is formed by collecting secondary and back-scattered electrons. In a TEM only transmitted electrons are detected which is only possible for thin samples. Therefore the first breakthrough in TEM came after the development of techniques to thin metal foils to electron transparency and the development of the theory of electron diffraction contrast[17]. In a TEM, electrons are accelerated from the source through the specimen and are converged by a series of lenses onto a detector (or a screen) at the bottom of the column. The thickness of the sample is therefore paramount to the quality of the imaging. The requirement to get enough electrons to be transmitted through the sample is a function of electron energy and average atomic number of the specimen. Higher kV beams allow thicker samples but produce more beam damage. Samples as thin as 100 nm or less are required for high resolution transmission electron microscopy (HRTEM). To achieve such small dimensions, samples can be prepared by forming a thin slice from the bulk sample or by cross sectioning the feature of interest from the surface. The former uses a dimpling machine and grinding tool for coarse thinning where the final thinning of the specimen is carried out either by electro-polishing (only for conductive samples) or by ion milling. The latter technique will be explained in Appendix A.

To ensure enough electrons go through the specimen, TEMs operate at high voltages, typically from 80 kV to 3 MV. However imaging samples at such high voltages create a significant amount of beam damage on the specimen. For this reason, most TEM are used between 200 and 400 kV resulting in the best resolution for the least beam damage. TEMs operate in the high vacuum range with a typical pressure in the column of about 10^{-7} Torr. The electron source usually has much higher vacuum and a field emission gun TEM operates at 10^{-11} Torr.

There are two main operating modes of TEM: imaging and diffraction, described on Figure 32[18]. The objective lens is the first lens on the beam path after the specimen. It forms a diffraction pattern (DP) in the back focal plane and recombines the electrons into an image on the image plane. Depending on the adjustment of the intermediate lens, either a diffraction pattern or an image is projected on the screen. The former occurs when the back focal plane of the objective lens acts as the object plane for the intermediate lens. The latter occurs when the object plane of the intermediate lens is the image plane of the objective lens. The insertion of a selected area diffraction (SAD) aperture allows the operator to select a specific area of the specimen to contribute to the DP, avoiding over-illumination and providing less diffuse spots. A selected area diffraction pattern (SADP) always contains a bright central spot (direct beam electrons) and some scattered electrons arranged in a specific way depending on the nature of the specimen. To obtain a bright-field image, the objective aperture has to be inserted to select only the bright central spot. If the unscattered electrons are excluded, the image obtained is a dark-field image. Electrons scattered out to higher angles (>3°) are detected by a High-Angle Annular Dark Field (HAADF) detector.

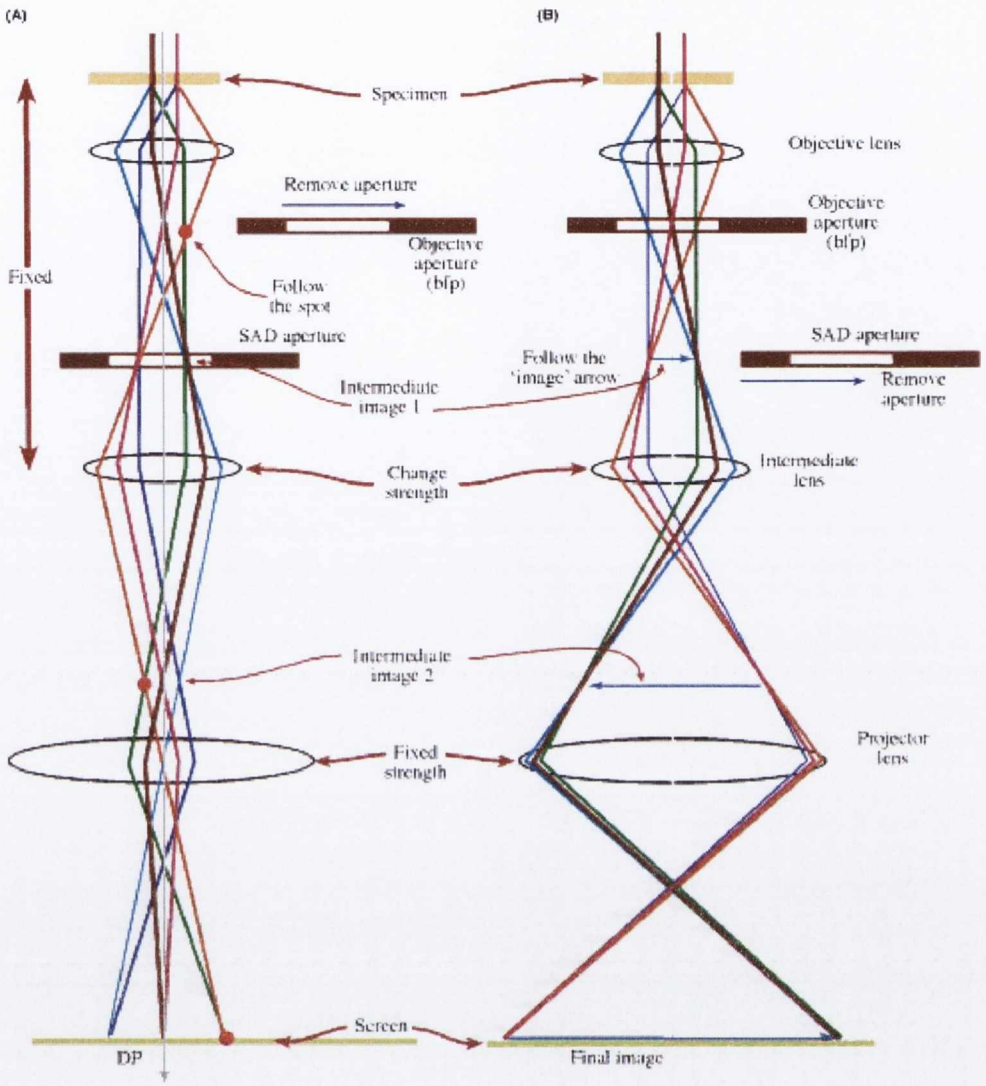


Figure 32. *The two main operating modes of TEM: (A) diffraction mode, (B) imaging mode*

The principle advantage of TEM over other electron microscopy method is its resolution. By applying the Rayleigh criteria described for the SEM on page 44 at 100 keV, the wavelength is 4 pm, hence a resolution of 2pm is theoretically possible. Unfortunately this is not the case because of imperfect electron lenses. However, the resolution of TEM has been dramatically improved in the last few years mainly due to breakthrough in spherical and chromatic aberration corrections. Therefore the improvement of electron lenses and the use of higher voltages led to the development of HRTEM, allowing the visualisation of columns of atoms in crystals.

Electron scattering is of paramount importance in TEM as elastically scattered electrons are the main source of contrast in TEM images. Scattering can be grouped in two

categories: elastic (no loss of energy) and inelastic (some energy loss). Coherence is also an important factor. Elastically scattered electrons are usually coherent if they are only deviated a few degrees from the incident beam and incoherent for higher angles (>10°); inelastic electrons are always incoherent. Scattering increases with specimen thickness and atomic number while it decreases with increasing voltages. For thin samples, single scattering events are most common as the mean free path of an electron accelerated at TEM voltages in of the order of tens of nm. Interestingly, the electrons are in phase in the incident beam but scattering results in a loss of phase coherence between scattered and direct beams.

To achieve best imaging in TEM and HRTEM, understanding diffraction is essential. Crystalline samples will produce an ordered array of dots when looked at in diffraction mode. This array of dots can help find the best orientation of the sample to achieve the highest quality imaging. From the diffraction pattern, we can also learn about symmetry, lattice parameters and crystallographic faults of the sample.

Conclusion

Scanning probe microscopy and electron microscopy are the cornerstone of nanotechnology. They are extremely versatile tools which can facilitate the investigation of a wide range of materials properties. In addition SEM coupled with electron beam lithography and/or FIB allow the fabrication of substrates for the integration of nanostructured materials into devices. We have demonstrated the importance of using several of these tools in conjunction to investigate the mechanical properties of nanowires. Indeed by first using FIB to mill trenches, then SEM to locate and pin the NWs with EBID Pt, then TEM to study the NWs structure and finally AFM to manipulate these NWs, we have developed a generalised technique to study the mechanical properties of nanowires.

References

(1) Binnig, G.; Roher, H. *IBM Journal of Research and Development* **1986**, *30*, 355.

(2) Binnig, G.; Quate, C. F.; Gerber, C. *Physical Review Letters* **1986**, *56*, 930.

(3) Gibson, C. T.; Weeks, B. L.; Lee, J. R. I.; Abell, C.; Rayment, T. *Review of Scientific Instruments* **2001**, *72*, 2340.

(4) Christopher, T. G.; Daniel, J. J.; Christopher, A.; Chris, A.; Trevor, R. *Review of Scientific Instruments* **2004**, *75*, 565.

(5) Torii, A.; Sasaki, M.; Hane, K.; Okuma, S. *Review of Scientific Instruments* **1996**, *7*, 179.

(6) Sader, J. E.; Chon, J. W. M.; Mulvaney, P. *Review of Scientific Instruments* **1999**, *70*, 3967.

(7) Langlois, E. D.; Shaw, G. A.; Kramar, J. A.; Pratt, J. R.; Hurley, D. C. *Review of Scientific Instruments* **2007**, *78*, 093705.

(8) Pettersson, T.; Nordgren, N.; Rutland, M. W.; Feiler, A. *Review of Scientific Instruments* **2007**, *78*, 093702.

(9) Gates, R. S.; Reitsma, M. G. *Review of Scientific Instruments* **2007**, *78*, 086101.

(10) Golovko, D. S.; Haschke, T.; Wiechert, W.; Bonaccurso, E. *Review of Scientific Instruments* **2007**, *78*, 043705.

(11) Wu, B.; Heidelberg, A.; Boland, J. J. *Nature Materials* **2005**, *4*, 525.

(12) Wu, B.; Heidelberg, A.; Boland, J. J.; Sader, J. E.; Sun, X.; Li, Y. *NanoLetters* **2006**, *6*, 468.

(13) Schwarz, U. D.; Koster, P.; Wiesendanger, R. *Review of Scientific Instruments* **1996**, *67*, 2560.

(14) de Broglie, L. *Annales de Physiques* **1925**, *3*.

(15) Davisson, C. J.; Germer, L. H. *Physical review* **1927**, *30*, 705.

(16) Knoll, M.; Ruska, E. *Z. Phys.* **1932**, *78*, 318.

(17) Hirsch, P.; Howie, A.; Nicholson, R.; DW, P.; Whelan, M. *Electron microscopy of thin film crystals* New York, 1977.

(18) Williams, D. B.; Carter, C. B. *Transmission Electron Microscopy - A textbook for materials science* New York, 1996; Vol. 1.

3. Mechanical properties of germanium nanowires with diameters above 40nm

3.1 Motivation

Semiconductor nanowires are important 'building blocks' for circuits, electromechanical devices and others. In the drive to implement them into devices, their electronic properties have been extensively studied. However, mechanical behaviour has received much less attention particularly due to the difficulty in handling these materials which makes manipulation and especially mechanical measurements a considerable challenge. Semiconductor nanowires are important 'building blocks' for electromechanical devices. We have reviewed in the first chapter the different techniques available to measure the mechanical properties of nanowires. While our main interest lies in germanium nanowires, we will discuss silicon as well. Silicon and germanium are quite similar; both are metalloids belonging to group 14 with germanium just below silicon in the periodic table. Both crystals are face-centered cubic with silicon lattice parameter being 5.43 Å and germanium's 5.64 Å. Silicon nanowires have been studied to a much larger extent than germanium nanowires, probably because of the importance of bulk silicon in the micro-electronics industry. Germanium was used to build the first transistor back in 1947[1] as it has a higher electron mobility than silicon. However the main advantage of silicon over germanium is its oxide. SiO_2 has been extensively studied and characterised over the years which makes it easy to incorporate into devices. Germanium oxide is of poor quality (mixture of GeO_x) with GeO_2 soluble in water. Nevertheless, recent advances in nanotechnology and end-of-the roadmap issues with silicon have resulted in renewed interest in germanium.

In terms of mechanical properties, both silicon and germanium are elastic materials exhibiting brittle failure in their bulk form. Table 4 displays the stiffness and strength of these materials. The range of Young's moduli data is due to the stiffness difference along different crystallographic orientations. Silicon exhibits a slightly larger Young's modulus (around 25%) and strength (around 35%) compared with germanium. It is worth noting that these values were calculated for defect-free materials and therefore represent an upper bound for these parameters.

Table 4. Young's modulus E and ultimate strength σ of bulk silicon and germanium

	E(GPa)	σ (GPa)
Silicon	135-190[2]	22[3]
Germanium	103-150[2]	14[3]

As we have seen in the first chapter there are many techniques to measure the mechanical properties of nanowires. Table 5 summarises the main experimental results and theoretical calculations for Si and Ge NWs.

Table 5. Young's modulus E, ultimate strength σ and bending strength σ_b of Si and Ge nanowires

	Silicon nanowires			**Germanium nanowires**	
	E (GPa)	σ (GPa)	σ_b (GPa)	E (GPa)	σ (GPa)
Experimental techniques	210[4], 158[5], 186[6]	12[7]	0.3-0.85[4], 17.5[7]	112[8], 106[9]	15[8]
Calculations	147.3 (tetrahedral NW)[10], 94.43 (cagelike NW)[10], 165[11], 139[11]	22.7[11], 13.2[11]		160[11], 125[11]	19[11], 11.1[11]

Interestingly there are only small discrepancies between experimental data and simulations for the diameters range studied, i.e. above 40 nm. The data for Ge NWs was reported by us[8] or was reported after the publication of our paper[9]. Therefore we will limit the introductory discussion to previous Si NWs data. A number of references cited in this table were detailed in Chapter 1. We will now explain mainly two approaches, one AFM-based on Si NWs and one inside an electron microscope for Ge NWs.

In 2005, Tabib-Azar et al reported on the mechanical properties of self-welded Si NWs[4] with diameters from 140 to 200 nm. Si NWs were grown between two vertical silicon surfaces following a technique described elsewhere[12]. In this configuration, NWs would

either form bridges or cantilevers. In the latter case an AFM was used to vertically load the NWs and extract their Young's modulus and bending strength. The authors found the Young's modulus to be between 93 and 250 GPa and bending strength from 210 and 830 MPa. The Young's modulus was calculated using the following equation:

$$E = 32mx^2 \frac{(3L - x)}{3\pi d^4}$$

where E is the Young's modulus, m is the slope of the load-displacement curve, x is the distance at which the load is applied on the NW, L is the length of the NW and d its diameter. These values are in accordance with bulk Si although they reflect only the behaviour of three NWs of large diameters.

In 2008 Smith et al reported on germanium nanoelectromechanical resonators[9] of diameters from 50 to 140 nm. These nanowires were pinned at the edge of a copper TEM grid with EBID. By applying an AC voltage between an STM tip placed at the clamped end of the nanowire and a tungsten probe near its free end the NW oscillated at their electromechanical resonance as shown on Figure 33. The frequency response of

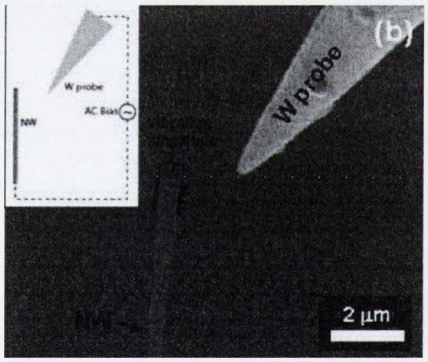


Figure 33. SEM image of a Ge nanowire vibrating due to the AC voltage applied to the tungsten probe[9]

the vibrational amplitude was measured and the Young's modulus was determined. The authors found no diameter dependence for the range studied. In this clamped-free beam configuration, the calculation of Young's modulus was carried out using the following equation derived from the Euler-Bernoulli model[13]:

$$f_1 = \frac{1.875^2}{8\pi} \sqrt{\frac{E}{\rho}} \frac{d}{L^2}$$

where f_1 is the natural resonance frequency, E the Young's modulus, ρ the density of Ge, d the diameter of the wire and L its length. The average Young's modulus was found to be 106 GPa, which is within the range of moduli for Ge. In addition, the authors measured the mechanical quality factor of the nanowires and found it decreased with decreasing diameters. They attributed this phenomenon to surface losses which increase with increasing surface to volume ratio of the nanowires. This result indicates that surface losses may be a limiting factor for nanoscale resonators and electromechanical devices. Surface chemistry and surface structure are essential to the understanding of energy dissipation phenomena at the nanoscale.

3.2 Germanium nanowires synthesis and structure

Germanium nanowires were synthesised by our collaborators in Dr Justin Holmes group in UCC. They used a super-critical-fluid (SCF) method described eslewhere[14]. Gold was sputtered on porous anodic aluminium oxide template and the support was placed inside a chamber with 10 mL of hexane and 0.1 mL of diphenyl germane. The reaction was carried out at 365 °C (ramping 10 °C/min) and 5.5 10^4 mbar for 30 min and formed undoped Ge NWs with diameters ranging from 40 to 160 nm. The NWs are grown from gold droplets. They are expected to have cylindrical shape and to be of the same diameter as their Au catalysts droplets. The NW structure was studied in TEM both on

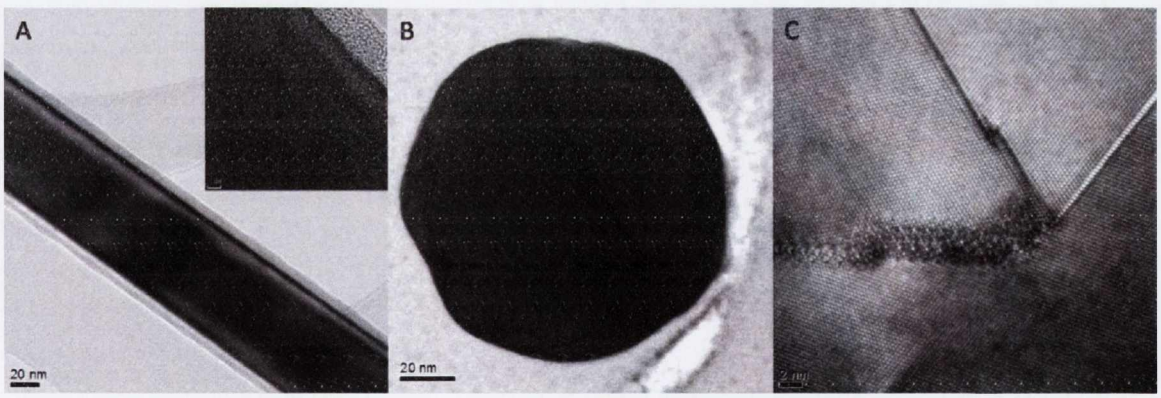


Figure 34. TEM micrographs of Ge NWs (A) plan view, (B) cross section and (C) zoom-in of (B)

plan and cross-section view. The latter sample was prepared following the procedure described in Appendix A. Plan view TEM shows the NWs are single crystal with a preferred growth direction along [110] as seen on Figure 34A. However Figure 34B is a cross-section of an 80 nm NW and Figure 34C clearly shows three crystal grown along the [110] direction and rotated in relation to each other. There are three twinning

planes between crystals of same orientation. Two of these planes are σ_3 and the third is a σ_9 with a much more complex interface. From the statistical sample of images we have taken it seems that a small quantity of wires has defects or stacking faults. Also it is important to note that these NWs have a layer of oxide surrounding them. This oxide layer looks smooth and well defined which makes its removal possible. The NW cross-section from Figure 35B exhibits some faceting instead of being purely disk-shaped.

These NWs were dispersed in isopropanol and sonicated for 30 sec before being dropped cast on a pre-patterned surface. The complete procedure for mechanical measurements is detailed in section 2.1.2. We will now concentrate on the results.

3.3 Mechanical measurements – Results

We found the Ge NWs to be brittle and their force-displacement (F-d) curve to be in excellent agreement with the model developed previously[5] and detailed in Appendix B. Figure 35 is a typical F-d curve for a Ge NW. The black dots represent the data while the red line represents the fit from the generalised model introduced in 2.1.2. At small

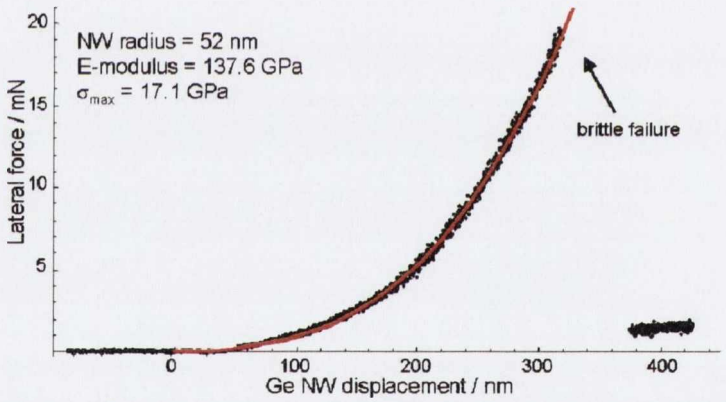


Figure 35. Typical force-displacement curve for a Ge NW

displacements (less than one radius) the F-d curve is linear, consistent with bending of the NW. At larger displacement, F increases more rapidly exhibiting an almost cubic dependence on d. This apparent increase in stiffness is due to tensile stretching of the wire. The model developed previously takes into account both bending and tensile components[5]. Several NWs were tested the same way and their modulus was calculated from the model. This data is displayed on Figure 36 as black dots and the hashed box represents the Young's modulus values for bulk Ge and its different crystal orientations. We found no dependence with diameter for this range and the dash line is the average Young's modulus, 112 GPa ± 43 GPa. It is important to highlight the fact that the oxide layer was not removed from the NWs before testing them. However because this layer is

quite thin (usually 2-4 nm) it does not matter at large diameters, however it will become

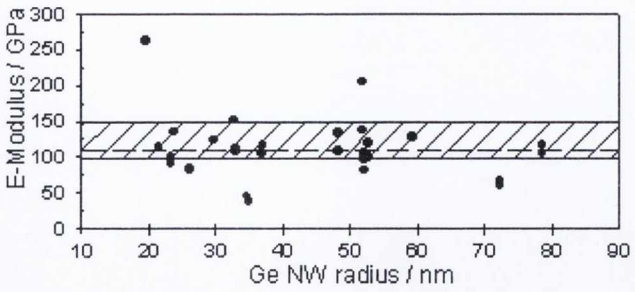


Figure 36. Young's modulus data for all Ge NWs studied

important for smaller wires since the ratio of Ge to Ge oxide is reduced. In any case, since germanium oxide has a much lower modulus than germanium[15] the Young's modulus values reported for small diameters represent a lower bound.

The observed brittleness of the Ge NWs is important on two levels. The absence of plasticity means that the AFM tip interaction on the NW surface does not generate enough compressive stresses to create dislocations and induce plasticity. Hence the failure is uniquely due to crack propagation. The second interesting conclusion we can draw from the brittle fracture is that we can directly extract the ultimate strength of the NWs from the F-d curves. If the failure is only due to bending there is a well-known relationship between the strength σ_0, the force applied F_{centre} and the dimensions of the wire[16]:

$$\sigma_0 = \frac{F_{centre}\, L}{2\pi R^3}$$

where R and L are the radius and length of the double-clamped beam. However this equation does not take into account the tip-NW interaction at the load point. By noting that the maximum stress is located at the surface of the NW at the load point and is identical to the stress at the clamped ends, we can write the following relationship that takes both axial and bending stresses into account:

$$\sigma_{max} = \frac{T}{\pi R^2} + ER \left|\frac{d^2 w}{dx^2}\right|_{x=L/2}$$

where T is the induced tension in the beam, E the Young's modulus, w is the deflection normal to the axis of the beam and x the coordinate along the axis of the beam (at x=L/2, x is the load point). In this relationship, the first term accounts for stretching and

the second for bending. The complete derivation of this equation is in Appendix B and leads to the following generalised equation for the ultimate strength:

$$\sigma_{max} = \frac{F_{centre}\, L}{2\pi R^3} g(\alpha)$$

$$\text{Where } g(\alpha) = \frac{4}{\sqrt{\alpha}} \tanh\left(\frac{\sqrt{\alpha}}{4}\right) + \sqrt{\frac{2+\cosh\left(\frac{\sqrt{\alpha}}{2}\right) - 6\frac{\sinh\left(\frac{\sqrt{\alpha}}{2}\right)}{\sqrt{\alpha}}}{\alpha \cosh^2(\sqrt{\alpha}/4)}}$$

$$\text{and } \alpha = \frac{6\epsilon(140+\epsilon)}{350+3\epsilon} \text{ and } \epsilon = \left(\frac{2\Delta z_{centre}}{R}\right)^2$$

By measuring the dimensions of the wire (L and R), the applied force (F_{centre}) and the resulting displacement at fracture (Δz_{centre}), we can calculate the strength of the wire. Note that knowledge of Young's modulus is not needed for the determination of the strength. We then calculated the strength of the NWs studied, this data is shown on Figure 37. We found an average strength of 15 GPa ± 4 GPa which is the highest recorded strength for any semiconductor material[17]. This value is also in excellent agreement with the predicted theoretical strength for a defect-free material, $\sigma=E/2\pi$[18]. In our case, this strength should be 17 GPa. Our wires exhibit strength only 15 % short of their theoretical strength. This demonstrates that these wires are without defects or flaws that compromise their mechanical properties. We think this behaviour stems from

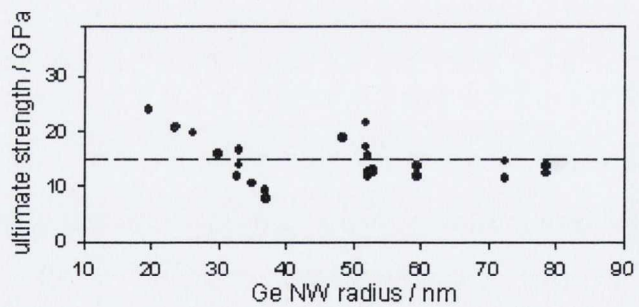


Figure 37. Ultimate strength versus Ge NWs radius

the supercritical growth during which the growth rate is significantly larger than the nucleation rate, driving defects out of the material.

When Δz_{centre} is much smaller than the radius of the beam, ε tends towards 0, so does α, which causes $g(\alpha)$ to tend towards 1. In this limiting case we found σ_{max} from the classic beam theory where fracture is induced by bending only. Interestingly a plot $g(\alpha)$ as a function of $\Delta z_{max}/R$, as shown on Figure 38, is equivalent to plotting how similar σ_0 and

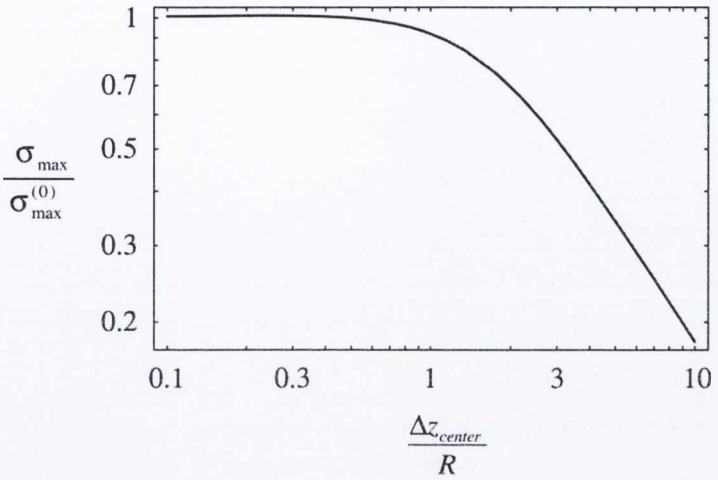


Figure 38. Plot of σ_{max}/σ_0 as a function of $\Delta z_{max}/R$

σ_{max} are as a function of displacement since $\sigma_{max} = \sigma_0\ g(\alpha)$. For small displacements, we find the bending condition discussed previously. When Δz_{max} is less than one radius, σ_0 and σ_{max} are similar, which means $g(\alpha)$ is equal to 1. As displacements increase so does the difference between σ_0 and σ_{max}. The Ge NWs studied here typically exhibit displacements of the order of 3 radii. In this case, if we had calculated their strength using σ_0 it would have been over-estimated by at least 50 %. Neglecting tensile stress in the analysis of the F-d curves can lead to significant deviation from the true strength.

An important quality of a material is its ability to elastically deform before failure. Figure 39 is a plot of the displacement at failure as a function of the aspect ratio of the wire. The black dots represent the experimental data. Smaller nanowires are extremely flexible and a 20 nm NW spanning a 300 nm trench can be elastically deformed up to 15 times its radius before failure. The solid line shows the predicted behaviour of a perfect material with strength of 15 GPa using the generalised model developed here. There is excellent agreement between the experiment and this predicted behaviour, demonstrating the accurate description of the mechanical deformation by the generalised model. The dashed line shows the predicted behaviour of this same nanowire using the classic beam-bending-only theory. The latter predicts that the NW

would need to be bent much more than is observed experimentally, hence greatly over-estimating its mechanical performance.

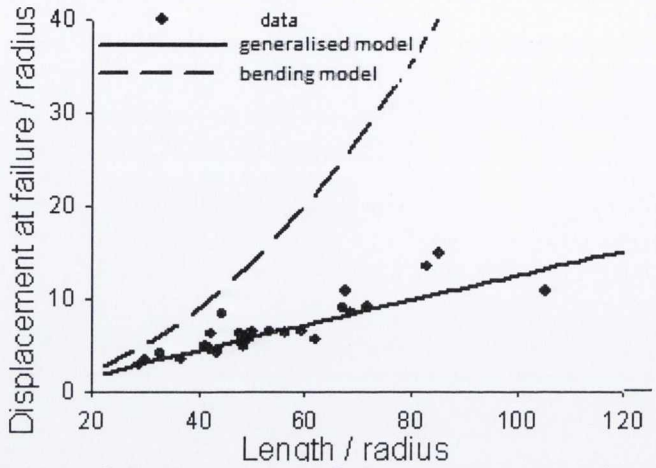


Figure 39. Plot of displacement at failure versus NW radius (normalised to length)

Conclusion

In conclusion nanowires of diameters from 40 to 160 nm were fabricated and their mechanical properties tested using an AFM-based method. We have established that for the diameters studied their Young's modulus is similar to bulk. We developed a generalised model for NW strength and demonstrated that Ge NWs grown by SCF method exhibit the maximum theoretical strength. The NWs are expected to be valuable building blocks in the development of future nanoscale devices. In addition the resilience of these Ge NWs and their ability to store energy makes them prime candidate for sensors and electromechanical oscillators.

References

1. Bardeen, J.; Brattain, W. H., THE TRANSISTOR, A SEMI-CONDUCTOR TRIODE. *Physical review* **1948,** *74* (2), 230-231.

2. Wortman, J. J.; Evans, R. A., Young's Modulus, Shear Modulus, and Poisson's Ratio in Silicon and Germanium. *Journal of Applied Physics* **1965,** *36* (1), 153-156.

3. Roundy, D.; Cohen, M. L., Ideal strength of diamond, Si and Ge. *Physical Review B* **2001,** *64*, 212103.

4. Tabib-Azar, M.; Nassirou, M.; Wang, R.; Sharma, S.; Kamins, T. I.; Islam, M. S.; Williams, R. S., Mechanical properties of self-welded silicon nanobridges. *Applied Physics Letters* **2005,** *87*, 113102.

5. Heidelberg, A.; Ngo, L. T.; Wu, B.; Phillips, M. A.; Sharma, S.; Kamins, T. I.; Sader, J. E.; Boland, J. J., A generalized description of the elastic properties of nanowires. *Nanoletters* **2006,** *6* (6), 1101-1106.

6. Paulo, A. S.; Bokor, J.; Howe, R. T.; He, R.; Yang, P.; Gao, D.; Carraro, C.; Maboudian, R., Mechanical elasticity of single and double clamped silicon nanobeams fabricated by the vapor-liquid-solid method. *Applied Physics Letters* **2005,** *87* (5), 053111.

7. Hoffmann, S.; Utke, I.; Moser, B.; Michler, J.; Christiansen, S. H.; Schmidt, V.; Senz, S.; Werner, P.; Gosele, U.; Ballif, C., Measurement of the bending strength of vapor-liquid-solid grown silicon nanowires. *Nanoletters* **2006,** *6* (4), 622-625.

8. Ngo, L. T.; Almecija, D.; Sader, J. E.; Daly, B.; Petkov, N.; Holmes, J. D.; Erts, D.; Boland, J. J., Ultimate-strength germanium nanowires. *Nano Letters* **2006,** *6* (12), 2964-2968.

9. Smith, D. A.; Holmberg, V. C.; Lee, D. C.; Korgel, B. A., Young's Modulus and Size-Dependent Mechanical Quality Factor of Nanoelectromechanical Germanium Nanowire Resonators. *J. Phys. Chem. C* **2008,** *112*, 10725-10729.

10. Menon, M.; Srivastava, D.; Ponomareva, I.; Chernozatonskii, L. A., Nanomechanics of silicon nanowires. *Physical review B* **2004,** *70*, 125313.

11. Kang, K.; Cai, W., Brittle and ductile fracture of semiconductor nanowires - molecular dynamics simulations. *Philosophical Magazine* **2007,** *87* (14-15), 2169-2189.

12. Islam, M. S.; Sharma, S.; Kamins, T. I.; Williams, R. S., Ultrahigh-density silicon nanobridges formed between two vertical silicon surfaces. *Nanotechnology* **2004,** *15* (5), L5-L8.

13. Meirovitch, L., *Analytical Methods in Vibrations*. The Macmillan Company: New York, 1967.

14. Hanrath, T.; Korgel, B. A., Nucleation and Growth of Germanium Nanowires Seeded by Organic Monolayer-Coated Gold Nanocrystals. *Journal of American Chemistry Society* **2002,** *124* (7), 1424-1429.

15. Spiner, S.; Cleek, G. W., Temperature Dependence of Young's Modulus of Vitreous Germania and Silica. *Journal of Applied Physics* **1960,** *31*, 1407-1410.

16. Landau, L. D.; Lifshitz, E. M., *Theory of elasticity*. Oxford, 1970.

17. Research highlights. *Nature* **2006,** *444* (7119), 522-523.

18. Barret, C. R.; Nix, W. D.; Tetelman, A. S., *The principles of engineering materials*. Prentice Hall: Englewood Cliffs, NJ, 1973.

4. Mechanical properties of germanium nanowires with diameters below 20 nm

4.1 Motivation

Does continuum elastic theory work for nanoscale systems? This question is at the centre of many discussions and grant proposals in research labs across the globe. The answer is most likely no. It is well known that surface atoms, having lower coordination numbers than the bulk, reconstruct to minimise this difference in coordination. Atoms bonding configurations deform or additional atoms (so-called adatoms) attach to the surface to fill the dangling bonds. These deviations from the bulk bonding propagate some distance into the bulk. The mechanical properties of the surface are then different than that of the bulk. It is then expected that when the diameter of a nanowire is close to this propagation length, mechanical properties such as Young's modulus should become size-dependent. There are two ways to go about proving this assumption: experimental observations and computational simulations. However the same systems are rarely studied by both techniques and it is difficult to draw firm conclusions. Most calculations report studies on ultra thin nanowires with diameters less than 5 nm while most experiments are performed on NWs with diameters above 20 nm. The reason for the latter is that it is difficult not only to fabricate very small wires but to manipulate them and study their mechanical properties. In addition, while it is possible for simulations to quantitatively take into account the surface effects, it is much more difficult to achieve this level of accuracy during experiments. By limiting the number of surface atoms during a numerical simulation it is possible to accurately account for surface reconstruction and determine the penetration distance (or strain field associated) with the reconstruction. Consequently simulations and experiments do not always agree concerning the mechanical properties of nanowires at these small diameters. In Table 6 we detail these issues with two most frequently studied nanowire systems: silicon and zinc oxide. The range of diameters studied is displayed as well as the behaviour of the Young's modulus, E, with decreasing diameters. It is important to note that this behaviour (increase, decrease of constant) is relative to the bulk.

Table 6. Diameter D and Young's Modulus E changes as D decreases (↙: E decreases with D, ↖: E increases as D decreases and —: E is constant over the range of D studied) for Si and ZnO NWs depending on simulations or experiments

	Simulations				Experiments			
	D (nm)	E change as D decreases			D (nm)	E change as D decreases		
		↙	↖	—		↙	↖	—
Si NWs	0.7 - 2.6[1]	X			39 - 400[2]			X
	0.5 - 4[3]	X			15 - 60[4]	X		
ZnO	0.7 –1.8[5]		X		18 - 204[6]		X	
NWs	5 - 20[7]		X		20 - 400[7]		X	
	1 - 3[8]		X		17 - 550[9]		X	
					18 - 304[10]			X
					25 - 134[11]		X	

From this table there is an obvious discrepancy in the diameters studied by both methods. There is no overlap in diameter range between numerical simulations and experimental observations. In addition, experimental studies observed a change in modulus from the bulk value for diameters between 20 and 80 nm. Simulations expect variations in the modulus to start at diameters below 5 nm. While in some cases both experiment and computational studies reported a decrease of the modulus from the bulk, because they are referring to different ranges of diameters, the results are not comparable. In only one instance are the results comparable, Agrawal et al purposely combined experimental and computational approaches for the study of the mechanical properties of ZnO NWs[7,12]. There is an obvious need for more data acquired for diameters between 5 and 30 nm. It is also important to note that the work reported on in this table do not always refer to the same crystallographic orientation, though ZnO [0001] is the most studied. Any comparisons must be carefully analyzed.

Interestingly it is predicted computationally that the modulus of Si NWs will decrease as their diameter becomes smaller while the modulus of ZnO NWs should increase. For both systems surface reconstruction was reported as being the main factor for these size

effects. For ZnO in particular surface reconstruction together with long-range ionic interactions are believed to give rise to surface effects. For the ZnO NWs a core-shell model is used to analyse the data and its main assumption is that the shell has a higher modulus than the core. Stan et al[11] introduced a core-shell model to explain the increase of ZnO modulus as the diameter decrease, described in Equation 1 where R_{NW} and E_{NW} are respectively the radius and the modulus of the NW, R_C is the radius of the core, t is the thickness of the shell and E_S is the modulus of the shell.

Equation 1

$$\frac{R_{NW}}{E_{NW}} = \frac{t}{E_S} + \frac{R_C}{E_S}$$

They found that a shell of thickness 12 nm with a modulus of 190 GPa and a core of modulus 95 GPa provided the best fit for their data. However the authors were conscious of the simplification their model creates by assuming a shell of constant modulus and thickness. Indeed, the strain experienced by the surface layers due to reconstruction is dependent on the nanowire diameter. In addition their approximation means that the thickness and the shell modulus correspond respectively to the radius and modulus of the smallest nanowire tested. Their model is then only valid for the range of diameter studied.

Another core-shell model was developed by Chen et al[9] in 2006 for ZnO NWs and it is described in Equation 2 where E and I are the modulus and moment of inertia of cross section with subscripts of C and S for core and shell respectively.

Equation 2

$$EI = E_c I_c + E_S I_S$$

Assuming a cylindrical cross section of the nanowire, we can rearrange the previous equation into Equation 3 where r_S is the radius of the shell and D the diameter of the NW.

Equation 3

$$E = E_0 \left[1 + 8\left(\frac{E_S}{E_0} - 1\right)\left(\frac{r_S}{D} - 3\frac{r_S^2}{D^2} + 4\frac{r_S^3}{D^3} - 2\frac{r_S^4}{D^4}\right)\right]$$

Using this equation the authors find a shell of 4.4 nm in radius with a modulus of 208 GPa, 1.5 times that of the core. It is possible to extend this model to other nanostructures with similar surface relaxation as ZnO such as GaN. This same model was used in 2008 by Agrawal et al[7] where they linked the results from the model to atomistic simulations. The individual contribution of surface atoms and bulk atoms at 0 K to the Young's modulus was also plotted and is reproduced here in Figure 40. It was found that

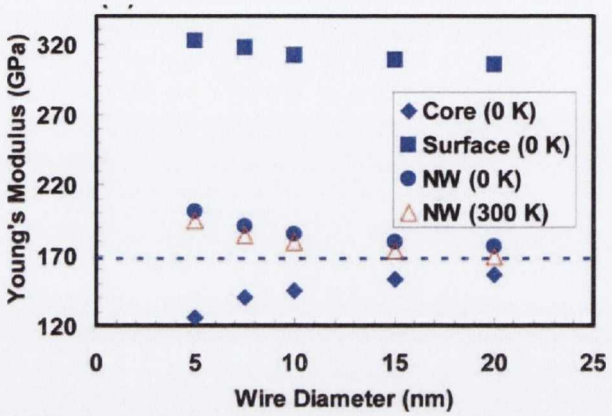


Figure 40. Computational results showing the Young's modulus variation with diameter for ZnO NWs at 0 K and 300 K[9]

surface atoms show much higher modulus than core atoms. In addition the modulus of the core atoms decreases with smaller diameters while the surface atoms exhibit a slight increase. For a simple spring-mass model where electrostatic interactions prevail, the authors report that the Young's modulus is expected to be proportional to the inverse of the distance to the fourth power[13]. The authors then attribute the higher modulus found for surface atoms to a local rearrangement of atoms leading to a decrease in interatomic spacing resulting in an increase of modulus. In addition the authors note that the assumption of a shell of constant radius is not correct. The dependence of shell thickness on the wire size is attributed to long-range electrostatic interactions. The core atoms do not exhibit bulk-like behaviour but that of a softer material and this behaviour is more pronounced as the wire diameter decreases.

Similar reports with both computational and experimental studies for Si NWs are not available to the best of our knowledge. However, it has been reported by Park in 2008 that in the case of fixed-fixed boundary conditions surface stresses cause significant deviations in the resonance frequencies of Si NWs as compared with continuum beam theory applied to bulk[14]. The authors found a threshold of 30 nm for fixed-fixed

boundary conditions upon which the resonance frequency of the nanowire is greatly reduced, which will result in a decrease of Young's modulus, expected from calculations[3]. Interestingly, the difference in resonance frequency from beam theory scales with the NW aspect ratio (length/radius) not surface area to volume ratio. In the case of fixed-free boundary conditions, surface stresses do not affect the resonance frequency nearly to the same extent. The latter only substantially deviates from the bulk value for NWs of diameters smaller than 10 nm or for very large aspect ratio.

The previous report sheds light on an interesting issue: how does the technique used to measure the mechanical properties of NWs affect them and/or the results, especially for smaller NWs. Assumptions that were valid for larger NWs might not be valid for smaller ones, in particular when surface stresses have a large influence on the mechanical properties. It is then essential to investigate these surface effects in conjunction with mechanical measurements. Computational simulations should be performed on similar size nanowires with same crystal orientation. Representing the nanowire as a core and a shell of different moduli is a valid model but simplifications such as shell of constant diameters for different diameters wires should may not be valid.

In this chapter we will present data acquired on germanium nanowires with diameters less than 20 nm using the AFM based method described previously. We will also present an improvement from this method critical for small nanowires. Finally we will introduce a new method to determine the mechanical properties of very small nanowires.

4.2 Mechanical measurements on small Ge NWs

4.2.1 Nanowires synthesis

Nanowires were synthesised in Dr Justin Holmes group in UCC using a super critical fluid method developed previously[15]. To achieve such small diameters, the synthesis was performed from gold nanoparticles (Au NPs) capped with perfluorodecanethiol which prevents the Au NPs agglomeration during synthesis. Diphenylgermane precursor was pressurised to 27 MPa and injected with the Au NPs into the reaction cell at 380 C with super critical CO_2. Figure 41 shows TEM and SEM micrographs of the gold nanoparticles (A) and the germanium nanowires after synthesis (B, C and D). Figure 41C highlights the different diameters found in a single dispersion. The choice of the synthesis temperature

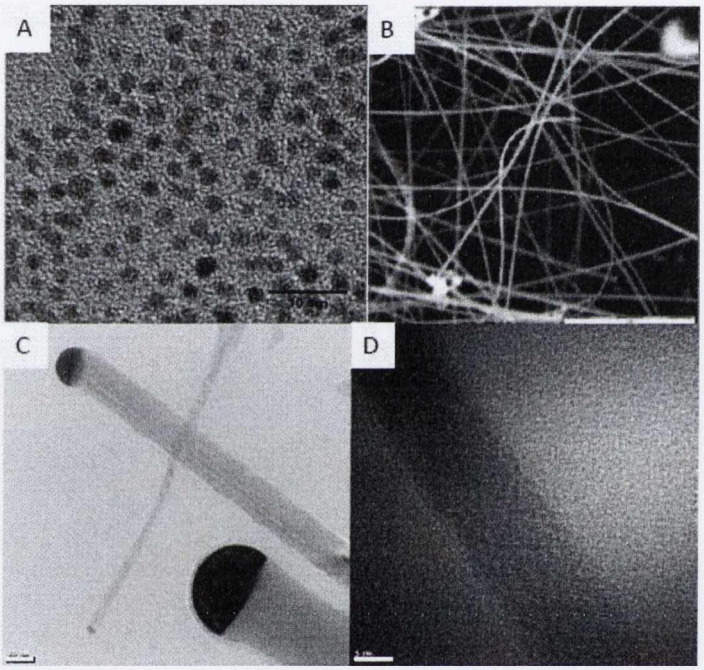


Figure 41. A) TEM image of Au NPs. B) SEM image of Ge NWs after synthesis. C) TEM image of three Ge NWs capped with Au NPs. D) TEM image of a single crystal Ge NWs of 10 nm in diameter.

is paramount to the quality of the wires. The optimum temperature range was reported to be 350 to 400 C[15]. In this range other considerations have to be taken into account. To prevent the Au NPs from agglomerating and to endure small diameter wires the temperature should stay quite low, as the diameter is directly proportional to the temperature. However, at low temperature the reaction is kinetically driven, not thermodynamically which results in a higher density of defects, as we will see in the next section.

4.2.2 Standard AFM technique

Following the procedure described in Chapter one, germanium nanowires with diameters from 10 nm to 80 nm were mechanically tested. While our main interest lies in the smaller nanowires, the Ge NWs solution contains all diameters. In addition the smallest nanowires are generally shorter which makes it more difficult for them to lie across trenches. A significant amount of these NWs were found to be sagging, hence touching the bottom of the trench, making their mechanical characterisation impossible using the present methods. Nevertheless, while the yield was quite low, 47 Ge NWs were mechanically tested and analysed following the method described in Chapter 1 and 2. Figure 42 displays the Young's modulus E (upper panel) and the strength σ (lower

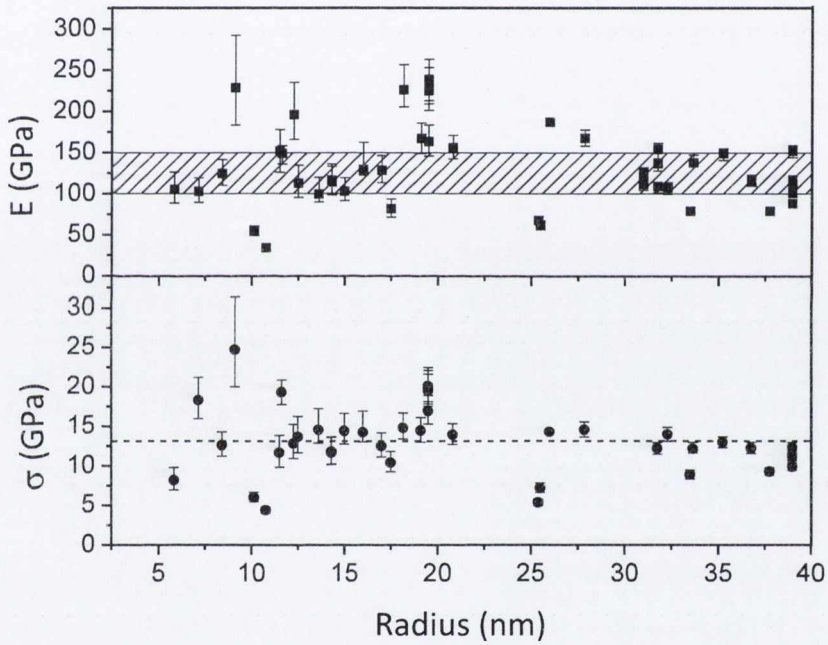


Figure 42. Plot of Young's modulus E and strength σ for Ge NWs of radius from 5 to 40 nm. Values calculated assuming an uniform beam of germanium.

panel) determined for these NWs. The hashed box in the upper panel represents values for Young's modulus depending on the crystal orientation of germanium. The dashed line on the strength graph represents the calculated average strength of 13.1 GPa ± 4.2 GPa. For NWs of radius larger than 12 nm, both The Young's modulus E and the strength σ exhibit similar values as found previously for larger NWs (see Chapter 2). However, for smaller NWs, values for both modulus and strength exhibit significant scatter. This scatter can come from mainly two sources: oxide layer not being completely removed on some NWs and non cylindrical NWs due to faceting, stacking faults and defects. The

latter would change the assumptions of our experiment as we would not be dealing with a double-clamped beam of uniform bonding arrangement and diameter as our model requires. The former would mean that we are actually dealing with a core-shell beam with a Ge core and a Ge oxide shell. As we do not know the dimensions of the oxide or core it is impossible to extract modulus or strength values from the F-d curves.

However, data other than modulus and strength can be extracted from the F-d curves. A plot of the displacement at fracture as a function of the radius is displayed in Figure 43.

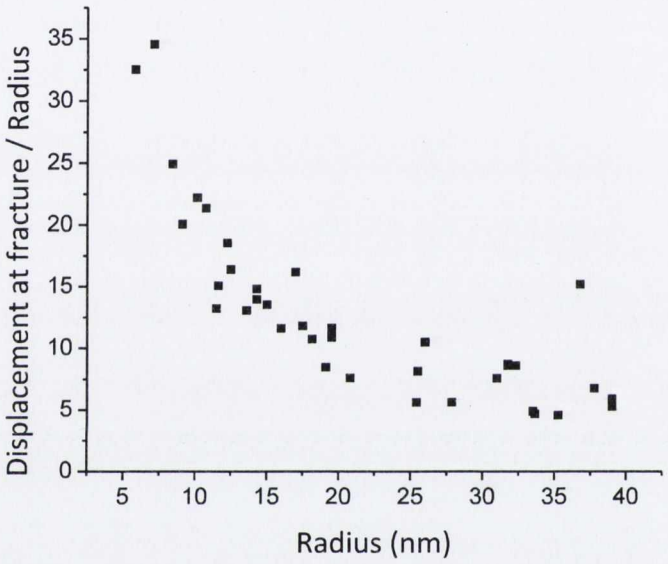


Figure 43. Plot of displacement at failure in radii versus NW radius

Larger NWs (radius above 25 nm) can only be deformed 5 to 10 times their radii on average. However as the radius of the NW decreases, the latter can be increasingly more elastically deformed, with the smallest NWs deforming up to 35 times their radii before failure. This extraordinary large resilience and the NWs ability to store elastic energy suggest great potential applications as sensors and mechanical resonators.

We carried out a HRTEM study on over 40 NWs to determine the possible origins for the scatter in the data: oxide layer or crystal defects. Figure 44 displays the main types of NWs found: large oxide with varying thickness, high defect density and non cylindrical NWs. Figure 44A displays a NW with large and non uniform oxide while Figure 44B depicts a superstructure-like NW with high density of stacking faults as shown on the inset which is a diffraction pattern of the NW. Figure 44C is a TEM micrograph of a cross section of 10 nm diameter NW exhibiting three domains and Figure 44D shows stacking

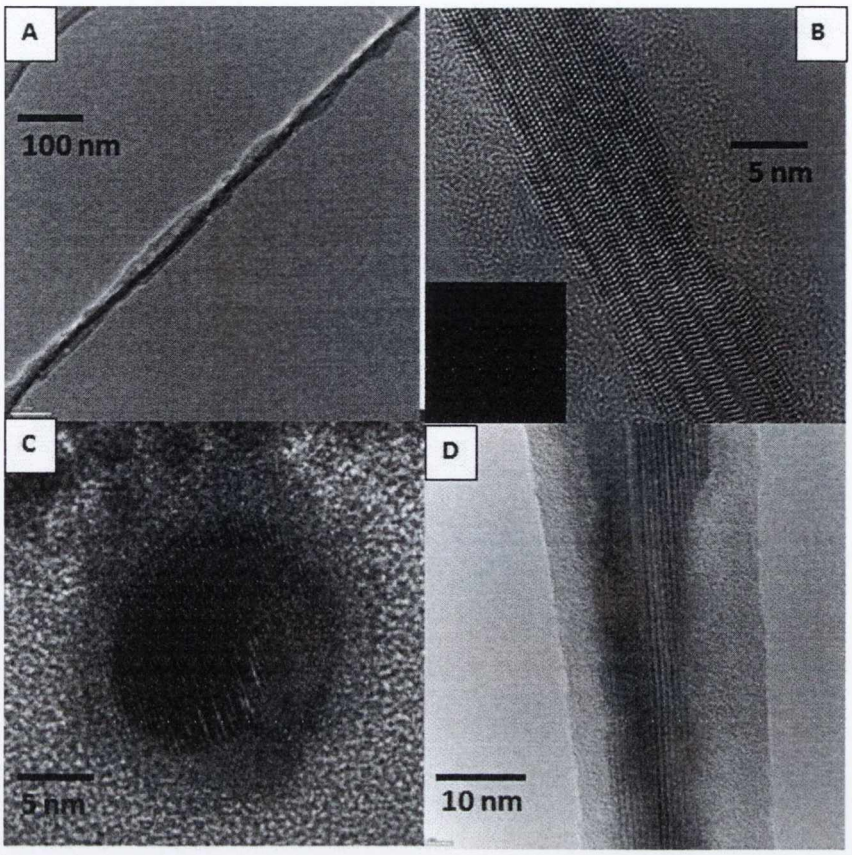


Figure 44. TEM images of Ge NWs showing major defects found in the dispersion, A) NW with large and non uniform oxide, B) superstructure-like NW with high density of stacking faults, inset is diffraction pattern of NW, C) cross section of 10 nm diameter NW exhibiting three domains, D) NW showing stacking fault resulting in non cylindrical NW.

faults resulting in non cylindrical NW. It was not possible to use these same nanowires in mechanical studies. That the synthesis resulted in such a large fraction of defective NWs was likely due to changes in pressure or temperature during synthesis of the NWs. Nevertheless we conducted a TEM study to observe the growth of the oxide over time in the dispersion depending on solvent used. We put a wafer with freshly synthesised NWs into four different solvents: water, isopropanol (IPA), toluene and chloroform. Using a dry transfer technique we looked at the NWs before dispersing them into the solvent and found that on average the oxide layer did not exceed 2 nm and a large majority of NWs exhibited stacking faults. For the NWs that were dispersed into the solvents, the solution was sonicated for 30 sec before dropping some on a TEM grid. After one week in each solvent, we found that the oxide layer thickness had not changed regardless of the solvents. We did notice that water was a very poor solvent as it will not provide a homogenous dispersion of NWs. We also noted that toluene and chloroform, while both

HPLC grade, provided quite dirty dispersion frequently leaving solvent stains on the surface. Since the oxide thickness had not changed over a week in IPA, we decided to use this solvent from that point forward.

4.2.3 Improved method for mechanical measurements

In order to determine the root cause of the scatter in the data at small radii, another method was developed. Mechanical measurements were performed in air directly on a TEM grid and the resulted were imaged afterward by TEM. The first experiments following this technique were performed on holey carbon grids. Figure 45 displays the sequence of events during the experiment. Figure 45A shows an SEM image of a Ge NW pinned to the holey carbon of the TEM grid. Figure 45B and C show AFM images of the NW before and after break. Figure 45D shows a TEM image of the broken NW and Figure 45E is a high resolution image of the fracture showing crystal orientation of the NW. From this last image we can see the brittle fracture of the NW with a fracture plane

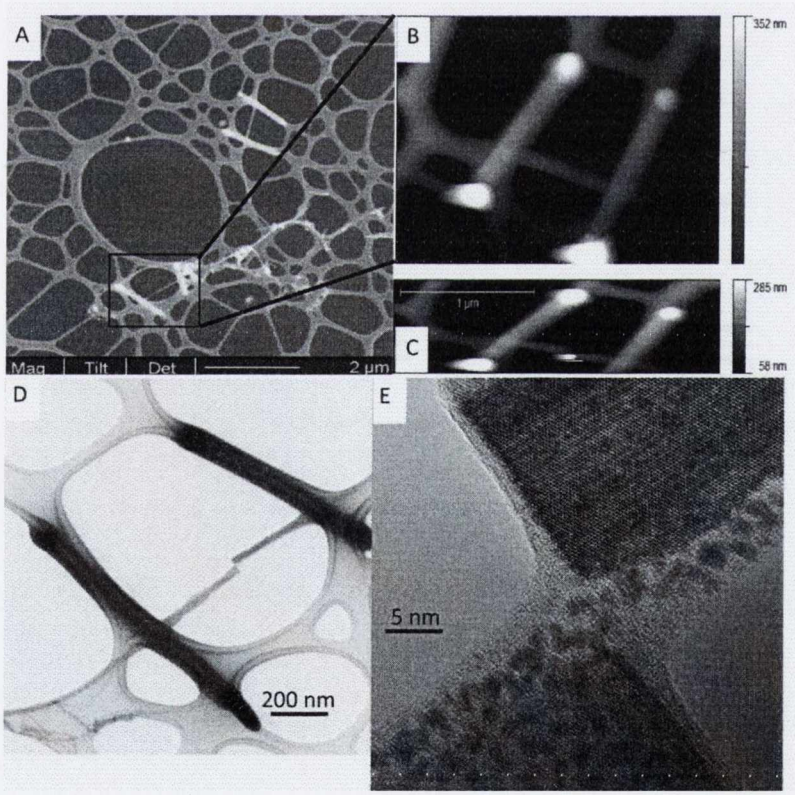


Figure 45. Images showing the sequence of events to perform mechanical measurements on a TEM grid. A) SEM image of pinned NWs on holey carbon TEM grid, B) AFM image of one pinned NW before manipulation, C) AFM image of same NW after break, D) TEM image of same broken NW as in C) and E) HRTEM image of the break region showing NW growth direction to be [112] brittle fracture, carboneous layer from EBID and oxide.

perpendicular to the NW growth direction. The oxide layer grown on the NW after the break is also visible on this image. The layer of amorphous material surrounding the NW is composed of both the oxide and some re-deposition material from EBID Pt. This problem was reported previously[16] and greatly deteriorates the quality of the TEM image. It is also difficult to quantify how much of this carboneous layer affects the mechanical properties of the NWs. We can only assume that the material is merely deposited on the surface and not covalently bonded, which should minimise its influence on the modulus and strength of the NW. In addition, while this method provides great insight into the atomic structure of the fracture of brittle materials, it has major disadvantages. The holey carbon film is not rigid and when the NWs are loaded by the AFM tip, the compliance of the carbon film changes the response of the force-displacement curve and makes it impossible to extract the mechanical properties of the NW.

For this reason we then purchased lithographically designed Si_3N_4 grids from SPI supplies, which are known to be mechanically robust. These grids have a 0.5 mm^2 window of 50 nm thick SiN with arrays of 2 µm holes located 2 µm apart. SiN is much stiffer than carbon and provides enough rigidity to carry out quantitative mechanical measurements on NWs. Nanowires were then dropped on the grid and the solvent was evaporated by gently flowing N_2 on the surface. Very few NWs were found lying over holes and we detail two NWs of similar diameters here. The first NW and its force-displacement curve are displayed on Figure 46. This NW was single crystal, as shown by

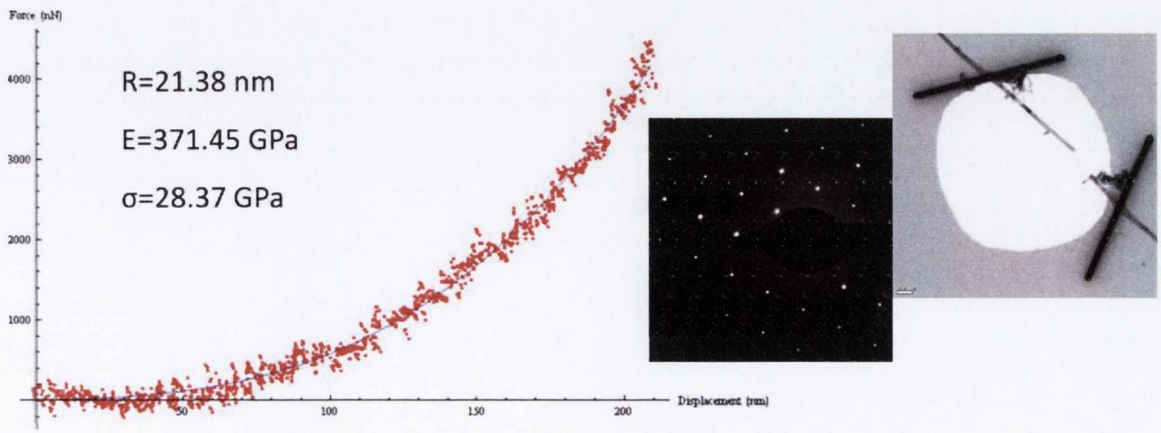


Figure 46. Force-displacement curve (red dots are data points and blue curve is fit from model detailed in Chapter 3), TEM micrograph and SAED pattern of Ge NW characteristic of a single crystal

the selected area electron diffraction pattern (SAED). HRTEM could not be performed on the broken piece of wire due to vibration. The radius of the NW was acquired on a section of the NW that was lying on the substrate. The analysis of the force-displacement curve using the generalised model described in Chapter 3 and Appendix B lead to fitting the data (red dots) with a curve (blue line) from which we can extract Young modulus and strength of the wire. For this particular NW the Young's Modulus was calculated to be 371.45 GPa and the strength to be 28.37 GPa. Both these values greatly exceed bulk. At such large radius it would be surprising for surface effects to influence the mechanical properties of the NW. We are in the process of acquiring similar data on a statistical amount of NWs to be able to draw conclusions.

Figure 47 displays the second NW we consider here. In this case the NW is not single

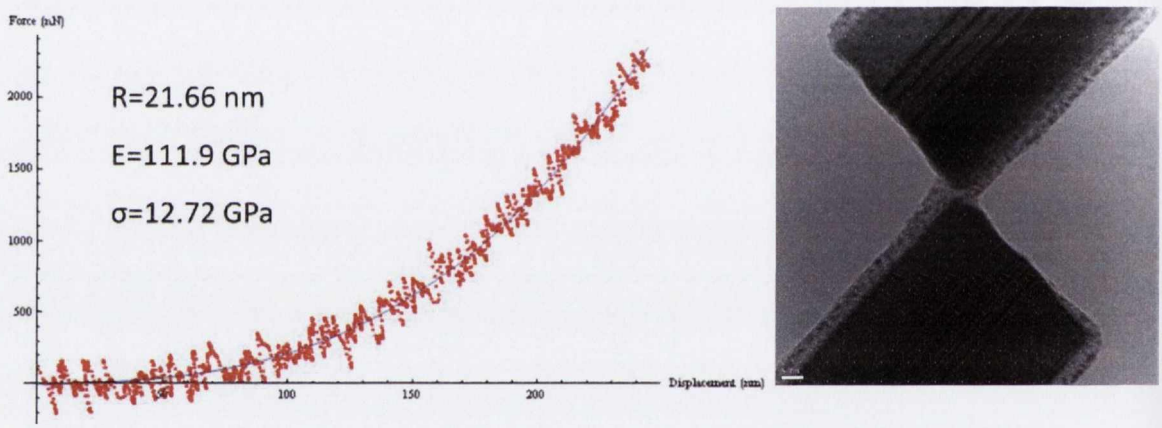


Figure 47. Force-displacement curve (red dots are data points and blue line is fit from model developed in Chapter 3) and HRTEM micrograph of a Ge NW broken by AFM manipulation showing high density of stacking faults at its centre

crystal but exhibits a large density of twins concentrated at its core. The same analysis as described for the first NW was carried out here and the Young's Modulus and strength were calculated to be 111.9 GPa and 12.72 GPa respectively. These values are less than half of the single crystal NW and are of the order of magnitude of the bulk. It is interesting to note that while this NW exhibits a large density of crystallographic faults at its core, its strength remains quite close to the ultimate strength reported in Chapter 3, 15 GPa.

HRSEM was carried out to inspect the quality of the dispersion and interestingly smaller NWs were found to avoid lying over holes and much preferred to adopting curved

configurations than follow the holes in the grid, as seen in Figure 48. We had seen in section 4.2.2 that the small NWs exhibited large elastic deformation, up to 30 times their radius. This effect coupled with the strong adhesion between the NW and the surface is responsible for this behaviour. However we can determine a relationship between the stiffness of the wire, its curvature and the adhesion force to the surface. We can measure the adhesion force by pushing a NW from one position to another with an AFM tip and record the force-displacement curve. By pinning down the NW at one location and pushing it in order to change its curvature, we can relate the adhesion force, the curvature change and the area of contact with the modulus of elasticity.

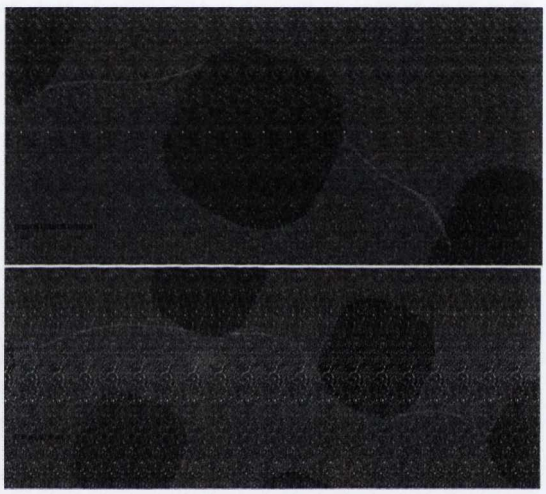


Figure 48. SEM micrographs of Ge NWs on Si_3N_4 grid. Scale bars are 1 μm.

We attempted the adhesion measurement experiment on the Si_3N_4 TEM grid. We found that if a NW is lying on the surface, the adhesion force is too strong and/or the NW too small for the AFM tip to move it, so that the tip just goes over the NW without changing its position. On the few occasions we found NWs crossing over holes, we also attempted to move them by positioning the AFM tip deep inside the hole and manipulate the NW from this position. In this configuration, the apex of the tip is situated several hundreds of nm below the NW providing much larger torque to move the latter. Unfortunately we found that the NW adhesion to the surface is so strong so that the latter would break at the point of loading rather than slide and overcome the adhesion forces. A future study would try to sputter carbon on the TEM grid to see if NWs adhere on that surface just as strongly.

Conclusion

Germanium nanowires with diameters below 40 nm were synthesised using a super critical fluid technique. Mechanical measurements using our AFM-based technique were carried out on over 40 nanowires. The Young's modulus and strength data exhibited a large scatter for diameters below 25 nm. An extensive TEM study was subsequently carried out and showed that a large majority of NWs had a high density of defects and a non-constant oxide layer. In order to tackle this issue, mechanical measurements were carried out first on holey carbon TEM grids, then on Si_3N_4 TEM grids as the latter provides more rigidity. Large NWs were mechanically deformed and broken using an AFM tip and the atomic structure of the NWs combined with modulus and strength data provided insights into the effect of stacking faults on their mechanical properties. More data is needed as no conclusion can be drawn on only 2 NWs. However setting up the AFM technique on TEM grids did not solve the problems encountered with smaller NWs. Ge NWs with diameters below 20 nm did not cross over holes but tended to preferentially adhere to the substrate, hence precluding mechanical testing. We attempted an adhesion related study to extract the modulus of the NWs but this did not provide any results because of the large adhesion force of the NWs on the surface. Future work will involve sputtering carbon onto the TEM grid to evaluate if the adhesion forces are weaker on this surface. Any quantitative future work is subject to the quality of the nanowires.

References

(1) Leu, P. W.; Svizhenko, A.; Cho, K. *Physical Review B* **2008**, *77*.

(2) Belov, M.; Quitoriano, N. J.; Sharma, S.; Hiebert, W. K.; Kamins, T. I.; Evoy, S. *Journal of Applied Physics* **2008**, *103*.

(3) Rudd, R. E.; Lee, B. *Molecular Simulation* **2008**, *34*, 1.

(4) Zhu, Y.; Xu, F.; Qin, Q.; Fung, W. Y.; Lu, W. *Nano Letters* **2009**.

(5) Wang, B.; Zhao, J.; Jia, J.; Shi, D.; Wan, J.; Wang, G. *Applied Physics Letters* **2008**, *93*, 021918.

(6) He, M.-R.; Shi, Y.; Zhou, W.; Chen, J. W.; Yan, Y. J.; Zhua, J. *Applied Physics Letters* **2009**, *95*, 091912.

(7) Agrawal, R.; Peng, B.; Gdoutos, E. E.; Espinosa, H. D. *NanoLetters* **2008**, *8*, 3668.

(8) Hu, J.; Pan, B. C. *Journal of Applied Physics* **2009**, *105*, 034302.

(9) Chen, C. Q.; Shi, Y.; Zhang, Y. S.; Zhu, J.; Yan, Y. J. *Physical Review Letters* **2006**, *96*, 075505.

(10) Wen, B.; Boland, J. J. *Physical Review Letters* **2008**, *101*, 175502.

(11) Stan, G.; Ciobanu, C. V.; Parthangal, P. M.; Cook, R. F. *Nano Letters* **2007**, *7*, 3691.

(12) Agrawal, R.; Peng, B.; Espinosa, H. D. *Nano Letters* **2009**, *9*, 4177.

(13) Newnham, R. E. *Structure-Property Relations*; Springer-Verlag: New Yok, 1975.

(14) Park, H. S. *Journal of Applied Physics* **2008**, *103*, 123504.

(15) Hanrath, T.; Korgel, B. A. *Journal of American Chemistry Society* **2002**, *124*, 1424.

(16) Zhu, Y.; Espinosa, H. D. *Proceedings of the National Academy of Sciences of the United States of America* **2005**, *102*, 14503.

5. Mechanical Properties of Individual Polymer Carbon Nanotubes Composites Fibers

5.1. Motivation

Electrospinning has been used since 1934[1] to continuously produce low diameter polymer fibers from polymer solutions or melts[5]. However, in recent years this technique has become more popular[6], principally to produce low density porous membranes[7]. By continuous electrospinning of fibers onto a stationary electrode, it is possible to form membranes some hundreds of microns thick. Potential applications suggested for these membranes range from use as bone[8] or tissue-engineering scaffolds[9] to battlefield dressings[10] and protective clothing[11]. Electrospinning can also be used to align fibers on a substrate[12] opening the possibility to obtain oriented membranes. Many polymers have been successfully electrospun[7] into thin fibers, depending on their application and process requirements. We concentrate here on poly vinyl alcohol fibers.

The water solubility of poly vinyl alcohol (PVA) makes it a prime candidate for electrospinning [13] as it can be adjusted by pH, temperature or surfactants. Moreover, the hydroxyl groups of PVA can be used for chemical reactions, prior or after electrospinning, hence the crystallinity and water resistance of fibers can be increased by chemical treatment[14]. Due to its availability with different molecular weights, its ease of use and its water solubility PVA is a widely used polymer for electrospinning. However for most applications of PVA electrospun fibers or membranes, their mechanical properties are critical both in terms of strength and mechanism of failure.

Reinforcing these fibers has become a major area of research and the fillers most widely studied are carbon nanotubes (CNT)[4, 15-21]. Discovered by Ijima in 1991[22], carbon nanotubes show great potential[23], especially due to their mechanical properties such as high modulus[24], high strength and toughness[25]. However the quality of the CNT dispersion within the matrix is fundamental to the improvement of the mechanical properties[26]. CNTs can be chemically functionalised to enhance the dispersion into the polymer and maximise polymer-nanotube stress transfer[27], this makes them the ideal candidate for mechanically reinforced composites[28]. Both single walled carbon

nanotubes (SWCNTs) and multi walled carbon nanotubes (MWCNTs) have been used as fillers to improve the modulus and strength of fibers. Their morphology and concentration are critically important in determining the mechanical properties of the fibers[29].

The bulk of work reported on mechanical properties of electrospun fibers is related to membranes; however a membrane is only as strong as its individual fibers, making the determination of their strength of paramount importance. The small dimensions (often below a micron) of electrospun fibers make their tensile properties difficult to investigate. A relatively small number of groups have studied the tensile properties of individual fibers and Table 7 displays the main results they obtained for different polymers.

Table 7. *CNT-polymer composite fibers and their tensile properties measurements details (V_f=volume fraction of CNT in fiber, PAN=polyacrylonitrile, PMMA=poly(methyl methacrylate), PBO=poly(p-phenylene benzobisoxazole.) Young Modulus and Strength displayed only for best result and percentage increase (or decrease) is in comparison to polymer only.*

Polymer	Ref, CNT type	V_f (CNT)	Fibers diameter	Method	Young Modulus	Strength	Strain at break (%)
PAN	[4], SWCNT	0 to 0.028	50-200 nm	AFM	140 GPa (133 % increase)	N/A	N/A
PMMA	[2], function-alised MWCNT	0.031	300-500 nm	Tensile tester inside SEM	267 MPa (267 % increase)	79.5 MPa (157 % increase)	N/A
PBO	[30], SWCNT	0.063	25 µm	Tensile tester	167 GPa (21 % increase)	4.2 GPa (61 % increase)	2.8 (40 % increase)

The full spectrum of mechanical properties was obtained for PBO/SWCNT fibers which have quite large diameters (25 µm) but were not electrospun. For fibers of sub-micron diameters, the determination of their strain at break has never been reported and to the

best of our knowledge only two groups have investigated the mechanical properties of individual fibers.

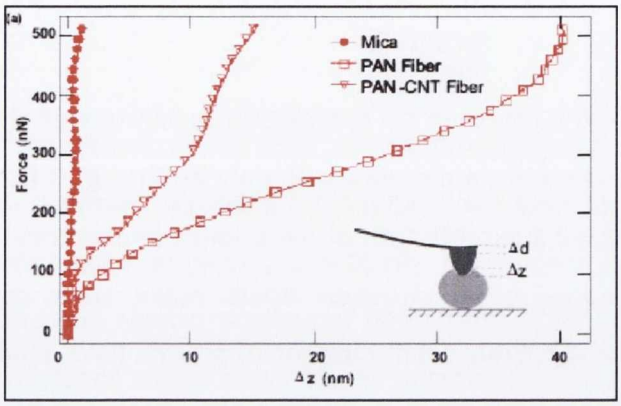


Figure 49. *Force-displacement plot of indentation experiment on PAN/SWCNT fibers*[4]

The AFM method Ko et al[4] used to study the mechanical properties of PAN/SWCNT fibers is quite interesting. They electrospun a low density of fibers directly on mica and using an AFM tip indented the fibers to test their stiffness. Figure 49 shows the Force-displacement data and a schematic of the experiment. The plot shows a non-linear load-deformation relationship where the modulus is extracted from the linear region only, i.e. small loads. The addition of SWCNT to the polymer matrix greatly enhanced its mechanical properties, with a 133 % increase in modulus for a volume fraction V_f=0.028. The radius of the contact area between the tip and the fiber is estimated to be 5nm, much smaller than the diameter of the fiber itself, preventing slipping. However this technique has obvious disadvantages: the determination of strength and strain at break is not possible. For most applications of polymer reinforced fibers, strength is pivotal.

The approach taken by Liu et al[2] provides values for modulus and strength. They electrospun PMMA/MWCNT fibers on an aluminium foil, cut the fibers towards the end of the foil to allow some fibers to be free standing at one end. The foil was then placed inside a SEM chamber and an AFM tip with a drop of epoxy glue was contacted to the mat, and became attached to a fiber. The latter was then pulled away from the mat and its other end was glued to the SEM stage. The stage was then slowly and controllably pulled away from the tip and the experiment was video-recorded. Strain-stress plots were gathered for functionalised MWCNT/PMMA fibers, as shown on Figure 50, and increases in modulus and strength of 267 % and 157 % respectively were reported. The scatter in the data is quite significant as strains at failure from 25 % to 165 % are found

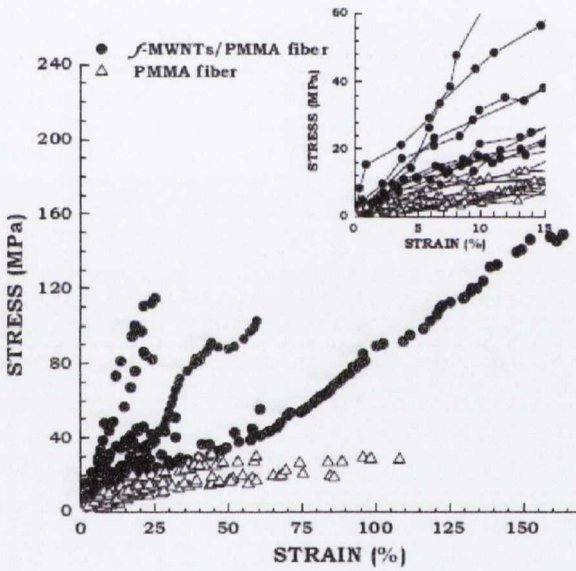


Figure 50. *Stress-strain curves for electrospun PMMA and MWCNT/PMMA fibers[2]. The inset is a magnified view of the plot at low strain.*

for MWCNT/PMMA fibers. Liu et al argued that this behaviour is due to the inhomogeneous dispersion of the CNT within the fibers, correlated by TEM images reproduced here in Figure 51. The high speed at which the fibers are electrospun might not allow for enough time for the MWCNT to orient themselves and disperse homogeneously within the polymer matrix. Moreover, electron beam influence from the SEM has to be taken into account here as it can greatly affect the polymer through thermal degradation. While this technique provides interesting results in terms of mechanical properties and insight into the dispersion of CNT within the matrix, the scattering of the data results in large errors in the modulus and strength (50 and 58 % respectively).

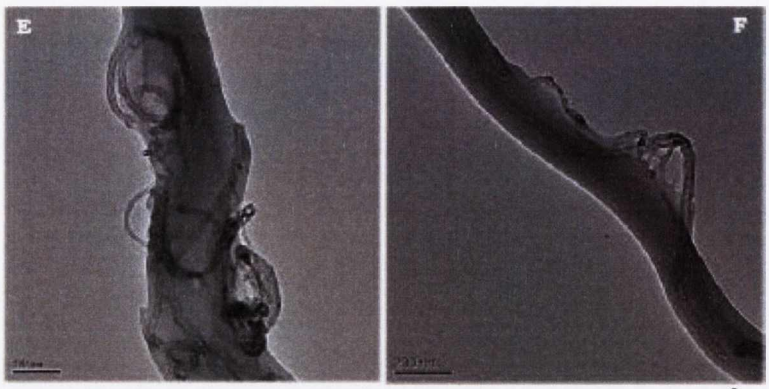


Figure 51. *TEM micrographs of MWCNT/PMMA fibers*[2]

The full spectrum of mechanical properties of SWCNT/PBO was investigated by Kumar et al[30] using an universal tensile machine. This was made possible thanks to the large diameter of these fibers (25 μm). It has to be noted that these fibers were not electrospun but piston-driven-spun, allowing much larger diameters of fibers, hence easier handling for mechanical measurements. However they constitute an interesting example of mechanical properties measurements of individual fibers as their strength is the highest ever reported (4.2 GPa). Another example of strong polymer-CNT composite fibers was reported by Dalton et al[3] in 2003 where they used a type of coagulation-based carbon nanotubes spinning method[31] to prepare fibers containing up to 60 %wt SWCNT and demonstrating tensile strength of 1.8 GPa. They also compare their results

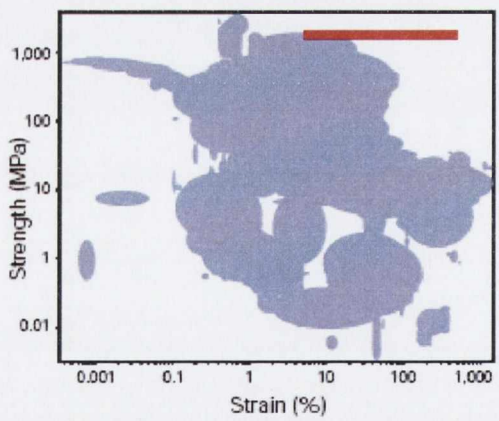


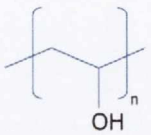
Figure 52. *Comparison of the strength and failure strain for carbon nanotubes composite fibers*[3]*. Lavender field represents all polymers from Cambridge Materials Selector database and red line represents data from Dalton et al*[3]*.*

with other polymers from the Cambridge Materials Selector database, show on Figure 52. The red line displays the strength and strain for different degrees of initial pre-draw and the lavender field represent the 3000 materials of all types, highlighting what is available and what is needed. The polymer chosen for these fibers was PVA which we

also chose for our experiments given that strong PVA composite fibers[32], films[29] and membranes[20] have been recently reported.

5.2. Experimental procedure

The fibers used in this work were prepared by Dr David Blond in Prof Jonathan N. Coleman group in the School of Physics in TCD. The following paragraphs detail the procedure employed which was published in 2008[20].

Poly vinyl alcohol (PVA) has the following chemical structure:  PVA is commercially available as a powder and the material used in this work was purchased from Sigma Aldrich (M_w=30 000-70 000 $gmol^{-1}$). The quality of the nanotube dispersion in the PVA solution is fundamental to this work, hence water-soluble polyaminobenzene sulfonic acid (PABS) SWCNTs (purchased from www.carbonsolution.com) were chosen and showed the highest quality nanotube dispersions[27]. The same concentration of PVA (250 gL^{-1}) was used to prepare the PVA/PABS-SWCNTs solutions but several mass fractions of SWCNTs (from 1 wt% down to 0.06 wt%) were investigated. Typically, each mass fraction of CNTs was first dispersed in 20mL of distilled water using a high–power sonic tip for 5 min (VibraCellCVX, 750 W, 20 %, 20 kHz). Subsequently, each solution was placed in a lower-power sonic bath for 3 h (Branson 1510, 42 kHz, 80 W). Next, PVA powder was slowly added to the solution and gently crushed with a spatula in order to minimise PVA agglomeration. Again, tip sonication was carried out for 5 min to break up any remaining polymer aggregates before placing it in a sonic bath for further 24 h until complete dissolution occurred. Finally, the solutions were sonicated with a sonic tip for 2 min immediately prior to electrospinning.

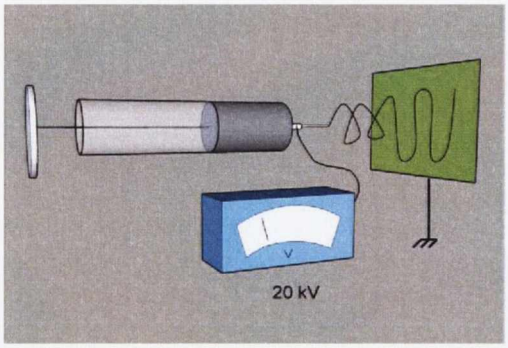


Figure 53. Schematics of electrospinning set-up

The electrospinning set up, shown on Figure 3, consisted of a 20 mL glass syringe with a 16 gauge stainless steel needle that was positioned on a horizontally moveable structure. A stationary stainless steel plate (15 cm × 15 cm) was used as a collector, hence grounded. For mechanical measurements, fibers were deposited onto pre-patterned silicon wafers with arrays of 5 μm wide trenches which were placed just in front of the steel collector. For all the experiments carried out with this set-up, the distance between the needle and the collector was set at 20 cm. The high voltage was provided by a Brandenburg high voltage generator. For each run, the voltage was kept at 20 kV. The needle was positively charged while the collector was grounded. A syringe pump (KDS 200 syringe pump) was used to ensure a constant flow rate at 0.003 $mLmin^{-1}$. Solutions were electrospun for a very short time (~45 s), resulting in a low density mesh of fibers with radii between 20 and 40 nm as shown on Figure 54. Only a few fibers are

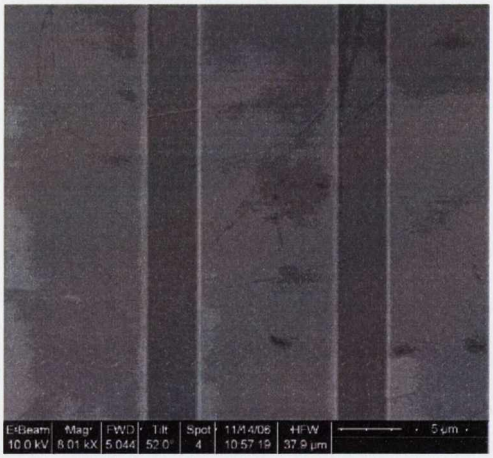


Figure 54. *SEM micrograph of SWCNT/PVA electrospun fibers on pre-patterned SiO_2 substrate*

present on the surface, avoiding the formation of a mesh and allowing measurements on individual fibers. This picture was taken at 52° tilt, showing that the fibers were not spanning across but sagging inside the trenches. We think this occurred sometimes if the

fibers were not completely dried out when they hit the surface. This did not happen often although the fact that the fibers were suspended was checked routinely.

Following the spinning of the fibers on the pre-patterned surface, AFM measurements were carried out following the procedure outlined in Chapter 1. For each SWCNT load an average of 15 fibers were tested, resulting in 103 Force-displacement curves for this system. In addition FIB cut cross-sections of the fibers were investigated under TEM as well as broken fibers. However, the polymer matrix turned out to be difficult to image as it tended to boil under the beam making the detection of CNTs within the matrix impossible. On Figure 55, the bright ellipsoid is actually a hole in the fiber caused by beam radiation (either FIB or TEM). The slightly darker shape surrounding this hole is the

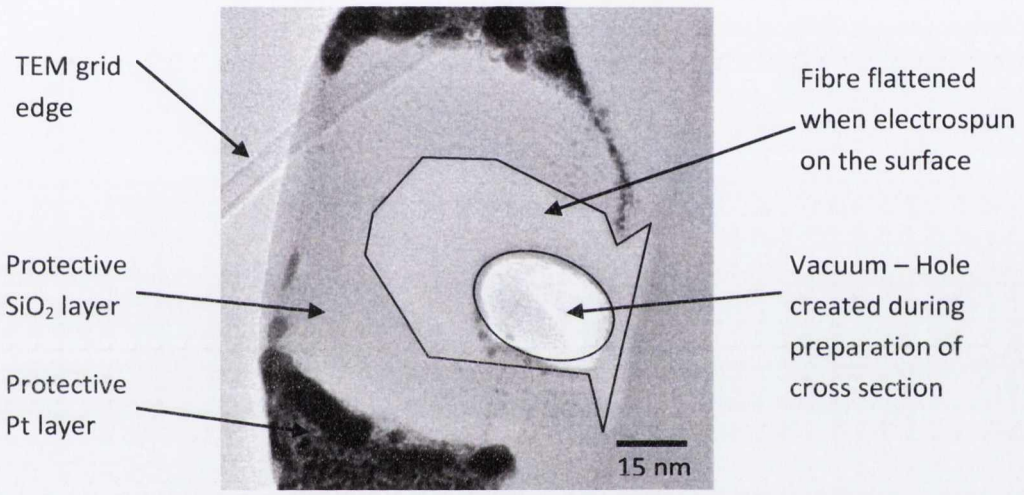


Figure 55. *TEM image of a fiber cross section showing an oval-shaped hole due to beam damage during sample preparation. Fibre not cylindrical and flattened on the surface, probably because of high impact due to electrospinning procedure.*

fiber. It is flattened on one side, probably when it was spun on the surface. We can assume that this flattening did not occur for the fibers that were spanning over the trenches, therefore our assumption that the fibers are cylindrical is still justified.

5.3. Results and Analysis

5.3.1. Force-displacement measurements

Figure 56A shows representative Force-displacement (F-Δz) curves for fibers of the different SWCNT mass fractions studied (from 0 to 1 wt%) during lateral loading. As all

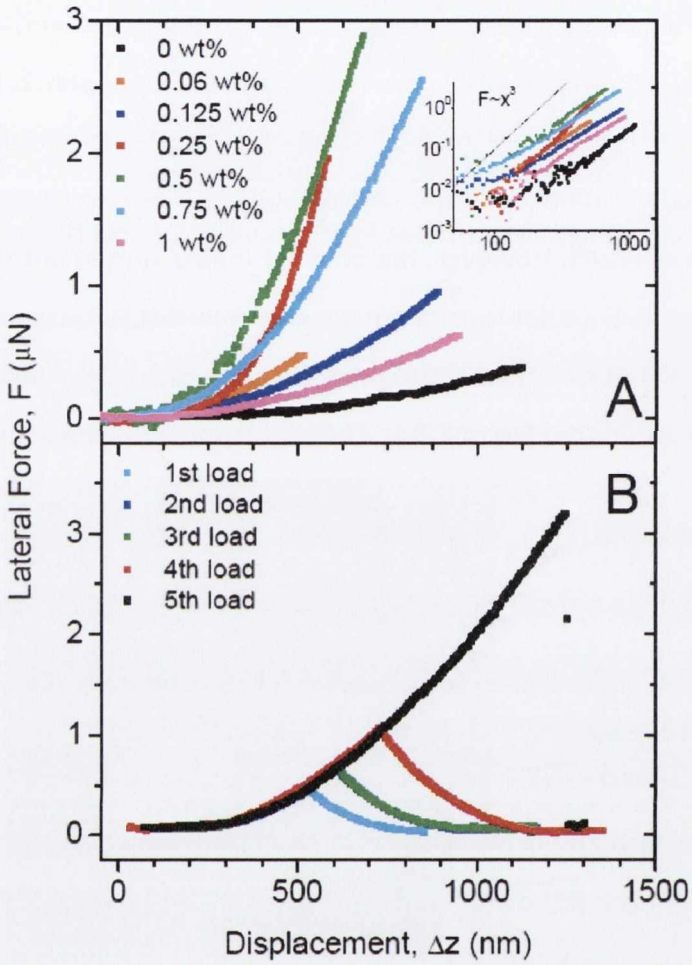


Figure 56. *Lateral force versus displacement curves for some of the fibers studied. A) Representative lateral force versus displacement curves for fibers filled with different nanotube mass fractions. Inset: the same graph displayed on a log-log scale. B) Lateral force versus displacement curves for a single fiber, strained repeatedly to different maximum values of Δz.*

fibers had diameters around the same range, we can compare their displacement at break. Fibers that extend the longest (over 1 μm) were comprised of PVA only whereas fibers demonstrating the shortest displacement before breaking had 0.06 wt% of SWCNT. Moreover the force needed to break these fibers is in the range of μN, which is quite large for such small fibers. It is interesting to note that while this behaviour is characteristic of double-clamped beam configurations for an elastic wire the present system is in fact much more complicated than a classic homogenously bonded material.

The inset in Figure 56A represents the same F-Δz curves plotted on a log-log scale. Also plotted as a dash line is the slope that corresponds to the expected cubic dependence, i.e. $F=\Delta z^3$, which is expected for elastically deformed homogenously bonded materials. The behaviour observed in this polymer-CNT composite is clearly sub-cubic for the vast majority of curves. Figure 56B shows the F-Δz curves for a 1 wt% fiber loaded 5 times until fracture (black line). The reversible behaviour demonstrates the absence of plasticity at displacements of <700 nm (<4 % tensile strain). Since there is no dramatic change of slope after 700 nm, we can assume there is no sign of plasticity before fracture. For all SWCNT loadings, fibers break at large displacement (on average 30 times their radii) and always break at the centre as shown in the AFM micrographs in Figure 57A and B. In addition, this reversible behaviour coupled with the fact that fibers always break at the point of loading (i.e. centre of suspended fiber) implies the absence of pull-out at the Pt clamps points. It is also interesting to note that on Figure 57B both sides of the broken fiber have the same brightness which means they are at the same height. The broken fibers do not sag inside the trench but seem to hold straight, a sign of a significant stiffness and absence of plastic deformation as no increase in length was

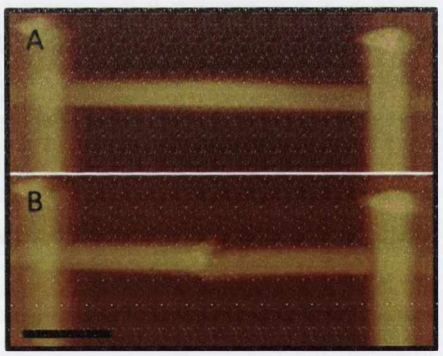


Figure 57. *AFM micrograph of a composite fiber before (A) and after (B) fracture. The scale bar is 1μm.*

recorded.

The simplest conclusions that can be drawn from these data are the force and displacement at break. These parameters are shown in Figure 58A and B respectively, as a function of nanotube content for all fibers studied here and the error bars represent the standard deviation for 10-15 measurements. For low mass fractions, the force to break is increased on adding CNTs, while the displacement at break is reduced. Some saturation is observed at higher mass fractions (from 0.5 wt%), possibly due to nanotube

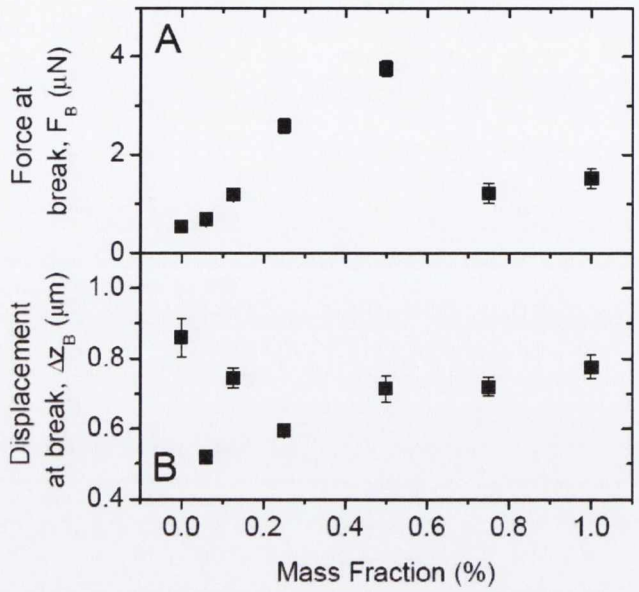


Figure 58. *Mean values for A) Force at break and B) displacement at break, as a function of nanotube mass fraction.*

aggregation. The displacement at break is more or less constant through the range of CNT loadings studied here. We can also note that the standard errors displayed on Figure 58 are rather small, showing the reproducibility and high quality of these measurements.

5.3.2. Theoretical Considerations

A theoretical model needs to be developed to extract the tensile mechanical properties of these fibers from the F-Δz data. However due to the complexity of this system (polymer chains, carbon nanotubes and likely interaction between both) we cannot successfully develop a model that would take into account all parameters. The simplest possible model, developed by Walters et al considers the fiber as an elastic string[33] and gives a relationship between the applied load, F, and the perpendicular displacement, Δz, as well as expressions for the tensile strength, σ_B, and the strain at break, ε_B. In addition, by assuming the material fails by brittle fracture, we can obtain lower bounds for tensile elastic modulus, E, and toughness T_E. In what follows, the subscript B denotes the value of a quantity when the fiber breaks. We assume that the AFM tip applies a lateral force, F, to the centre of the fiber, in a direction perpendicular to the initial fiber length as shown in Figure 59.

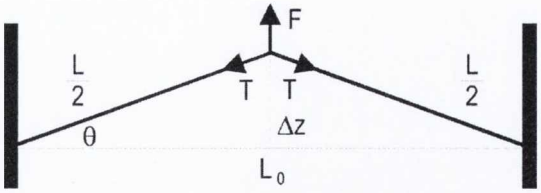


Figure 59. *Schematics of lateral loading of fiber and quantities associated*

Assuming the tension in the fiber can be written as $T = F/2Sin\theta$ and writing the fiber tensile strength as $\sigma_B = T_B/\pi R^2$, R is the fiber radius and L_0 is the initial fiber length, T_B is the tension when the fiber breaks, we can express the tensile strength as

$$\sigma_B \approx F_B L_0 / 4\pi R^2 \Delta z_B \qquad \textbf{Equation 1}$$

where F_B and Δz_B are the values of lateral force and perpendicular displacement when the fiber breaks. Similarly, we can write the strain at break as

$$\varepsilon_B = (L_B - L_0)/L_0 \approx 2\Delta z_B^2 / L_0^2 \qquad \textbf{Equation 2}$$

(L_B is the fiber length on fracture). The force displacement curves show sub-cubic behaviour (quite close to quadratic), as seen on the inset in Figure 56A, which we believe is due to a slightly sub-linear relationship between tensile stress and strain. We attribute this to non-Hookian behaviour, often observed for polymers, rather than plasticity. Repeated stretching of the fibers show no signs of plasticity for Δz<700 nm (ε<4 %) at least. However, without precise knowledge of the constitutive equation for this material, modelling of such non-ideal behaviour is extremely difficult. In the absence of further knowledge, this tensile model is a valid approximation which directly gives values for σ_B and ε_B as described above. In addition, the elastic string analysis gives a relationship between the lateral force and the perpendicular displacement Δz:

$$F \approx 8\pi E R^2 \Delta z^3 / L_0^3 \qquad \textbf{Equation 3}$$

where E is the tensile modulus of the fiber. However we note that the non-cubic behaviour observed in the measured data makes it inappropriate to use to find E. To estimate E we must make the approximation that $\sigma \propto \varepsilon$ over the whole strain range. This gives us an under estimate of the Young's modulus from $E \approx \sigma_B / \varepsilon_B$. Similarly, we can get an under estimate of the toughness from $T_E \approx \sigma_B^2 / 2E$.

5.3.3. Data Analysis

All fibers have shown brittle failure without any sign of plasticity. Since the average spanning length of the fiber is 5 μm, that the average length of a SWCNT is 1 μm and according to the concentration of nanotubes in the fiber (on average 2 CNTs per cross section for 0.5 % loading), we can expect to have at least two CNTs spanning across the trench. We speculate that failure is most likely due to pullout of the CNT from the matrix rather than an actual fracture of the polymer/CNT material.

The tensile modulus was calculated for each fiber using the tensile model as described above. The moduli values for individual nano-fibers varied between 3 and 85 GPa, depending on the SWCNT mass fraction. However significant spread in the moduli for different fibers of the same mass fraction occurred, as shown on Figure 60 which displays the modulus for fibers with 0.75 wt% of SWCNT. The modulus varies between 6 and 19 GPa for this loading. The radius of the fibers does not seem to have a major effect on the value of the modulus. Over the range of mass fractions studied, the mean moduli varied between 10 and 50 GPa. This range is not unexpected since PVA/SWNT coagulation spun fibers have shown similar moduli, varying between 10 and 80 GPa[3, 31, 34].

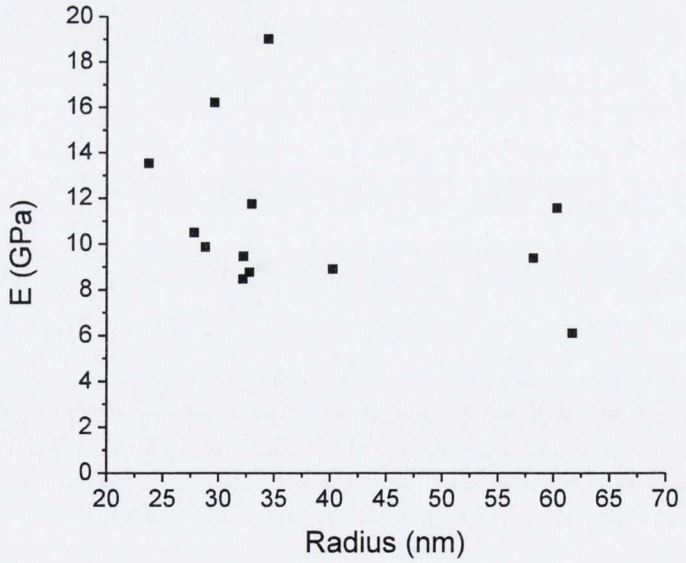


Figure 60. *Plot of tensile modulus against radius of fiber for 0.75wt% SWCNT*

The strengths of the individual composite fibers were calculated for all mass fractions using the tensile model described in Equation 1. The individual fiber strength varied

between 0.26 and 2.6 GPa. However, the mean strength calculated for each mass fraction varied from 0.5 GPa to 1.4 GPa. It is worth remembering that the model we use only provides estimates of the strength and modulus, the actual values are expected to be larger. In addition, the mechanical properties of these nanofibers are maximised for SWCNT mass fractions of 0.06 % and 0.125 % with respective strengths and moduli of 1.2 GPa and 40 GPa.

Our model is approximate, but how close to the reality is it? We can test the validity of our model fairly simply by comparing our results with others. We found that for a range of reported PVA-nanotube composites[3, 20, 35] membranes or fibers, the strength scales linearly with the modulus ($\sigma_B=0.04E$) as shown in Figure 61. We then plot the calculated strength versus the calculated modulus for our fibers. Here, the strength scales approximately linearly with the modulus as expected. However, more importantly the

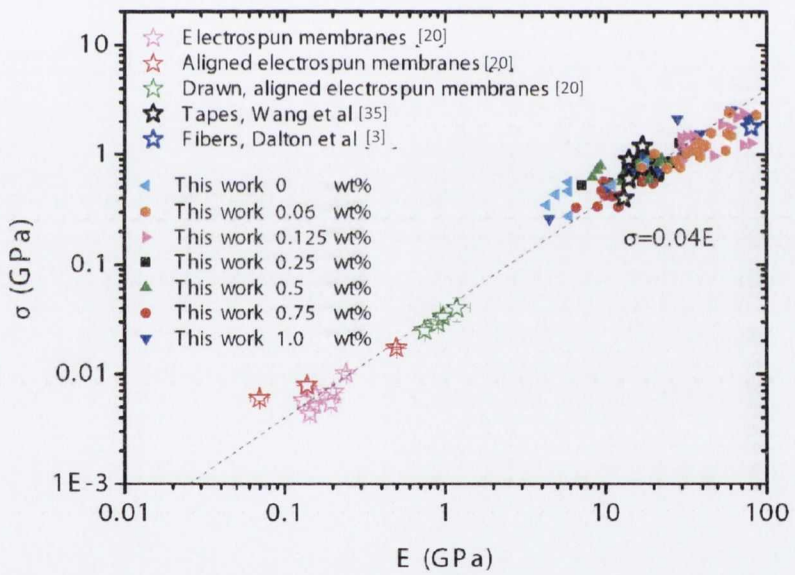


Figure 61. *Plot of fiber tensile strength versus fiber tensile modulus. Also shown are data taken from the literature, for PVA/CNT composites in form of fiber-like material or aligned tapes (stars). Note that the literature data tend to sit on a straight line defined by $\sigma=0.04E$.*

fiber data lies close to the straight line described by $\sigma_B=0.04E$ which is typical for PVA-nanotube composites. This agreement between our results and those available in the literature give us confidence that our model works reasonably well. In addition, on this same figure, our fibers data lies on the top right hand side of the slope, with high modulus and high strength values.

Mean tensile modulus, tensile strength, toughness and strain at break for these fibers as a function of nanotube volume fraction are presented in Figure 62. Note that we have transformed the nanotube content from mass fraction to volume faction to facilitate analysis using the rule of mixtures. For both modulus and strength (Figure 62A and B), significant increases are observed at low SWCNT content (<0.2 vol%), with mean

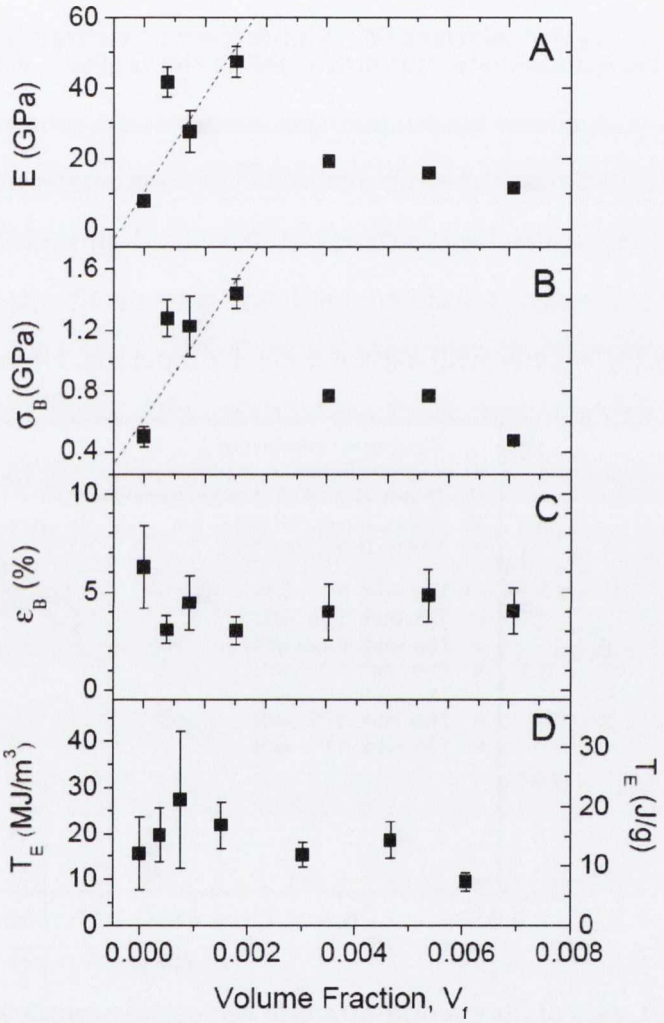


***Figure 62**. Data calculated using the tensile model, plotted as a function of composite mass fraction: A) Young's modulus E, B) tensile strength σ_B, C) strain at break ε_B and D) toughness T_E. The right axis shows the toughness plotted by mass (calculated taking ρ_{PVA}=1300 kg/m^3). The error bars are the standard errors calculated from 10-15 measurements.*

modulus and strength reaching values as high as 50 GPa and 1.4 GPa respectively. These values are at the high end of what has been observed for polymer-nanotube composite fibers[28]. The rate of increase of both modulus and strength in this regime are $dE/dV_f \sim 27$ TPa and $d\sigma_B/dV_f \sim 600$ GPa respectively. These extremely high values cannot be

explained by the standard Rule of Mixtures which can account for values of dE/dV_f and $d\sigma_B/dV_f$ no larger than the nanotube modulus and strength, respectively (~1 TPa and ~100 GPa)[21]. It is likely that some other form of reinforcement must be present to explain these results. A likely possibility is nanotube-nucleated polymer ordering which is often observed in PVA based composites[36] and is known to result in significantly enhanced mechanical properties[28, 37]. The presence of CNT in the matrix helps in the formation of crystalline-like polymer volumes around the CNT. It has been reported that these volumes could extend up to 20 nm from the nanotube[37]. At volume fractions above 0.2 vol%, both modulus and strength tend to fall off slightly. This is generally attributed to nanotube aggregation, which is unsurprising given that adjacent aligned nanotubes are typically only ~20 nm apart at a volume fraction of 0.2 vol%. At this volume fraction, a cross section of the fiber contains on average 2 SWCNTs. If both CNTs are surrounded by a crystalline volume of 20 nm in radius, most of the fiber is then made up by these volumes, reaching the highest strength and modulus.

The data for fiber strain at break and toughness are shown in Figure C and D. The strain at break, ε_B, was 6 % for a PVA only fiber and falls off slightly as nanotubes are added, saturating at ~4 %. The PVA-only fibers displayed toughnesses of ~15 MJ/m^3. On adding nanotubes, the toughness increased slightly to a maximum of 27 MJ/m^3, equivalent to 20 J/g. At higher mass fractions, the toughness fell off, in line with the fall off in strength. It should be noted that these fibers display reasonably high toughness. For comparison, Kevlar fibers have toughness in the region of 35 J/g[38]. Although our fibers are not super-tough, as has been reported for SWCNT-PVA fibers produced by coagulation spinning[3], they have one significant advantage. Their toughness comes from energy absorbed at low strain (<4 %) as is the case for Kevlar and other tough fibers[39]. By contrast, super-tough fibers tend to be tough because they are ductile[3]. However, in many cases they absorb very little energy at strains below 5 %, making them unsuitable for many applications. Thus, these electrospun fibers may be useful for ballistic-type applications requiring the absorption of large quantities of energy over small distances.

Conclusion

We have used our generalised method to study the mechanical properties of polymer composite fibers. We have measured both force and displacement as the fiber was

strained. These electrospun fibers did not exhibit any plasticity, which we attributed to CNT induced crystallisation of the polymer. We presented a simple model which we used to generate the tensile properties; modulus, strength, strain at break and toughness from the force–displacement data. We found the tensile properties were optimised around 0.05 vol% nanotubes. We have observed maximal strengths and moduli of 2.6 and 85 GPa, respectively. Optimised fibers broke at strains of 4 % having absorbed 27 MJ/m^3.

References

1. Formhals, A. Process and apparatus for preparing artificial threads. 1934.

2. Liu, L.-Q.; Tasis, D.; Prato, M.; Wagner, H. D., Tensile Mechanics of Electrospun Multiwalled Nanotube/Poly(methyl methacrylate) Nanofibers. *Advanced Materials* **2007,** *19* (9), 1228-1233.

3. Dalton, A. B.; Collins, S.; Munoz, E.; Razal, J. M.; Ebron, V. H.; Ferraris, J. P.; Coleman, J. N.; Kim, B. G.; Baughman, R. H., Super-tough carbon-nanotube fibres. *Nature* **2003,** *423* (6941), 703-703.

4. Ko, F.; Gogotsi, Y.; Ali, A.; Naguib, N.; Ye, H.; Yang, G. L.; Li, C.; Willis, P., Electrospinning of Continuous Carbon Nanotube-Filled Nanofiber Yarns. *Advanced Materials* **2003,** *15* (14), 1161-1165.

5. Ramakrishna, S.; Fujihara, K.; Teo, W.-E.; Lim, T.-C.; Ma, Z., *An Introduction to Electrospinning and Nanofibers*. World Scientific Publishing Co Pte Ltd: Singapore, 2005.

6. Dzenis, Y., Spinning Continuous Fibers for Nanotechnology. *Science* **2004,** *304* (5679), 1917-1919.

7. Huang, Z. M.; Zhang, Y. Z.; Kotaki, M.; Ramakrishna, S., A review on polymer nanofibers by electrospinning and their applications in nanocomposites. *Compos. Sci. Technol.* **2003,** *63* (15), 2223-2253.

8. Meechaisue, C.; Wutticharoenmongkol, P.; Waraput, R.; Huangjing, T.; Ketbumrung, N.; Pavasant, P.; Supaphol, P., Preparation of electrospun silk fibroin fiber mats as bone scaffolds: a preliminary study. *Biomed Mater* **2007,** *2* (3), 181-8.

9. Li, W. J.; Laurencin, C. T.; Caterson, E. J.; Tuan, R. S.; Ko, F. K., Electrospun nanofibrous structure: A novel scaffold for tissue engineering. *J. Biomed. Mater. Res.* **2002,** *60* (4), 613-621.

10. Ignatova, M.; Manolova, N.; Rashkov, I., Novel antibacterial fibers of quaternized chitosan and poly(vinyl pyrrolidone) prepared by electrospinning *Macromolecular Nanotechnology* **2007,** *43* (5), 1112-1122.

11. Sundarrajan, S.; Ramakrishna, S., Fabrication of nanocomposite membranes from nanofibers and nanoparticles for protection against chemical warfare stimulants. *J. Mater. Sci.* **2007,** *42* (20), 8400-8407.

12. Kim, G.; Kim, W., Formation of oriented nanofibers using electrospinning. *Applied Physics Letters* **2006,** *88*, 233101.

13. Greiner, A.; Wendorff, J. H., Electrospinning: A fascinating method for the preparation of ultrathin fibres. *Angew. Chem.-Int. Edit.* **2007,** *46* (30), 5670-5703.

14. Ding, B.; Kim, H. Y.; Lee, S. C.; Shao, C. L.; Lee, D. R.; Park, S. J.; Kwag, G. B.; Choi, K. J., Preparation and characterization of a nanoscale poly(vinyl alcohol) fiber aggregate produced by an electrospinning method. *J. Polym. Sci. Pt. B-Polym. Phys.* **2002,** *40* (13), 1261-1268.

15. Dror, Y.; Salalha, W.; Khalfin, R. L.; Cohen, Y.; Yarin, A. L.; Zussman, E., Carbon Nanotubes Embedded in Oriented Polymer Nanofibers by Electrospinning. *Langmuir* **2003,** *19*, 7012-7020.

16. Jeong, J. S.; Moon, J. S.; Jeon, S. Y.; Park, J. H.; Alegaonkar, P. S.; Yoo, J. B., Mechanical properties of electrospun PVA/MWNTs composite nanofibers. *Thin Solid films* **2007,** *515*, 5136-5141.

17. McCullen, S. D.; Stano, K. L.; Stevens, D. R.; Roberts, W. A.; Monteiro-Riviere, N. A.; Clarke, L. I.; Gorga, R. E., Development, optimization, and characterization of electrospun poly(lactic acid) nanofibers containing multi-walled carbon nanotubes. *Journal of Applied Polymer Science* **2007,** *105* (3), 1168-1678.

18. Naebe, M.; Lin, T.; Tian, W.; Dai, L.; Wang, X., Effects of MWNT nanofillers on structures and properties of PVA electrospun nanofibres. *Nanotechnology* **2007,** *18*, 225605.

19. Sen, R.; Zhao, B.; Perea, D.; Itkis, M. E.; Hu, H.; Love, J.; Bekyarova, E.; Haddon, R. C., Preparation of Single-Walled Carbon Nanotube Reinforced Polystyrene and Polyurethane Nanofibers and Membranes by Electrospinning. *Nano Letters* **2004,** *4* (3), 459-464.

20. Blond, D.; Walshe, W.; Young, K.; Blighe, F. M.; Khan, U.; Almecija, D.; Carpenter, L.; McCauley, J.; Blau, W. J.; Coleman, J. N., Strong, tough, electrospun polymer-nanotube composite membranes with extremely low density. *Adv. Funct. Mater.* **2008,** *18* (17), 2618-2624.

21. Coleman, J. N.; Khan, U.; Blau, W. J.; Gun'ko, Y. K., Small but strong: A review of the mechanical properties of carbon nanotube-polymer composites. *Carbon* **2006,** *44* (9), 1624-1652.

22. Iijima, S., Helical microtubules of graphitic carbon. *Nature* **1991,** *354* (6348), 56-58.

23. Baughman, R. H.; Zakhidov, A. A.; de Heer, W. A., Carbon nanotubes - the route toward applications. *Science* **2002,** *297* (5582), 787-792.

24. Treacy, M. M. J.; Ebbesen, T. W.; Gibson, J. M., Exceptionally high Young's modulus observed for individual carbon nanotubes. *Nature* **1996,** *381*, 678-680.

25. Wong, E. W.; Sheehan, P. E.; Lieber, C. M., Nanobeam Mechanics: Elasticity, strength and toughness of nanorods and nanotubes. *Science* **1997,** *277*, 1971-1975.

26. Lordi, V.; Yao, N., Molecular mechanics of binding in carbon-nanotube-polymer composites. *Journal of Material Research* **2000,** *15* (12), 2770-2779.

27. Amiran, J.; Nicolosi, V.; Bergin, S. D.; Khan, U.; Lyons, P. E.; Coleman, J. N., High quality dispersions of functionalized single walled nanotubes at high concentration. *J. Phys. Chem. C* **2008,** *112* (10), 3519-3524.

28. Coleman, J. N.; Cadek, M.; Ryan, K. P.; Fonseca, A.; Nagy, J. B.; Blau, W. J.; Ferreira, M. S., Reinforcement of polymers with carbon nanotubes. The role of an ordered polymer interfacial region. Experiment and modeling. *Polymer* **2006,** *47*, 8556-8561.

29. Wong, K. K. H.; Zinke-Allmang, M.; Hutter, J. L.; Hrapovic, S.; Luong, J. H. T.; Wan, W., The effect of carbon nanotube aspect ratio and loading on the elastic modulus of electrospun poly(vinyl alcohol)-carbon nanotube hybrid fibers. *Carbon* **2009,** *47* (11), 2571-2578.

30. Kumar, S.; Dang, T. D.; Arnold, F. E.; Bhattacharyya, A. R.; Min, B. G.; Zhang, X.; Vaia, R. A.; Park, C.; Adams, W. W.; Hauge, R. H.; Smalley, R. E.; Ramesh, S.; Willis, P. A., Synthesis, Structure, and Properties of PBO/SWNT Composites. *Macromolecules* **2002,** *35*, 9039-9043.

31. Vigolo, B.; Penicaud, A.; Coulon, C.; Sauder, C.; Pailler, R.; Journet, C.; Bernier, P.; Poulin, P., Macroscopic Fibers and Ribbons of Oriented Carbon Nanotubes. *Science* **2000,** *290* (5495), 1331-1334.

32. Dalton, A. B.; Collins, S.; Razal, J.; Munoz, E.; Ebron, V. H.; Kim, B. G.; Coleman, J. N.; Ferraris, J. P.; Baughman, R. H., Continuous carbon nanotube composite fibers: properties, potential applications, and problems. *Journal of Materials Chemistry* **2004,** *14* (1), 1-3.

33. Walters, D. A.; Ericson, L. M.; Casavant, M. J.; Liu, J.; Colbert, D. T.; Smith, K. A.; Smalley, R. E., Elastic strain of freely suspended single-wall carbon nanotube ropes. *Applied Physics Letters* **1999,** *74* (25), 3803-3805.

34. Miaudet, P.; Badaire, S.; Maugey, M.; Derre, A.; Pichot, V.; Launois, P.; Poulin, P.; Zakri, C., Hot-drawing of single and multiwall carbon nanotube fibers for high toughness and alignment. *Nano Letters* **2005,** *5* (11), 2212-2215.

35. Wang, Z.; Ciselli, P.; Peijs, T., The extraordinary reinforcing efficiency of single-walled carbon nanotubes in oriented poly(vinyl alcohol) tapes. *Nanotechnology* **2007,** *18* (45).

36. Minus, M. L.; Chae, H. G.; Kumar, S., Single wall carbon nanotube templated oriented crystallization of poly(vinyl alcohol). *Polymer* **2006,** *47* (11), 3705-3710.

37. Coleman, J. N.; Cadek, M.; Blake, R.; Nicolosi, V.; Ryan, K. P.; Belton, C.; Fonseca, A.; Nagy, J. B.; Gun'ko, Y. K.; Blau, W. J., High-performance nanotube-reinforced plastics: Understanding the mechanism of strength increase. *Adv. Funct. Mater.* **2004,** *14* (8), 791-798.

38. Vollrath, F.; Knight, D. P., Liquid crystalline spinning of spider silk. *Nature* **2001,** *410* (6828), 541-548.

39. Chae, H. G.; Kumar, S., Rigid-rod polymeric fibers. *Journal of Applied Polymer Science* **2006,** *100* (1), 791-802.

Conclusion

In this thesis we have studied the mechanical properties of germanium nanowires and polymer composite nanofibres. We have used an AFM-based technique previously developed in our group where nanowires lying across trenches and pinned down on the edges are laterally loaded with an AFM tip. In the case of germanium nanowires, using the data provided for nanowires of diameters above 40 nm, we developed a generalised model to extract the ultimate strength of the wires. We subsequently established the Young modulus and ultimate strength of these wires to be 112 GPa and 15 GPa respectively. The latter was the highest ever recorded strength for a semiconductor nanowire and was very close to the theoretical limit of 17 GPa. The model developed here can be used for any continuous beam in a double clamped configuration. These results were published in Nano Letters, vol 6, page 2964. We also used this model for smaller germanium nanowires, with diameters from 10 to 40 nm. The set of data acquired for these nanowires resulted in a large amount of scatter, especially for the smallest nanowires. We attributed this effect to either the presence of an oxide layer or the atomic structure of the nanowires. TEM investigation was carried out on a statistically relevant number of nanowires and a significant number of them were found to show a large density of defects. To tackle this problem, we carried out mechanical measurements on TEM grids, first on holey carbon grids, then on silicon nitride grids as those provided rigidity. These measurements were successful on large nanowires but could not be carried out on smaller ones as these would curve around the holes to avoid lying across them. From this observation we are still developing experiments to measure the adhesion of the nanowires on the surface in order to link it to their curvature and ultimately their modulus.

The investigation of the mechanical properties of polymer composite nanofibres was carried out on electrospun poly-vinyl-alcohol-carbon nanotube composite fibres. From the data acquired using the AFM-based technique we found that these nanofibres exhibited brittle fracture without any sign of plasticity. We then developed an elastic model to establish lower bounds for both modulus and strength of the fibres depending on their carbon nanotube concentration. It was found that 0.05 vol% of carbon

nanotube resulted in the highest values for modulus and strength, 85 GPa and 2.6 GPa respectively. In addition, strain at break and toughness were extracted and optimised fibres break at 4 % strain having absorbed 27 MJ/m^3. These results were published in Carbon, vol 47, page 2253.

Preliminary work was also carried out in the determination of electro-mechanical properties of germanium nanowires. Substrates were fabricated using UV lithography and EBL. These were made of 20 interdigitated electrodes separated by 400 nm deep trenches. Nanowires were contacted to the electrodes with electron beam induced deposition of tungsten. A nano-pulley system was introduced to overcome the problems stemming from bending the nanowire while passing current through. The remaining work stemming from this thesis will be carried out by another member of our group, Eoin McCarthy.

Publications

- Lien T. Ngo, Dorothée Almecija, John E. Sader, Brian Daly, Nikolay Petkov, Justin D. Holmes, Donats Erts, John J. Boland, *Nanoletters* **2006**, 6, (12), 2964
- Xueyan Wu, Jaideep Kulkarni, Gillian Collins, Nikolay Petkov, Dorothée Almecija, John J. Boland, Donats Erts, Justin D. Holmes, *Chemistry of Materials*, **2008**, 20, 5954
- Dorothée Almecija, David Blond, John E. Sader, Jonathan N. Coleman and John J. Boland, *Carbon*, **2009**, 47, 2253

Appendices

Appendix A. TEM sample preparation procedure

The SEM/FIB is a FEI xP Dual Beam Workstation. The micro-manipulator is from Kleindiek Nanotechnik. The optical microscope is a Zeiss Axio. All dimensions are given in the x-y-z format.

The nanowire solution is sonicated for 20 seconds and a few µL are drop cast on the surface. The remaining solvent is blown away using nitrogen. The density of wires on the surface can be checked on the optical microscope, as a fairly high density is required to get the highest throughput.

After locating a long and smooth wire, Platinum is deposited with the electron beam, perpendicularly to the wire direction on the wafer, as shown on Figure A1A. This electron beam induced deposition (EBID) is carried out with the 1000µm aperture, patterning a rectangle of 0.5 x 3 x 1 μm^3 for one minute with the pt.mtr material file. This step is designed to protect the wire from being damaged by the gallium ions during milling and during the next Pt deposition. While the EBID was carried out with the stage at 0°, the ion beam induced deposition (IBID) is performed at 52°, perpendicular to the ion beam. Using 100pA ion current, a rectangle of 1 x 15 x 1 μm^3 of Pt is patterned for 2 min. The IBID deposition is significantly faster than the EBID one and provides a homogenous layer of Pt, about a 1µm high on top of the wire.

Two areas are milled out on either side of the Pt line using a current of 3nA and the material file si.mtr. They are set to be 6µm long, 15µm wide and about 6µm deep and milling one typically lasts 10min. Each side is milled following a staircase shape, reducing the milling time without preventing the rest of the procedure. The current used is quite high, which makes the bulk milling faster but also gives rougher edges, especially around the Pt and the feature of interest. In addition, it has been noted that higher currents seem to drift faster than smaller ones, hence jeopardizing the cross-section. It is then advisable to set this milling quite a distance away from the Pt and then mill a smaller staircase at 1nA, closer to the Pt. The lamella left in the centre (and containing the

nanowire cross-section) should be at that point about 1μm thick, as pictured in Figure A1B.

In order to release it from the silicon bulk and thus facilitate its lift out, the lamella needs to be undercut. Whereas all the previous steps were done at 52° tilt (i.e. perpendicular to the ion beam direction), this particular one is done at 7° tilt so that the ion beam is almost parallel to the staircase, providing the best angle to optimise milling time while milling as deep into the pit as possible. However, in this configuration, the ion beam will scan the side of the lamella, i.e. the feature of interest and might damage it. Hence a small current is required. We used 100pA. Rectangles of 0.3 μm large and 1 μm deep were patterned. The length of the 2 side cuts is actually quite important. It is best to mill as close from the surface as possible as it will facilitate the last step. Typically, the side cuts take 90sec while the bottom cut lasts 4min. It should be noted that the previous step is actually essential for the undercutting process. If this first thinning of the lamella doesn't occur, it is very likely that the bottom of the lamella would be several microns wide, making it very hard to undercut the bottom of the lamella, thus preventing its release. Figure A1C shows an electron beam image taken to verify the beam went through the thickness of the lamella.

The stage is tilted back to 52°, to be perpendicular to the ion beam. The ion current is set at 50pA. When possible, an ion beam voltage of 12kV should be used for this step. However our tool does not function at this voltage, so we have to use the 30kV beam voltage. The software provides a 'cleaning' procedure where, the ion beam is scanned in lines and moved inwards in half a beam diameter steps, providing thin parallel side walls, as shown on Figure A1D. For time saving purposes, we typically only fine mill the area around the feature of interest. Electron transparency is targeted during this milling. It is then of the utmost importance to be extra careful during this step. The slightest drift of the beam can damage the entire work done so far. When the milling was started, electron beam images were taken every half minute or so, to check that the beam did not damage the feature of interest. Milling should be stopped when the area around the feature of interest is getting brighter on the electron beam image, sign of electron transparency. Once the lamella is cleaned, it should only be less than 100nm thick, as

seen on Figure A1E. However, electron reflection from the lamella walls makes it hard to appreciate its exact thickness. Typically this step takes around 10 minutes.

Before lifting-out the lamella, the latter needs to be released from the bulk Si. This is done by milling the side parts of the lamella, which are still connected to the bulk. In order to facilitate lift off, it is very advisable to try to get the lamella to stick out from the pit. To do so, the lamella is released on one side by a short mill (10sec). The other side is then slowly milled away using several line mills of less than a second. This creates a tension on the part still attached to the Si and makes the lamella stick up, as Figure A1F shows. After this step, the sample can be taken out of the SEM chamber and brought to the optical microscope and micro-manipulator.

After setting up the micro-manipulator beside the microscope, a glass needle is fabricated from a glass cylinder (1.2x90mm) using the Narishige Single Stage Glass Microelectrode Puller PP-830 at 65.8°C. The micro-manipulator allows controlled motion in X, Y and Z directions independently. It can be used at different gears, allowing perfect control over short and long distances (from hundreds of nanometres to centimetres).

The sample is securely positioned on the microscope stage and a TEM grid is placed beside it. For best success rates, the lamella should be positioned parallel in the XY plane to the incoming needle. Adhesion between the needle and the lamella is done though Van der Waals forces. The needle is centred on the XY plane under the microscope beam. Using the 50x objective, focus is made on the lamella and the needle is slowly brought down into focus, i.e. near the surface. Once both needle and lamella are in focus, the needle is moved in a sideways manner to brush over the surface, then lowered, then swept across the surface, until the lamella attaches itself to the needle. This typically takes a few minutes. Care has to be taken not to push the lamella into the pit, as it would make its recovery a more difficult task. Once the lamella is on the needle, it is unlikely it will drop back on the surface. The needle can then be moved upwards to a safe distance from the surface and the microscope stage is moved to have the TEM grid below the beam, hence below the needle. The latter is then slowly brought down

towards the grid until close enough that the lamella usually jumps from the needle to the grid, as shown on Figure A1G.

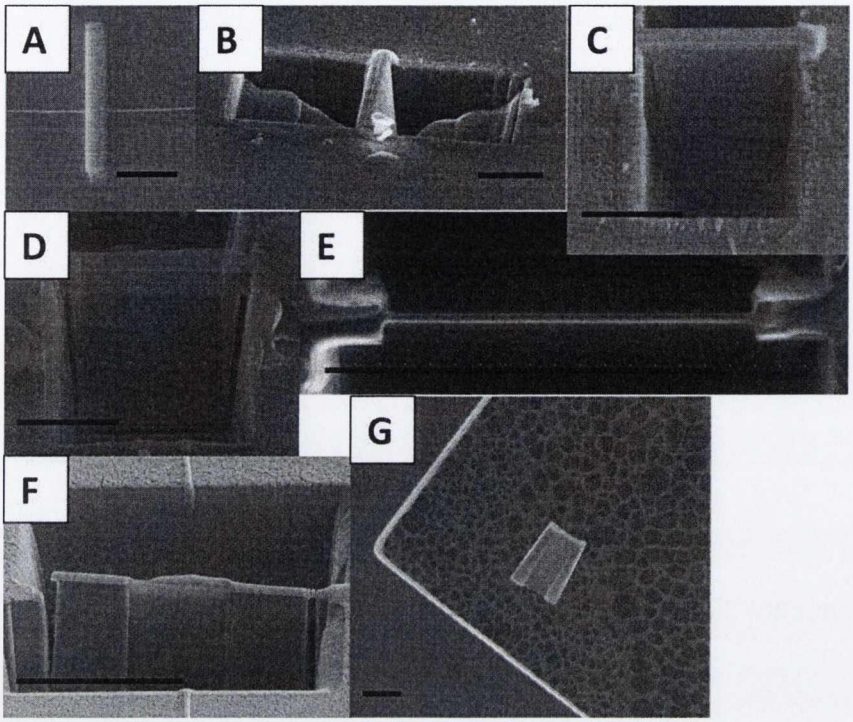


***Figure A1**. SEM images showing the sequence of events to obtain a TEM lamella containing a NW cross section.*

Appendix B. Young's modulus determination from generalised model

Young's modulus is obtained normally from a measurement of the beam displacement as a function of the applied load. The resulting curve is then fit to the following well-known equation

$$F_{center} = \frac{192\,E\,I}{L^3}\Delta z_{center}, \qquad (1)$$

where F_{center} is the load applied to the center of the beam, Δz_{center} is the resulting displacement of the beam at the load point, E is the Young's modulus of the beam, I is areal moment of inertia, and L is the beam length.

Importantly, this equation predicts a linear relationship between the applied load and the resulting displacement and thus requires that measurements also exhibit this

property. However, as the beam is displaced, an in-plane tensile force is inherently induced due to the stretching of the beam. This force affects the total stress experienced by the beam, leading to an enhancement of its rigidity. In this section, we present a simple closed form solution to this problem that is valid for any beam displacement, enabling the determination of the Young's modulus, irrespective of the applied load.

To begin we note that the governing beam equation, which includes the effects of in-plane forces, is

$$E I \frac{d^4 w}{dx^4} - T \frac{d^2 w}{dx^2} = F_{center} \delta(x - \tfrac{L}{2}) \quad , \qquad (2)$$

where w is the deflection of the beam, x is the spatial coordinate along the beam length, T is the tension along the beam, and δ is the Dirac delta function. Note that $\Delta z_{center} = w(L/2)$. The tension T is determined from the strain along the axis of the beam, and is given by

$$T = \frac{E A}{2L} \int_0^L \left(\frac{dw}{dx} \right)^2 dx \quad , \qquad (3)$$

Equations (2) and (3) are to be solved subject to the usual clamped boundary conditions at both ends of the beam, i.e.,

$$w = \frac{dw}{dx} = 0 \quad \text{at} \quad x = 0 \text{ and } L \, . \qquad (4)$$

Solving Eqs. (2) – (4) gives the required solution

$$F_{center} = \frac{192 E I}{L^3} f(\alpha) \Delta z_{center} \quad , \qquad (5)$$

where

$$f(\alpha)=\frac{\alpha}{48-\dfrac{192\tanh(\sqrt{\alpha}/4)}{\sqrt{\alpha}}}\quad, \qquad (6)$$

where α is related to the maximum deflection Δz_{center} by the following transcendental equation

$$\frac{\alpha\cosh^2(\sqrt{\alpha}/4)}{2+\cosh(\sqrt{\alpha}/2)-6\dfrac{\sinh(\sqrt{\alpha}/2)}{\sqrt{\alpha}}}\left(1-4\frac{\tanh(\sqrt{\alpha}/4)}{\sqrt{\alpha}}\right)^2=\Delta z_{center}^2\left(\frac{A}{I}\right) \quad . \qquad (7)$$

We note that $f(\alpha)\geq 1$, so that inclusion of the tensile force increases the effective rigidity of the beam. Also, α is directly connected to the tension in the rod via the relation

$$\alpha=\frac{TL^2}{EI}$$

and is the ratio of axial stresses due to extension and bending.

While Eqs. (5) – (7) present an exact analytical solution, it is complex in nature, requiring the numerical solution of a transcendental equation for its implementation. To overcome this limitation, we note that the solution to Eq. (7) possesses the following asymptotic solutions

$$\alpha=\begin{cases}\dfrac{12}{5}\varepsilon-\dfrac{3}{875}\varepsilon^2 & , \quad \varepsilon\to 0\\[2ex] 2\varepsilon & , \quad \varepsilon\to\infty\end{cases} \quad , \qquad (8)$$

where

$$\varepsilon = \Delta z_{center}^2 \left(\frac{A}{I} \right) \quad . \qquad (9)$$

An approximate and explicit expression for α is then obtained by constructing a Padé approximant using Eq (8), i.e.,

$$\alpha = \frac{6\varepsilon(140 + \varepsilon)}{350 + 3\varepsilon} \quad , \qquad (10)$$

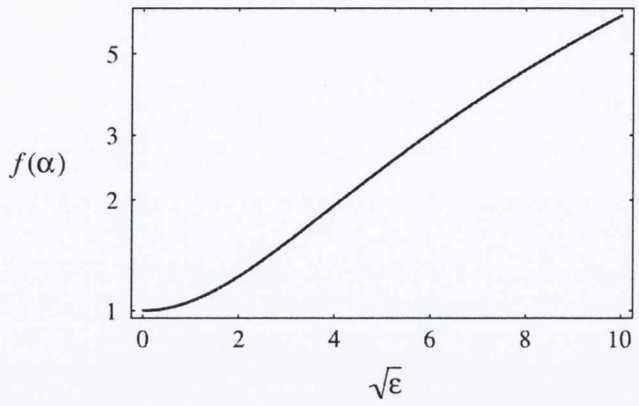
which exhibits a maximum error of only 2.1% over the entire range of ε. Equations (5), (6) and (10) are the results we seek, and enable the applied force to be determined for any beam displacement.

Equation (9) indicates that the solution, Eq. (1), is valid provided the maximum displacement Δz_{center} is less than the radius of the beam. As Δz_{center} is increased to a value larger than the beam radius, the solution becomes progressively more nonlinear with respect to the displacement, leading finally to a cubic dependence on Δz_{center}. Thus, an approximate solution can be obtained by superimposing the small and large deflection limits, namely

$$F_{center} = \frac{192\,E\,I}{L^3} \Delta z_{center} \left(1 + \frac{A}{24\,I} \Delta z_{center}^2 \right) \quad , \qquad (11)$$

a result which exhibits a maximum error of 18%.

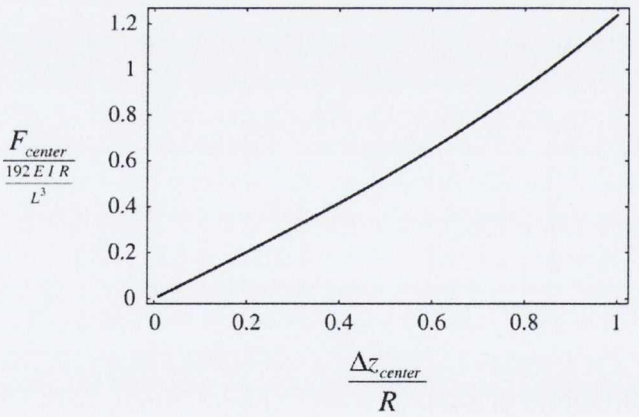
We now show a plot of the rigidity enhancement function $f(\alpha)$ as a function of $\sqrt{\varepsilon}$ (which is directly proportional to the maximum displacement, see Eq. (9)),



For a circular cylinder

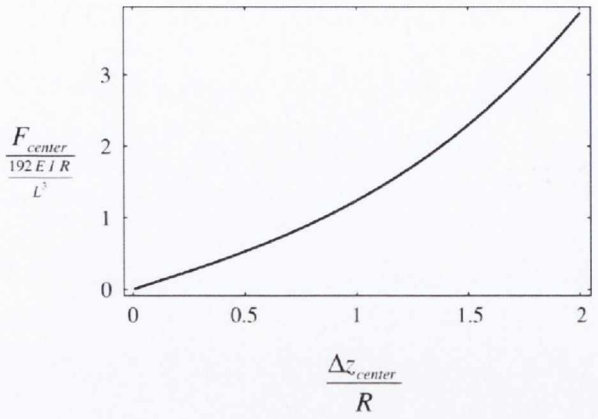
$$I=\frac{\pi R^4}{4} \quad , \quad A=\pi R^2 \quad , \quad \varepsilon=\left(\frac{2\Delta z_{center}}{R}\right)^2 \quad . \tag{12}$$

Below we illustrate the effect of this nonlinearity on the measured force curves of circular cylinders. First, we consider the case where the maximum deflection is one radius

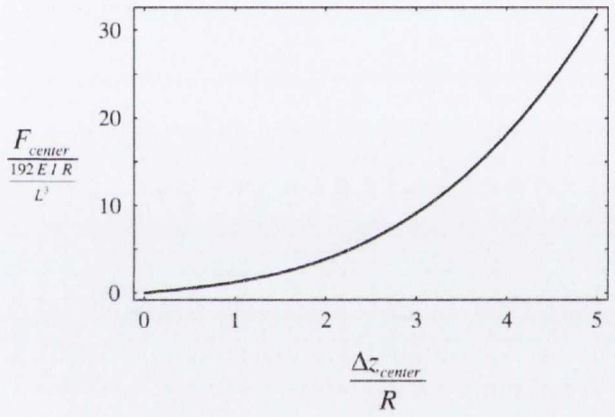


From these results, it is clear that for deflections smaller than one radius, the standard theory accurately predicts the behaviour of the rod. Note that the results have been normalised so that a slope of unity corresponds to the standard theory.

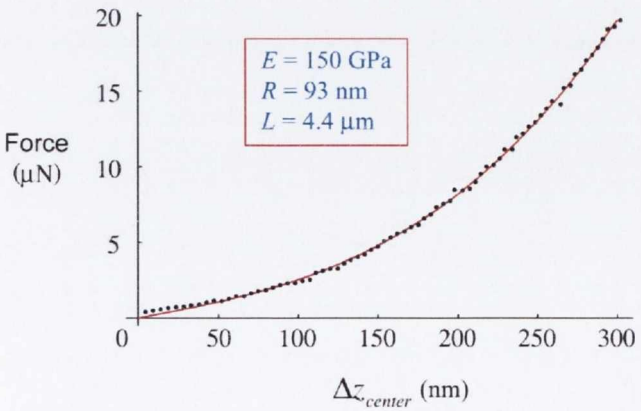
Next, we show the force curve for a slighter larger extension up to twice the radius of the rod.



As can be seen, the curve becomes increasingly nonlinear as the deflection is increased passed one radius. For larger deflection, the nonlinearity grows leading to an ultimate cubic dependence on the deflection

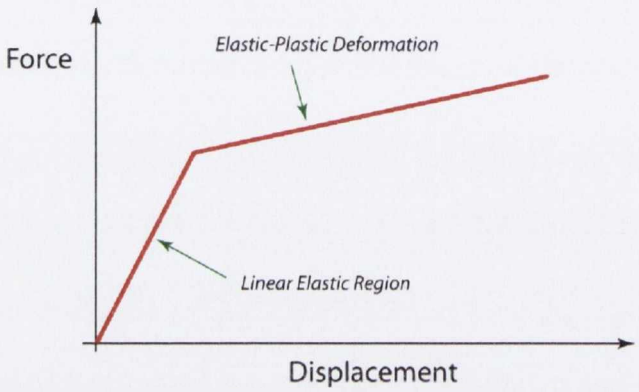


These calculations are to be compared against the measured force curves taken on silicon nanowires:

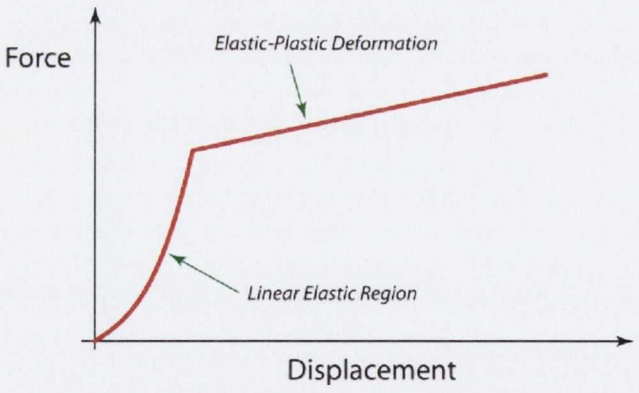


Note that the only adjustable parameter in the fit was the Young's modulus *E*. The value obtained is in line with expected bulk material values. Thus, nonlinear force curves can be used to determine the Young's modulus of nanowires, even though the Young's modulus is inherently a linear elastic property. Note that the nonlinearity observed is due to a geometrically induced nonlinearity within the framework of linear elasticity.

The classical load-displacement curve showing transition from elastic to plastic behavior is given by



whereas accounting for this geometric nonlinearity gives the more realistic picture



Thus even though the material is behaving as a linear elastic solid, the load-displacement curve is inherently nonlinear in the linear elastic regime. The theory presented above can be used to extract the linear material constants from this nonlinear curve.

IMPORTANT:

(1) Beam theory is used to analyse these measurements. This inherently assumes that the stresses are uniaxial and hence that the beam is much longer than it is wide. This restriction must be reflected in the experimental set up. Failure to comply can result in complex stress distributions in the rod, leading to failure of the theoretical framework.

(2) The induced in-plane tensile stress also has obvious implications to the determination of the maximum tensile stress, the standard formula for which only assumes that bending, and not stretching, is occurring.

(3) To determine maximum tensile strength, such tensile stretching forces must be included.

Appendix C. Ongoing work - Investigation of the electromechanical properties of germanium nanowires

AC.1 Motivation

Nanowires are expected to have great potential for applications in sensors, actuators and nano electromechanical systems (NEMS)[1-3]. Most NEMS are operated in their resonant modes and due to their small size and high surface area they exhibit extremely high fundamental resonance frequency[6]. The quality factor, Q, of these systems is usually in the range of 10^3 to 10^5, significantly higher than MEMS. NEMS have been actively explored because of their applications as ultra high resolution mass sensors[7], and the detection[8] of classical and quantum mechanical forces[9]. Nanowires have been the subject of various studies including switches[10-11] and high frequency resonators[12-13]. To fabricate these NEMS structures, top down techniques have been the most employed[14]. However with the advancement in the synthesis of high quality nanowires, bottom up approaches are becoming more popular. The latter give access to crystalline, size controllable nanowires with smooth surfaces. The main drawback of this method is the need to position the nanowires to obtain good electrical contact and to allow space for mechanical movement. Nevertheless progress in lithography and etching should overcome this hurdle and open up new designs for NEMS.

There has been a significant number of reports on carbon nanotubes and Si NWs based NEMS[11, 13, 15-16] but very few concerning Ge NWs: except for Smith et al[17] and Andzane et al[18], and the continuing work from Ziegler et al[19]. We have discussed the former in

Chapter 3 in the context of mechanical properties of Ge NWs. By vibrating Ge NWs pinned to a TEM grid and in close proximity to a tungsten probe to which an AC voltage was applied, the authors studied the frequency response of the resonators. They calculated quality factor values of 100 to 600, much lower than for Si NWs resonators[13] where Q was found to be 13,100 for 80 nm pristine Si NWs. In addition they found Q to decrease with decreasing diameters, as shown on Figure C1. They attributed this rise in energy dissipation at smaller diameters to surface losses which increase with the surface area to volume ratio. If energy is dissipated by the surface, a good understanding of surface chemistry and structure is critical to the study of Ge NWs resonators. Such a

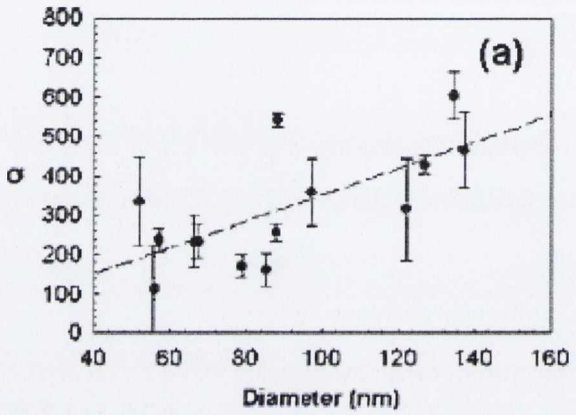


Figure C1. *Quality factor Q versus diameter for Ge NWs*[17]

trend could be a problem for further development of nanowire-based resonators and more data needs to be acquired for other NWs systems as well as for Ge.

Andzane et al studied Ge NWs in a two-terminal NEMS with ON/OFF regimes[18] by carefully balancing adhesion, electrostatic and elastic forces. They used a TEM-SPM based technique already developed by Ziegler et al in 2004[19]. A Ge NWs is pinned at the end of a gold tip and in close proximity to an opposite electrode, as displayed in Figure C2. The distance between the two electrodes is carefully chosen to overcome

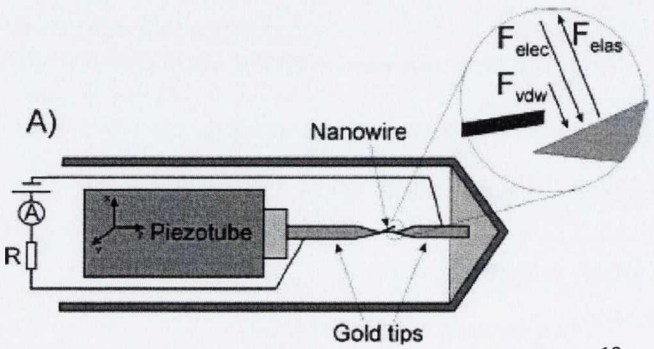


Figure C2. *Set-up for TEM-SPM study of Ge NEMS*[18]

electrostatic forces (Van der Waals forces) that would cause the wire to snap onto the opposite electrode. Upon the application of a voltage between the two electrodes, the NW is forced to deform and move towards the opposite electrode. When a sufficient voltage is applied, the attractive force between the tip and the sample exceeds the spring constant of the NW and jump-to-contact occurs. When the voltage was reduced, the NW remained in contact with the electrode at a lower voltage than the jump-to-contact voltage due to adhesion forces. The authors also found that adhesion forces and elastic forces were almost similar for large NWs (diameter larger than 50 nm). However for smaller diameter NWs, the adhesion force was estimated at an order of magnitude higher than the elastic force. This was attributed to the different thickness of oxide on facets of the NWs, hence decreasing the contact area with the electrode.

Ge NWs have proven to be successful resonators and can be integrated into functional devices. Another interesting use of nanowires is band gap engineering[20] especially for photonic applications. Band gap engineering has been demonstrated for semiconductor alloys[21] such as InGaAs[22], GaAlAs[23] or ZnO based materials[24-25], carbon nanotubes[26] and polymers[27] but has not been reported for Ge NWs to the best of our knowledge.

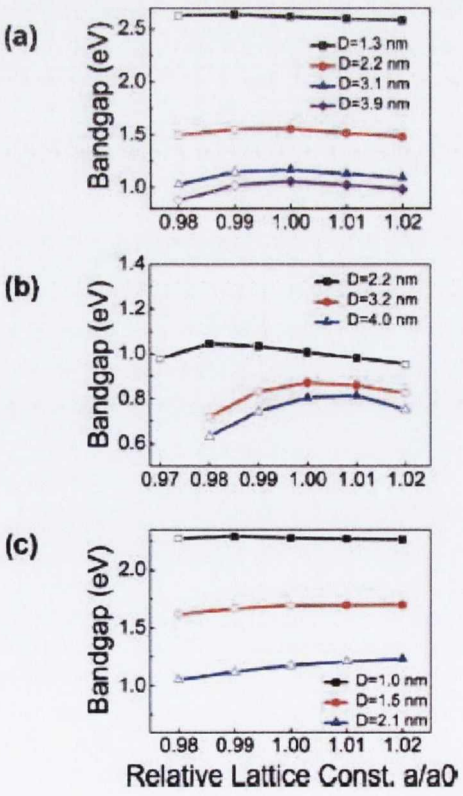


Figure C3. *Band gap variation as a function of strain for (a) [100], (b) [110] and (c) [111] orientations. Filled and unfilled symbols represents direct and indirect band gap*[4].

However, Hong et al reported on strain driven band gap modulation of Si NWs[4] in 2008. The objective of that study was to understand how to obtain a direct band gap in Si NWs. Using DFT they studied the effect of uniaxial strain on Si NWs depending on their crystal orientation and diameters. Figure C3 shows the variation of band gap for different crystal orientation and diameters. This study is in good agreement with expectation that smaller diameter wires have larger band gap due to quantum confinement effects[28]. It was found that tensile strain enhances direct band gap characteristic for the directions [100] and [111]. For the direction [110] both tensile and compressive stresses result in an indirect band gap. The strain dependence on crystal orientation is attributed to the different shapes of wave functions of the valence band for the different crystal orientations. In addition the authors observed that smaller nanowires with larger quantum confinement had a tendency to exhibit a direct band gap.

Si and Ge have similar crystal structures and it is expected that Ge band gap could be modulated through strain. This has never been demonstrated on a nanowire but Fischetti et al reported on the band structure in strained Si and Ge in 1996[5]. In the case of Ge, the electron and hole mobility variation with strain in the [001] direction is

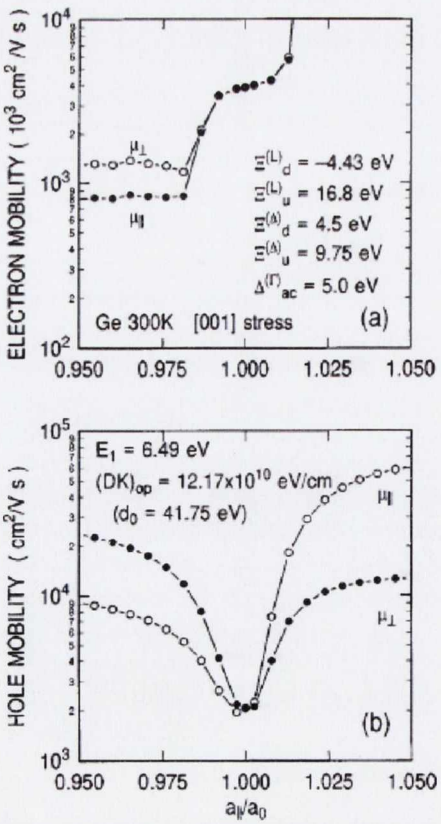


Figure C4. *Electron and hole mobility variation for Ge under strain in [001] direction[5].*

displayed on Figure C4. Hole mobility greatly increases both under tension and compression although the highest increase is for the in-plane mobility under tension. The electron mobility exhibits a dramatic increase under tension and a decrease under compression followed by a plateau at around a third of the bulk value. We note that these values were calculated for bulk strained Ge. The electron and hole mobility behaviour for Ge NWs has not yet been calculated or demonstrated.

For this work we propose to apply tension to Ge NWs while passing current in them. Our objective is to study the change in resistivity as a function of the strain applied and the diameter of the nanowires. We will use our AFM-based technique to locally strain the nanowires. We will comment on the limitations of the first design and we will detail the fabrication of a pulley system to apply uniaxial strain to the NWs. We expect a larger effect for smaller nanowires, which we have demonstrated in Chapter 4 can be deformed significantly before fracture. The variation in resistivity as a function of strain can provide us with important insight in the modulation of the band gap for Ge NWs. This work is still in progress and we will only mention the preliminary results obtained.

AC.2 Experimental approach

To perform this study we need to fabricate trenched substrates where each electrode is conductive and linked to an individual accessible pad. Figure C5 displays a schematic of

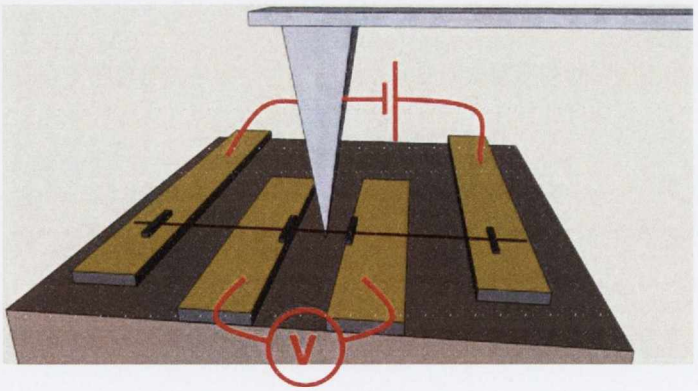


Figure C5. *Schematic of electromechanical set-up*

the design. A Ge NWs is positioned across four electrodes by drop casting the solution on the substrate. The NW is subsequently pinned down by EBID W on three electrodes (grey strips on schematics). A current source is applied on the outer electrodes and the voltage across the inner electrodes voltage is monitored as the AFM tip laterally loads

the NW. While this system is quite simple in its design, its fabrication required several carefully carried out steps which we will detail now.

The substrate was fabricated using electron beam and UV lithography steps. Both these processes are similar in concept and the main steps of UV lithography are detailed in Figure C6. First, the wafer has to be cleaned. Silicon wafers (ordered from Chris Baker), 500 μm thick, covered with 1 μm of SiO_2 were cleaved into small rectangular pieces of about 10x10 mm with a diamond scribe. After blowing away the dust residue with an N_2 gun, the pieces were placedinto acetone and sonicated for 5 min. Afterwards, they were put into isopropanol (IPA) and sonicated another 2 minutes. Then the pieces were

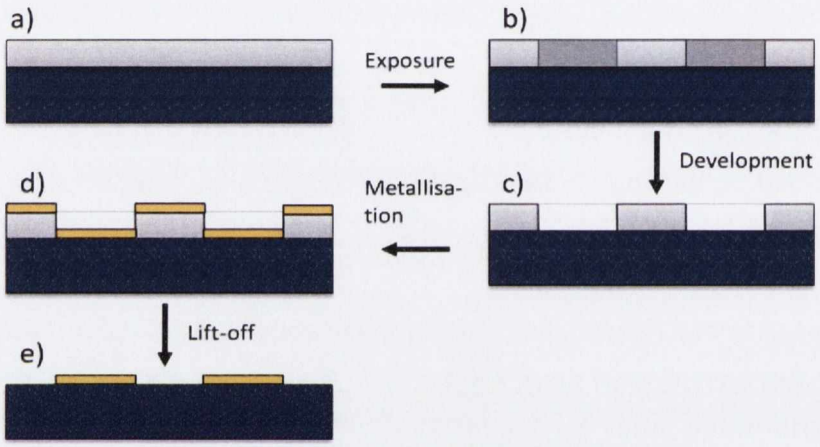


Figure C6. *Schematics of lithography process*

thoroughly dried with an N_2 gun prior to spinning. Secondly, resist was spun on the wafer. Prior to spinning any water residue on the wafer was evaporated by baking the wafer for 10 min at 110 C. On the spinner machine, the substrate was placed on top of the vacuum chuck and the lid was closed. A program was chosen to spin the resist at the selected speed. A typical procedure starts with 500rpm for 5 sec, then 5000rpm for 40 sec. A few mL of positive photoresist S1813 (purchased from Rohm and Haas Electronic Materials LLC) was drop cast onto the substrate and the spinning was started. At the end of the spinning, the substrate was placed on a hot plate to bake the resist at 115 C for 75 sec. At the end of this step, the substrate is covered by a homogenous layer of resist, as seen on Figure 8a. The resist is then exposed to the beam. Using the Karl SUSS-MJB 3 UV400 Mask Aligner, the sample was exposed for 3.1 sec with UV light (405nm h-line 23mW/cm^2) under hard contact. During this step, the parts of the resist that are not shadowed by the mask are cross-linked by the UV light. Choosing the exposure time is extremely important. Under-exposed samples have a thin layer of resist left over on the

surface which will be detrimental to the rest of the process. Over-exposure would change the dimensions of the features on the surface. After exposure, the sample was placed into the developer, MF319 (purchased from Micro resist Technology) for 90 sec. The sample was then dried out thoroughly under a N_2 gun. It is important to check the quality of the development as it is directly linked to the quality of the exposure. By looking at the substrate under an optical microscope, one can insure the pattern from the mask has successfully been 'printed' onto the resist as shown on Figure 8b. For most samples metal was evaporated on the surface with the Temescal evaporator. An adhesion layer of titanium was first evaporated to a thickness of 5 nm followed by a thermal evaporation of 50 nm of palladium. In some cases the substrate was then transferred to a sputtering machine (Cressington). The sputtering machine consists of a metal target through which a plasma is created in an Ar atmosphere (pressure around 0.02mbar) with a current of 80 mA. The metal atoms are then ejected from the target onto the substrate. A Pd target was used to metallise our sample. Typically, 50 nm of Pd were deposited in about 3 min. The sample was placed in an acetone bath for at least 15 minutes. The leftover resist should start lifting-off as soon as it is in contact with the acetone. Leaving the sample in acetone for longer ensures the acetone can dissolve as much of the resist as possible, even in between small features. Gentle sonication is usually carried out after 15 minutes, for 2 sec. The sample is then placed into a flat crystallizing dish filled with IPA, making sure the acetone doesn't dry out and the features are closely looked at under a light microscope. If the lift-off is not complete at this point, the sample can be put back into acetone and sonicated for another few seconds. Once lift-off is complete, the sample is rinsed with IPA, DI H_2O and dried with N_2 gun. At the end the pattern on the mask is 'printed' on the sample and covered in metal.

Any one of these steps can damage the sample sometimes irreversibly. We have discussed the importance of exposure time but metallisation and lift off are just as important. If during evaporation or sputtering, the temperature in the chamber gets too high, the resist will be over-baked on the side and then cannot be removed with acetone, which is the common case of rabbit ears. In order to prevent over-baking of the resist, evaporation is preferred over sputtering. The chamber being much larger, the temperature does not rise above 40 C, hence does not damage the resist. In addition the

ratio of thickness of metal over thickness of resist is critical and is usually set to one third. These parameters all have a significant influence on the lift-off procedure and a careful determination of resist thickness, exposure time and evaporation procedure insures the highest quality of lithography.

For our specific purposes, the process to obtain a substrate similar to Figure C5 requires 2 steps. The first step is a UV lithography step using the mask displayed in Figure C7

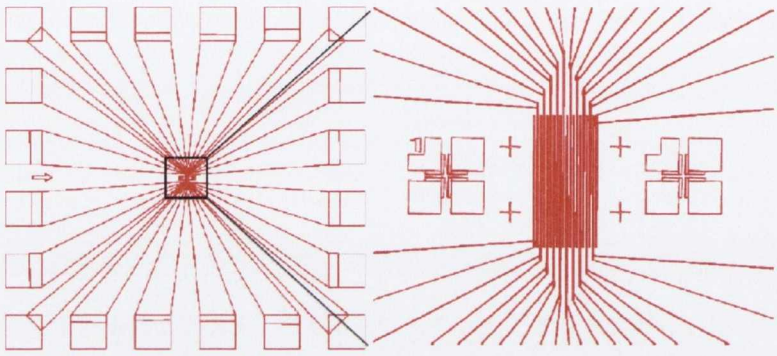


Figure C7. *Design of mask for UV lithography*

which contained 20 electrodes linked to 20 pads on a 10 mm^2 area. The centre electrodes were 200 µm long, 2 µm wide and separated by a 2 µm gap. Alignment marks were added to this mask for the second step of this fabrication. The sample was metallised with 5 nm Ti and 50 nm Pd. The second step is an electron beam lithography (EBL) step to design the trenches between the electrodes. Using the alignment marks designed beside the central electrodes displayed in the zoom-in picture of Figure 69, the sample was aligned so that an array of electrodes similar to the central part of the previous mask were exposed in between the metal lines. While the width between electrodes is 2 µm, this EBL step only expose 1.2 µm of this area using a dose of 110 $\mu A.cm^{-2}$. The reason for that is due to the next step: hydrofluoric (HF) acid etch. After

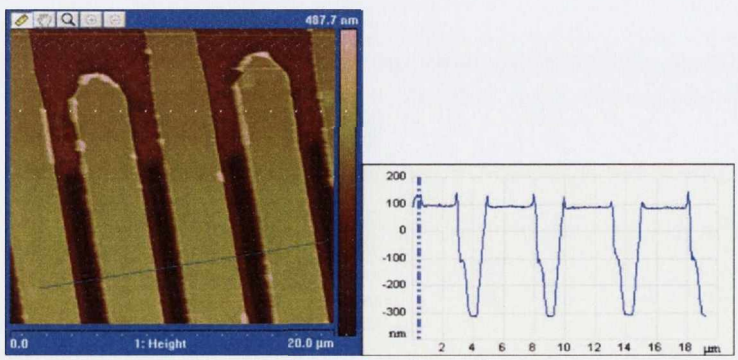


Figure C8. *AFM micrograph of substrate after all processing and cross section*

development, revealing SiO_2 surface between the electrodes, the sample is placed in HF buffer bath (etch rate 100 nm/min) for 4 min. HF etching is isotropic, meaning that SiO_2 will be etched towards the electrodes also. By exposing 1 μm and leaving the etching to be carried out for 4 min, we end up with a 2 μm trench, 400 nm deep between the electrodes. Figure C8 is an AFM micrograph of the central pattern and the trace of a cross section of the playground showing the depth of the trenches. From the cross section trace we can see that the electrodes are not perfectly flat and some rabbit ears are still present However these are only 50 nm high are not an issue for us because the tungsten deposition will weigh the NW down and enhance contact with the electrodes. Germanium nanowires were subsequently drop cast on the substrate. Some fell on the central electrodes as displayed in Figure C9 and were contacted to the electrodes using EBID W. Unfortunately, due to a large amount of dirt in the Ge NWs dispersion, this

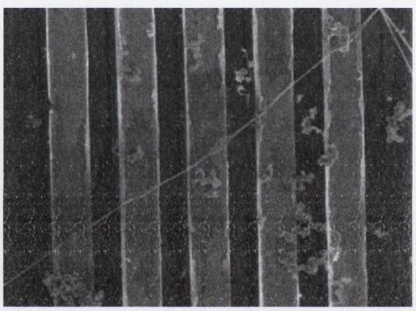


Figure C9. *SEM image of a Ge NW pinned by EBID W over 5 electrodes*

particular sample was not contacted successfully.

This design is a first approach that we use to test our set-up by checking wiring and metallisation work. However it is important to note that this design is not a solution for the study of electromechanical properties of nanowires. The voltage drop at the centre electrodes will be monitored as a function of the deformation applied by the AFM tip. This deformation is composed of bending and stretching and it is expected that tension and compression of the wire while bending will cancel each other, leading to no noticeable effects on the first order. We have then designed a pulley system, displayed in Figure C10, where the nanowire is subject to uniaxial tension. The main difference between this design and the one from Figure C5 is that the NW lying on the third electrode is not contacted by EBID W but is slid against a metal pillar by the AFM tip pulling on the NW along the next trench. This results in an uniaxial strain on the NW between the central electrodes. We can relate the amount of uniaxial strain in the NW

to the force applied to the next NW section, which we know from the laser deflection on the AFM cantilever. The fabrication of this substrate is similar to the previous one. An extra EBL step is added after metallisation of the UV lithographically pattern. Using the alignment marks on the UV mask, pillars are defined on the central electrodes. These are made of Pd, 300 nm wide, 50 nm high and periodically located on the electrodes with a separation of 10 μm.

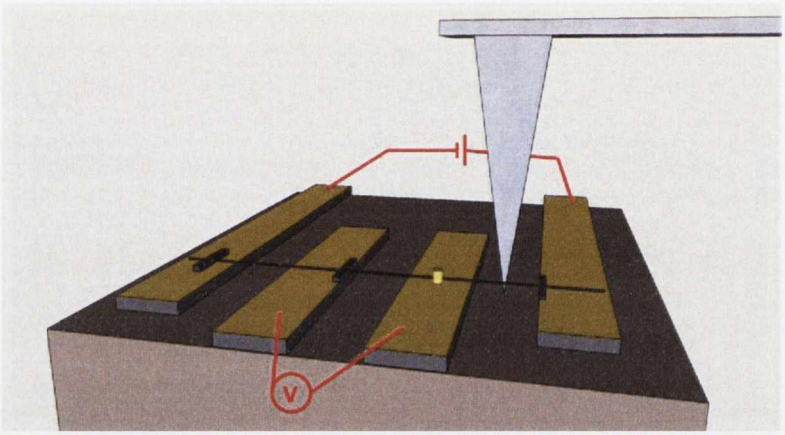


Figure C10. *Schematics of pulley system for the investigation of the electromechanical properties of nanowires*

In order to be able to locate a NW beside a pillar two approaches are being investigated. The first technique is similar to the one developed by Lee et al[29] and involves plucking a NW from the wafer where they were grown and placing it beside a pillar with a micro-manipulator. The other approach involves drop casting NWs over the trenches and sliding one beside the pillar. The second approach might not be possible if the adhesion of the NW on the electrode surface is too large. We have not been able to test this issue yet as we need the lift-off to work perfectly as the smallest rabbit ear would be detrimental to that experiment. We are still actively working to solve this issue.

Conclusion

We have demonstrated the first steps to perform electro-mechanical measurements on Ge NWs by designing and fabricate an adequate substrate. The latter can be used for a wide range of materials such as nanowires or graphene to study transport measurements and electromechanical behaviour. In the case of Ge NWs, a clean dispersion of NWs is critical to the quality of the contact as any large piece of contaminant can short the electrodes. This work is only preliminary to the investigation

of the electromechanical properties of Ge NWs and the remaining will be carried out by Eoin McCarthy.

References

1. Xia, Y. N.; Yang, P. D.; Sun, Y. G.; Wu, Y. Y.; Mayers, B.; Gates, B.; Yin, Y. D.; Kim, F.; Yan, Y. Q., One-dimensional nanostructures: Synthesis, characterization, and applications. *Advanced Materials* **2003,** *15* (5), 353-389.

2. Lieber, C. M., Nanoscale science and technology: Building a big future from small things. *MRS Bull.* **2003,** *28* (7), 486-491.

3. Cui, Y.; Wei, Q. Q.; Park, H. K.; Lieber, C. M., Nanowire nanosensors for highly sensitive and selective detection of biological and chemical species. *Science* **2001,** *293* (5533), 1289-1292.

4. Hong, K.-H.; Kim, J.; Lee, S.-H.; Shin, J. K., Strain-Driven Electronic Band Structure Modulation of Si Nanowires. *Nano Letters* **2008,** *8* (5), 1335-1340.

5. Fischetti, M. V.; Laux, S. E., Band structure, deformation potentals, and carrier mobility in strained Si, Ge, and SiGe alloys. *Journal of Applied Physics* **1996,** *80* (4), 2234-2252.

6. Ekinci, K. L.; Roukes, M. L., Nanoelectromechanical systems. *Review of Scientific Instruments* **2005,** *76* (6).

7. Yang, Y. T.; Callegari, C.; Feng, X. L.; Ekinci, K. L.; Roukes, M. L., Zeptogram-Scale Nanomechanical Mass Sensing. *Nano Letters* **2006,** *6* (4), 583-586.

8. Rugar, D.; Budakian, R.; Mamin, H. J.; Chui, B. W., Single spin detection by magnetic resonance force microscopy. *Nature* **2004,** *430* (6997), 329-332.

9. Katz, I.; Retzker, A.; Straub, R.; Lifshitz, R., Signatures for a classical to quantum transition of a driven nonlinear nanomechanical resonator. *Physical Review Letters* **2007,** *99* (4).

10. Jang, J. E.; Cha, S. N.; Choi, Y.; Amaratunga, G. A. J.; Kang, D. J.; Hasko, D. G.; Jung, J. E.; Kim, J. M., Nanoelectromechanical switches with vertically aligned carbon nanotubes. *Applied Physics Letters* **2005,** *87* (16).

11. Qiliang, L.; Sang-Mo, K.; Richter, C. A.; Edelstein, M. D.; Bonevich, J. E.; Kopanski, J. J.; Suehle, J. S.; Vogel, E. M., Precise Alignment of Single Nanowires and Fabrication of Nanoelectromechanical Switch and Other Test Structures. *Nanotechnology, IEEE Transactions on* **2007,** *6* (2), 256-262.

12. Husain, A.; Hone, J.; Postma, H. W. C.; Huang, X. M. H.; Drake, T.; Barbic, M.; Scherer, A.; Roukes, M. L., Nanowire-based very-high-frequency electromechanical resonator. *Applied Physics Letters* **2003,** *83* (6), 1240-1242.

13. Feng, X. L.; He, R. R.; Yang, P. D.; Roukes, M. L., Very high frequency silicon nanowire electromechanical resonators. *Nano Letters* **2007,** *7* (7), 1953-1959.

14. Blencowe, M. P., Nanoelectromechanical systems. *Contemp. Phys.* **2005,** *46* (4), 249-264.

15. Subramanian, A.; Alt, A. R.; Dong, L.; Kratochvil, B. E.; Bolognesi, C. R.; Nelson, B. J., Electrostatic Actuation and Electromechanical Switching Behavior of One-Dimensional Nanostructures. *ACS Nano* **2009,** *3* (10), 2953-2964.

16. Postma, H. W. C.; Kozinsky, I.; Husain, A.; Roukes, M. L., Dynamic range of nanotube- and nanowire-based electromechanical systems. *Applied Physics Letters* **2005,** *86* (22), 223105-3.

17. Smith, D. A.; Holmberg, V. C.; Lee, D. C.; Korgel, B. A., Young's Modulus and Size-Dependent Mechanical Quality Factor of Nanoelectromechanical Germanium Nanowire Resonators. *J. Phys. Chem. C* **2008,** *112*, 10725-10729.

18. Andzane, J.; Petkov, N.; Livshits, A. I.; Boland, J. J.; Holmes, J. D.; Erts, D., Two-Terminal Nanoelectromechanical Devices Based on Germanium Nanowires. *Nano Letters* **2009,** *9* (5), 1824-1829.

19. Ziegler, K. J.; Lyons, D. M.; Holmes, J. D.; Erts, D.; Polyakov, B.; Olin, H.; Svensson, K.; Olsson, E., Bistable nanoelectromechanical devices. *Applied Physics Letters* **2004,** *84* (20), 4074-4076.

20. Capasso, F., BAND-GAP ENGINEERING - FROM PHYSICS AND MATERIALS TO NEW SEMICONDUCTOR-DEVICES. *Science* **1987,** *235* (4785), 172-176.

21. Geller, C. B.; Wolf, W.; Picozzi, S.; Continenza, A.; Asahi, R.; Mannstadt, W.; Freeman, A. J.; Wimmer, E., Computational band-structure engineering of III-V semiconductor alloys. *Applied Physics Letters* **2001,** *79* (3), 368-370.

22. Seravalli, L.; Minelli, M.; Frigeri, P.; Franchi, S.; Guizzetti, G.; Patrini, M.; Ciabattoni, T.; Geddo, M., Quantum dot strain engineering of InAs/InGaAs nanostructures. *Journal of Applied Physics* **2007,** *101* (2).

23. Tong, B. Y.; Kiriushcheva, N., Band-gap engineering of a Sech-squared potential in heterojunctions. *Phys. Lett. A* **1997,** *229* (1), 49-52.

24. Ozgur, U.; Alivov, Y. I.; Liu, C.; Teke, A.; Reshchikov, M. A.; Dogan, S.; Avrutin, V.; Cho, S. J.; Morkoc, H., A comprehensive review of ZnO materials and devices. *Journal of Applied Physics* **2005,** *98* (4).

25. Makino, T.; Segawa, Y.; Kawasaki, M.; Ohtomo, A.; Shiroki, R.; Tamura, K.; Yasuda, T.; Koinuma, H., Band gap engineering based on MgxZn1-xO and CdyZn1-yO ternary alloy films. *Applied Physics Letters* **2001,** *78* (9), 1237-1239.

26. Crespi, V. H.; Cohen, M. L.; Rubio, A., In situ band gap engineering of carbon nanotubes. *Physical Review Letters* **1997,** *79* (11), 2093-2096.

27. van Mullekom, H. A. M.; Vekemans, J.; Havinga, E. E.; Meijer, E. W., Developments in the chemistry and band gap engineering of donor-acceptor substituted conjugated polymers. *Mater. Sci. Eng. R-Rep.* **2001,** *32* (1), 1-40.

28. Vo, T.; Williamson, A. J.; Galli, G., First principles simulations of the structural and electronic properties of silicon nanowires. *Physical Review B* **2006,** *74* (4).

29. Lee, K. M.; Choi, T. Y.; Lee, S. K.; Poulikakos, D., Focused ion beam-assisted manipulation of single and double b-SiC nanowires and their thermal conductivity measurements by the four-point-probe 3-w method. *Nanotechnology* **2010,** *21*, 125301.